ODGERS, ARTHUR TERRANCE ROHAN

PROCESSING AND INTERPRETARION OF THE BUSHVELD SEISMIC SURVEY P1-86

MSc UP 1992

Processing and interpretation of the Bushveld seismic survey P1-86

by

ARTHUR TERRANCE ROHAN ODGERS

Submitted in partial fulfilment of the requirements
for the degree of

MASTER OF SCIENCE

in the Faculty of Science

University of Pretoria

Pretoria

January, 1992

Processing and interpretation of the Bushveld seismic survey P1-86

by

ARTHUR TERRANCE ROHAN ODGERS

Promoter : R. C. Hinds
Co-promoter : Prof G. Von Gruenewaldt
Department : Geology
Degree : Magister Scientiae in Exploration Geophysics

ABSTRACT

An investigation into the processing and interpretation of the P1-86 reflection seismic data, acquired by the Geological Survey of South Africa in 1986, is shown in this thesis. The seismic line is geographically located west of Pretoria, from Sandpits to Swartdamstat.

A non-migrated stacked section was presented in Du Plessis and Levitt (1987). The presence of structural complexities and high amplitude diffractions/out-of-plane reflections on the original seismic section prompted a decision to process the line using the methodology of interpretive data processing (Hinds *et al.*,1989). It was postulated that interpretive processing and migration of the data may improve the imaging of some of the structural complexities, noted in the original investigation by Du Plessis and Levitt (1987), and enhance seismic events in regions of low signal-to-noise ratio.

At each step in the processing sequence, the effects of the processing on the data was evaluated. The reprocessed brute stack section revealed additional structural detail.

Phase-shift migration of the stacked section restored complex reflection events to true spatial positions. Non-collapsed diffraction energy is attributed to out-of-the-plane reflections and noise. It is suggested that these diffractions may result from complex 3-D geological structure.

A geological model was postulated using the interpretation derived from the final migrated and non-migrated stacked time sections. It is proposed that the Transvaal Sequence and the upper zone of the Rustenburg Layered Suite are regionally continuous across the survey. The RLS and Transvaal Sequence are identified as northerly dipping events which appear to undergo structural updoming towards the northern part of the survey. The marginal norites are proposed to pinch out, and the main zone is proposed to thin, over the anticlinal structure.

The postulated updoming is possibly related to similar structures in the Brits area (Roberts, 1981), a few kilometers to the west of the survey. The anticlinal structure resulting from the postulated updoming may have caused a tensional regime in the rocks of the Transvaal Sequence and RLS. This may have resulted in complex faulting. Signal interference in this region of faulting, caused by conflicting reflectors (Ohlovich, 1964), is proposed to be one of the causes of the low signal-to-noise ratio in the northern region of the survey.

A model of the subsurface imaged by the seismic survey was fitted to the regional gravity data using two-dimensional forward modeling (Talwani *et al.*, 1959). The good fit of the calculated gravity anomaly values to the observed gravity anomaly values supports the feasibility of the seismically-derived geological model.

Processing and interpretation of the Bushveld seismic survey P1-86

deur

ARTHUR TERRANCE ROHAN ODGERS

Leier : R. C. Hinds
Mede-leier : Prof G. Von Gruenewaldt
Departement : Geologie
Graad : Magister Scientiae in Eksplorasie Geofisika

SAMEVATTING

Die P1-86 seismiese refleksiedata wat in 1986 deur die Geologiese Opname van Suid Afrika ingesamel is, is interaktief geprosesseer en geïnterpreteer. Die seismiese lyn is geografies wes van Pretoria, en strek vanaf Sandpits na Swartdamstat.

'n Onmigreerde gestapelde seksie is deur Du Plessis en Levitt (1987) voorgestel. Die voorkoms van komplekse strukturele en groot amplitude diffraksies/buite-die-vlak refleksies op die oorspronklike seismiese seksie het daatoe gelei dat die lyn geherprosesseer is, met 'n deeglike evaluasie van elke stap en elke parameter. Daar is voorgestel dat opeenvolgende interpretiewe beoordeling voor elke fase van die prosessering, asook die toepassing van die migrasietegniek, die gehalte van die seismiese refleksie profiel, wat volgens Du Plessis en Levitt (1987) a.g.v. die geologiese

(strukturele) kompleksiteit onduidelik gemaak is, mag verbeter. Dit is ook gepostuleer dat hierdie benadering die seismiese gebeurtenisse sou verbeter in die gebiede met 'n lae sein-tot-geraas verhouding.

Met elke stap in die prosesseringsroetine, is die gevolge van die prosessering op die data geëvalueer. Die hergeprosesseerde gestapelde seksie het addisionele strukturele besonderhede uitgewys.

Faseverskuiwingsmigrasie van die gestapelde data het komplekse refleksiegebeurtenisse na hulle ware ruimtelike posisies verskuif. Die diffraksie-energie wat nie verval het nie, is aan buite-die-vlak refleksies en geraas toegeskryf. Dit is moontlik dat hierdie diffraksies deur 'n komplekse 3-D struktuur veroorsaak is.

'n Geologiese model is voorgestel uit die interpretasie van die finale migreerde en onmigreerde gestapelde tydseksies. Die Transvaal Opeenvolging en die boonste sone van die Rustenburg Gelaagde Suite is geïnterpreteer as regionaal aaneenlopend in die opnamegebied. Die RGS en die Transvaal Opeenvolging is geïdentifseer as noordelik hellende opeenvolgings wat antiklinale vervorming in die noordlike gebied van die opname ondergaan het. Daar word voorgestel dat die noriete van die randsone uitknyp, en die hoofsone dunner word oor die antiklinale struktuur.

Die voorgestelde antiklien kan vergelyk word met soortgelyke strukture in die Britsgebied (Roberts, 1981), 'n paar kilometer wes van die opname. Die antiklinale opbuiging kon 'n rekspanningsgebied en gevolglike verskuiwings in die gesteentes van die Transvaal Opeenvolging en die RGS laat onstaan het. Sein interferensie in die verskuiwingsgebied, wat deur strydende reflektors veroorsaak word (Ohlovich, 1964), is voorgestel as een van die oorsake vir die lae sein-tot-geraas verhouding in die noordelike gebied van die opname.

'n Geidealiseerde geologiese profiel wat uit die interpretasie van die seismiese opname gevolg het, is deur twee-dimensionele voorwaartse modelering (Talwani *et al.*, 1959) op die regionale gravitasiedata gepas. Die goeie passing van die berekende gravitasie-anomaliewaardes met die waargenome gravitasie-anomaliewaardes ondersteun die haalbaarheid van die seismies-geïnterpreteerde geologiese model.

TABLE OF CONTENTS

CHAPTER 1

INTRODUCTION

CHAPTER 2

GEOLOGICAL AND GEOPHYSICAL MODELS
OF THE BUSHVELD COMPLEX

CHAPTER 3

DATA ACQUISITION

CHAPTER 4

PRESTACK PROCESSING

CHAPTER 5

POSTSTACK PROCESSING

CHAPTER 6

INTERPRETATION

CHAPTER 7

CONCLUSION

APPENDICES

LIST OF FIGURES

LIST OF TABLES

CHAPTER 1

INTRODUCTION

1.1 INTRODUCTION

Interpretive seismic data processing and subsequent proposed interpretations of the P1-86 regional seismic line, acquired in the southwest portion of the Bushveld Complex, South Africa (Fig. 1.1), are presented in this thesis. The seismic survey, performed in 1986, was commissioned by the Geological Survey of South Africa in order to delineate subsurface geological structures in the study area. The specific objectives of the survey were to determine along the seismic traverse:

1. the total thickness of the Rashoop Granophyre Suite and Lebowa Granite Suite assemblages;

2. the shape and extent of the Rustenburg Layered Suite (RLS);

3. the structural relationship between the RLS and the Transvaal Sequence; and

4. the configuration of the Transvaal basin along the seismic traverse.

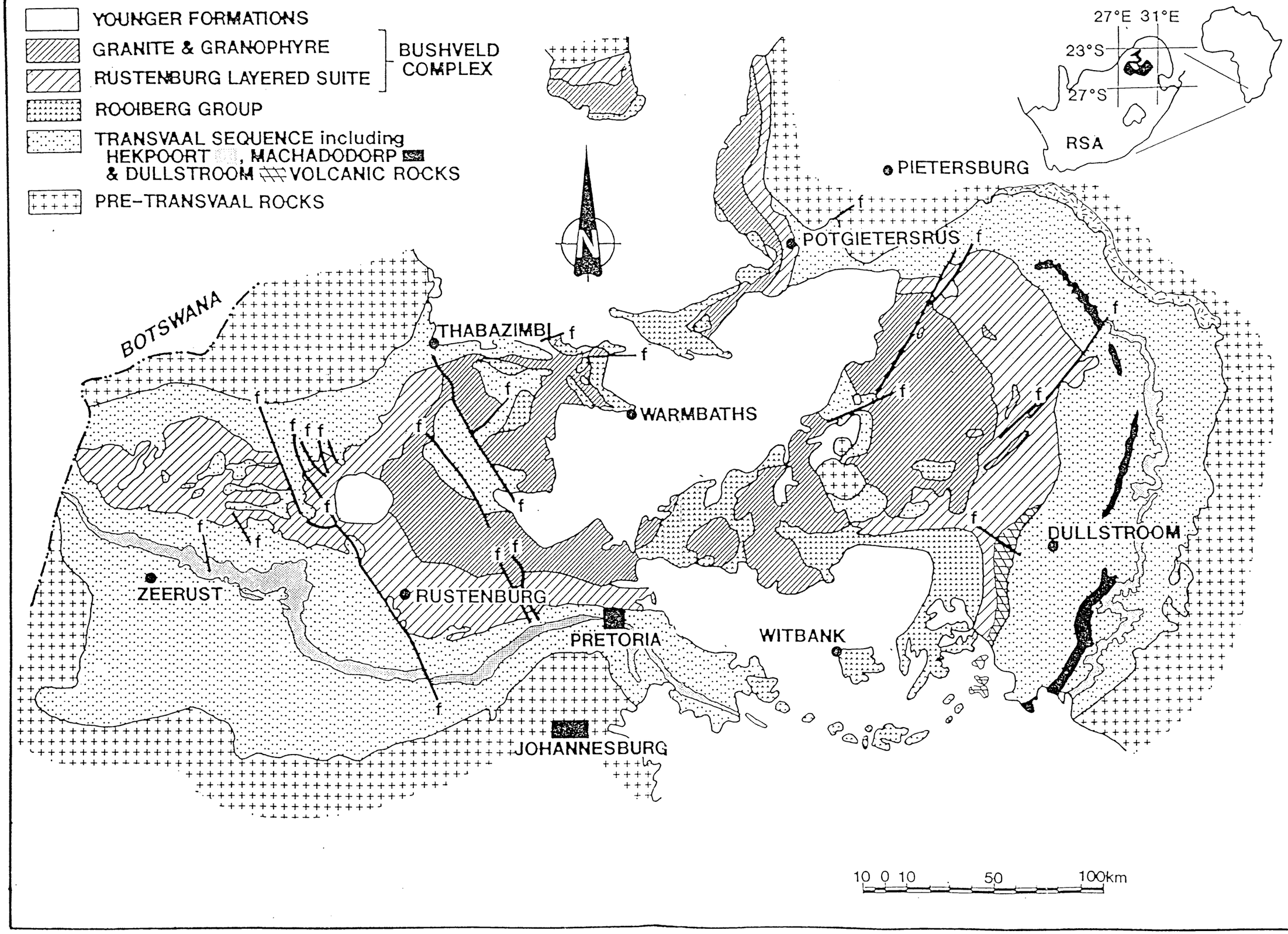

Fig. 1.1 Locality map of the Bushveld Complex.

The objectives of this thesis are to:

1. review the geology and pertinent geological and geophysical models of the study area;

2. review the data acquisition of the seismic line;

3. investigate the effects of processing parameter selection in the prestack and poststack processing runstreams, using interpretive data processing;

4. present an interpretation of the poststack seismic data; and

5. evaluate the feasibility of an earlier interpretation by Du Plessis and Levitt (1987) in light of the results obtained by the application of an interpretive processing procedure.

1.2 INTERPRETIVE DATA PROCESSING

The interpretation of surface seismic data is intimately linked to the processing that has been performed on the data (Hinds *et al.*, 1989). Each step of the processing sequence can affect the interpretation of the final stacked section by introducing processing artifacts. Interpretive data processing optimizes the various stages of the processing runstream by repeated interpretation of the brute stack through to the final migrated stack.

Interactive processing systems allow a "hands-on" perspective of the data. This promotes an appreciation of the effect of each processing step on the seismic data and enables the processor and interpreter to optimize the processing parameters by experimenting with the data until a satisfactory result is achieved (as for the migration processing sequence in Hosken and Deregowski, 1985); namely the optimum seismic section, constrained by processing and interpretation insight.

1.3 THESIS ORGANIZATION

In Chapter 1 the objective of the thesis is presented and interpretive data processing is reviewed. The regional geology of the Bushveld Complex and the geology of the specific study area, as well as published models for the Bushveld Complex and the study area, are reviewed in Chapter 2. The survey route and the parameters used during data acquisition in the P1-86 seismic survey are presented in Chapter 3. A review of the Vibroseis seismic source is also presented in Chapter 3. Prestack and poststack interpretive seismic data processing is reviewed in Chapters 4 and 5, respectively. Interpretations of the poststack seismic data and a proposed geological model of the subsurface along the seismic line are presented in Chapter 6. Details of the processing runstream formulated in this thesis are presented in Chapter 7. Comparisons are made between the processing sequence used in this thesis and that used by the Geological Survey. The geological model proposed by Du Plessis and Levitt (1987) is evaluated in light of the model proposed in this thesis.

CHAPTER 2

GEOLOGICAL AND GEOPHYSICAL MODELS OF THE BUSHVELD COMPLEX

2.1 INTRODUCTION

The Bushveld Complex, located in the central Transvaal Province, South Africa (Fig. 1.1), contains the world's largest known reserves of the platinum group elements, chromite and vanadium.

The Bushveld Complex consists of the following suites of igneous rocks:

1. the Rustenburg Layered Suite (RLS);
2. the Rashoop Granophyre Suite; and
3. the Lebowa Granite Suite (LGS).

The exposed parts of the layered sequence of the Bushveld Complex cover an area of approximately 12 000 km^2, and reach a thickness of 7 750 m in the western Bushveld Complex and 9 000 m in the eastern Bushveld. The Bushveld Complex as a whole subcrops over an area of approximately 60 000 km^2, considerably larger than other known layered intrusions (Hunter, 1975).

2.2 GEOLOGICAL AND GEOPHYSICAL MODELS

The structure of the Rustenburg Layered Suite of the Bushveld Complex has been considered to be a huge laccolith (Molengraaff, 1901; Jorissen, 1904; Mellor, 1906), a number of smaller laccolithic intrusions (Molengraaff, 1902), and a lopolith (Daly and Molengraaff, 1924; Hall, 1932). Daly and Molengraaff (1924) noted that the lopolithic structure of the RLS may involve a group of igneous units, termed a "complex". Subsequently, the structure of the RLS was described (Willemse, 1969) to consist of five adjoining, basin-shaped masses of igneous rocks.

Recently, many geophysical techniques (including regional gravity surveys, ground and aeromagnetic surveys, time domain EM, DC resistivity soundings and seismic reflection studies) have been used to constrain models of the Bushveld Complex (Meyer, 1987). A number of models for the structure of the Bushveld Complex have been proposed, some of which are presented in this review. The models presented are detailed in the following publications:

1. Cousins (1959);
2. Smit (1961), and Smit *et al.* (1962);
3. Walraven (1974), Walraven and Darracott (1976), and Engelbrecht (1987);
4. Meyer and De Beer (1987); and
5. Molyneux and Klinkert (1978), and Kleywegt and Du Plessis (1986).

Models derived from the interpretation of gravity and magnetic data do not support the proposal of a lopolith with mafic material present beneath the centre of the complex, but suggest rather that the Bushveld Complex consists of a number of separate, overlapping intrusions (Truter, 1955; Hattingh, 1983). Interpretation of gravity data (Cousins, 1959) suggested that the interior remnants of the Transvaal Sequence are an indication of updoming of the central portion of the Transvaal basin, prior to emplacement of the Bushveld Complex. Cousins (1959) concluded that the mafic sequence of the Bushveld Complex was not emplaced in the central portion of the Transvaal basin, but in "curved trough-like bodies" around a central dome.

Interpretation of modeled gravity data of the central region of the Bushveld Complex (Smit, 1961; Smit *et al.*, 1962) led to the proposal of a model consisting of discrete compartments, where the Lebowa Granite Suite (LGS) in the central part of the Complex is underlain by sediments of the Transvaal Sequence, and not by the mafic rocks of the Rustenburg Layered Suite. On the western lobe of the Complex, the positive gravity and magnetic anomalies associated with the RLS are modeled as a trough-shaped synformal unit.

The distribution of granophyre zones associated with the contact between the RLS rocks and the overlying Bushveld granite, in conjunction with interpretation of aeromagnetic and gravity data, led to the proposal that the western part of the Bushveld Complex is folded into open synclines and anticlines along northwest trending axes (Walraven, 1974; Walraven and Darracott, 1976; Engelbrecht, 1987). The folding occurred as a result of compressional forces operating in a north-east to south-west direction. Molyneux and Klinkert (1978) propose that similar folding, having intersecting axes as proposed by Hunter (1975), may be related to domal structures occurring in the eastern Bushveld Complex. Such folding in the central lobe may also result in (subsurface) domal structures.

The results of deep DC resistivity soundings performed over the Bushveld Complex and Transvaal Sequence in conjunction with geological constraints led Meyer and De Beer (1987) to propose that towards the centre of the western and eastern compartments, the LGS is underlain by rocks of the Transvaal Sequence. The interpretation of the geoelectrical data, while supporting earlier gravity models according to which mafic rocks are absent from the central portion of the Complex, shows that the Bushveld granite lies directly over the Archaean basement, rather than over the Transvaal Sequence rocks.

In contrast to the models of the RLS which suggest a trough-shaped structure for the RLS, gravity and magnetic modeling of the eastern Bushveld Complex (Molyneux and Klinkert, 1978) indicated that the RLS can be modeled as a sill-like structure, with the ferrogabbros of the upper zone thinning toward the centre of the Bushveld Complex and pinching out towards the west. Kleywegt and Du Plessis (1986) modeled the RLS as a northerly-dipping tapering sheet, terminating approximately 25 km north of the northernmost outcrop of the RLS in the survey area. Du Plessis and Kleywegt (1987) have subsequently shown that gravity anomalies attributed to trough-shaped models may be modeled equally successfully using a dipping sheet model for the RLS (Fig. 2.1). Palaeomagnetic studies (Hattingh, 1991) also favour a dipping sheet model of the RLS.

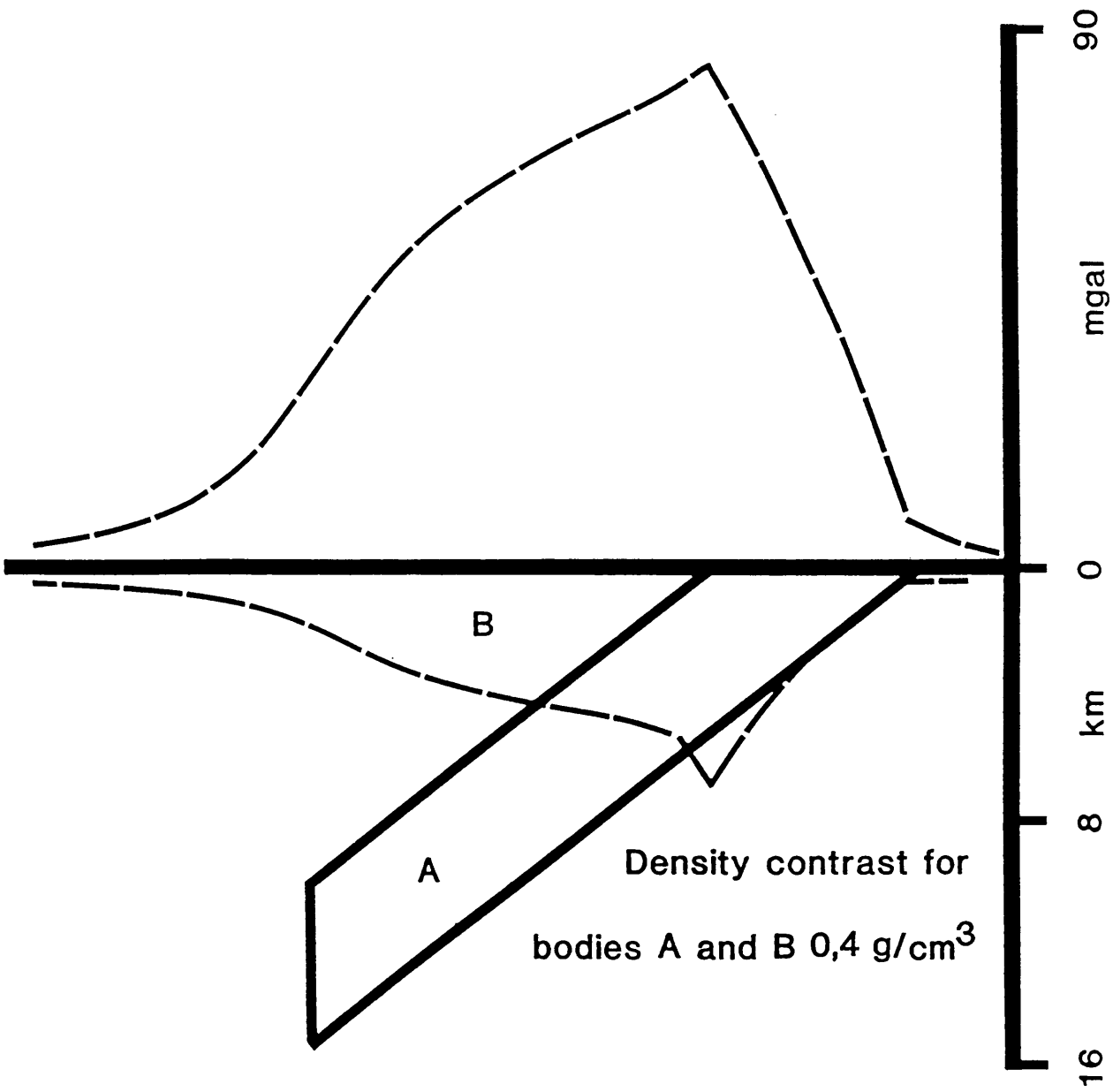

Fig. 2.1 Gravity model illustrating that an anomaly attributed to a trough shaped body (B) may also be modeled by a dipping sheet (A) (after du Plessis and Kleywegt, 1987).

2.3 GEOLOGY OF THE BUSHVELD COMPLEX IN THE SURVEY AREA

The southern portion of the seismic survey traverses rocks of the Transvaal Sequence, while the central and northern portions lie upon Bushveld Complex and Karoo Sequence rocks respectively (Figure 2.2).

2.3.1 *THE TRANSVAAL SEQUENCE*

Dolomite of the Malmani Subgroup of the Chuniespoort Group is overlain by approximately 1 200 m of shale (dip 20°-28°N) of the Timeball Hill Formation and quartzite of the Boshoek Formation (Fig. 2.3). Approximately 550 m (South African Committee for Stratigraphy (SACS), 1980) of the Hekpoort Andesite Formation overlies the Boshoek Formation. This is in turn overlain conformably by the Strubenkop Shale Formation, the Daspoort Quartzite Formation, the Silverton Shale Formation, and the Magaliesberg Quartzite Formation. The stratigraphic thickness of the package of alternating shales and quartzites (dip 22°-26°N) above the Hekpoort Andesite Formation is approximately 2 500 m.

2.3.2 *SILLS OF THE TRANSVAAL SEQUENCE*

Numerous diabase sills occur within the shales and quartzites of the Transvaal Sequence. These sills dip conformably with the sedimentary layering. The contact between the sills and the shales of the Transvaal Sequence may represent considerable reflectivity contrasts. Such reflectivity contrasts may be responsible for the high amplitude reflections on the seismic section. The sills that may be imaged by the seismic survey will be discussed. Unfortunately, little information exists on the lateral continuity of these sills, both along strike and down dip.

South of the starting point of the survey are two diabase sills in the shales of the Timeball Hill Formation. The southernmost sill is approximately

Fig. 2.2 Geology of the study area and location of the P1-86 seismic line.

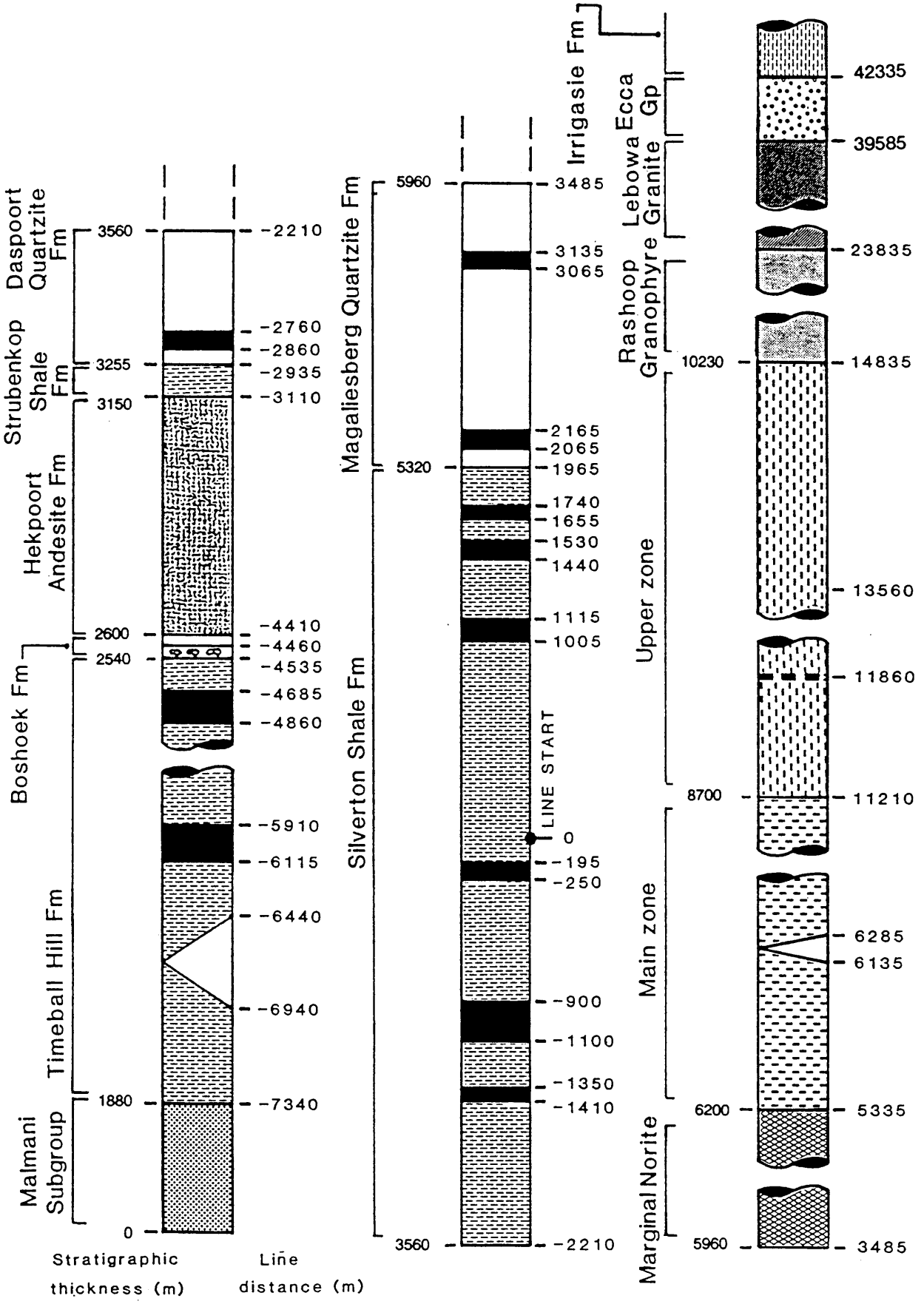

Fig. 2.3 Stratigraphic column of the survey area. For legend see Figure 2.2

85 m thick. The second sill is approximately 75 m thick.

A 42 m thick sill occurring in the Daspoort Quartzite Formation, is located south of the survey starting point.

Six prominent sills occur in the Silverton Shale Formation. The lowest three sills in the sequence occur south of the survey starting point. From lowest to highest in the succession, the sills are approximately 26 m, 85 m, and 23 m thick respectively. The remaining three sills occur north of the starting point, and are approximately 46 m, 38 m, and 36 m thick respectively.

Two sills occur in the Magaliesberg Quartzite Formation. The lower sill is approximately 42 m thick. The upper sill is approximately 30 m thick and is covered by sand at the intersection with the survey.

2.3.3 *THE BUSHVELD COMPLEX AND THE KAROO SEQUENCE*

The norites present in the Rustenburg Layered Suite (RLS) were intruded above the Magaliesberg Quartzite Formation of the Transvaal Sequence. The norite outcrops over approximately 1 500 m of the survey route. Numerous quartzite xenoliths occur along the norite/gabbro contact. Such xenoliths may be present at depth.

A sequence of gabbroic rocks of the main zone of the RLS occurs above the norite. The main zone rocks are traversed for approximately 6 000 m of the survey route. A large quartzite xenolith, which occurs in the gabbro, is traversed by the seismic survey approximately 800 m north of the norite/gabbro contact. The gabbro is overlain by ferrogabbro of the upper zone of the RLS, containing magnetite layers. The ferrogabbro is traversed over approximately 2 250 m of the survey route. The mapped magnetite layers occur along the survey line, approximately 650 m north of the gabbro/ferrogabbro contact. The contact between these two units dips at approximately 25° N. Sandstones

of the Ecca Group of the Karoo Sequence overlie the ferrogabbro at the contact with the granophyre. The sandstones, which have a shallow depth extent, cover the surface along the survey route for approximately 1 250 m.

The granophyre of the Bushveld Complex extends for approximately 9 500 m to the contact with the Lebowa Granite Suite. The Lebowa Granite Suite extends for approximately 15 750 m to the contact with the sandstone/shale/conglomerate package of the Ecca Group. These Ecca Group members occur along the survey route for approximately 2 750 m, up to the contact with the Irrigasie Formation of the Karoo Sequence. The survey then continues on this formation until the end of the seismic line.

To the west of the survey line, south of Brits, horst-graben faulting affects the Rustenburg Layered Suite of the Bushveld Complex. Roberts (1981) proposes that this zone of faulting appears to be centred at the apex of a shallow "bulge" in the floor. Such bulges may have affected regions traversed by the line, thereby influencing the deep seismic signature.

2.4 PREVIOUS RESULTS FROM THE P1-86 SEISMIC SURVEY

An interpretation of a non-migrated stacked section of this seismic line and gravity data (Du Plessis and Levitt, 1987) led to the proposal of an evolutionary model consisting of the following events (Fig. 2.4):

(1) vertical movement along a major pre-Bushveld fault;
(2) erosion of parts of the Transvaal Sequence north of the fault;
(3) further downward motion to the south of the fault; and
(4) controlled emplacement of the RLS only to the south of the fault.

A major fault is proposed to occur 29 km from the south of the line (approximately CMP 12855 in Fig 5.1). The fault is termed the Mabopane Fault (Du Plessis and Levitt, 1987). The proposed fault coincides with a broad region of anomalous reflection events, some of which may originate from outside of the

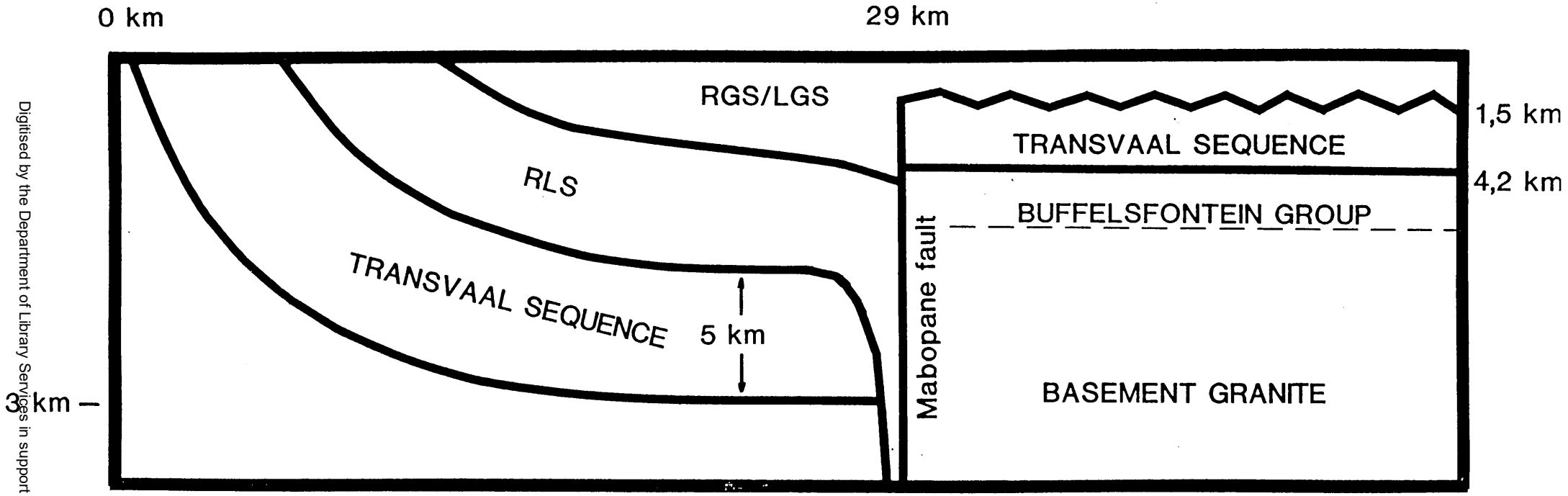

Fig. 2.4 Geological model of the Bushveld Complex in the P1-86 study area, as described in du Plessis and Levitt (1987). RLS - Rustenburg Layered Suite; RGS - Rashoop Granophyre Suite; LGS - Lebowa Granite Suite.

plane of the line. Du Plessis and Levitt (1987) propose that the existence of possible out-of-the-plane reflections imply that the seismic line traverses the Mabopane Fault at an oblique angle.

Vertical movement along the Mabopane Fault promoted conditions favorable for increased erosion on the northern (upthrown) side of the fault. The upper members of the Transvaal Sequence were removed by erosion, leaving only the lower 2 700 m (Du Plessis and Levitt, 1987).

Further downward movement of the southern side of the fault allowed the magma of the RLS, rising along the fault plane, to be emplaced laterally along well developed bedding planes, into the Transvaal sediments to the south (Du Plessis, *pers comm*). To the north, however, the magmatic material was constrained by basement material. The RLS was therefore not emplaced north of the Mabopane Fault (Du Plessis and Levitt, 1987).

Interpretation of the seismic and gravity data led Du Plessis and Levitt to the following conclusions concerning the structural detail of the Bushveld Complex and Transvaal Sequence on either side of the Mabopane Fault:

(1) North of the fault:

(a) an irregular contact between the Bushveld granite and the underlying material occurs. Du Plessis and Levitt conclude that this may be indicative of an erosional surface, proposed to be an erosional remnant of the Transvaal Sequence (the lower 2 700 m), present up to a depth of approximately 4 200 m;

(b) the contact between the Transvaal Sequence and postulated pre-Transvaal rocks of the Buffelsfontein Group occurs at approximately 4 500 m below the surface. This is proposed on the basis of an interpretation of an unconformity between shallow horizontal reflections and deeper northerly dipping events (Du Plessis and Levitt, 1987);

(c) the RLS is absent (Du Plessis and Levitt, 1987); and

(d) a unit of abnormally high density to the north of the fault, occurs between 2 700 m and 4 200 m. The unit is interpreted to be the Chuniespoort Group dolomites (Du Plessis and Levitt, 1987).

(2) South of the fault:

(a) a 5 000 m thick seismic sequence of reflectors, interpreted as the Transvaal Sequence, is preserved below the RLS (Du Plessis and Levitt, 1987); and

(b) along the fault plane, the minimum depth of the base of the Transvaal Sequence is proposed to be 13 000 m (Du Plessis and Levitt, 1987).

CHAPTER 3

DATA ACQUISITION

3.1 INTRODUCTION

In this chapter the following aspects of the acquisition of the seismic reflection data is reviewed:

(1) the survey route of the P1-86 seismic line;
(2) the seismic source used; and
(3) the data acquisition parameters.

3.2 SURVEY ROUTE

The seismic line is shown in Figure 2.2 and is described as follows:

1. the seismic line commenced a short distance south of the Suiderberg interchange, near the Sandpits railway station, west of Pretoria;
2. continuing northwards along the road median between the two tarred lanes of road P200-1, for a distance of 12 km;
3. the survey continued along the unused eastern lane, up to the intersection with road 157;
4. a short extension of the line was made through the veld until it intersected road 318; and
5. the line continued along the road reserve of road 318, ending approximately 9 km north of Swartdamstat.

The total length of the seismic line is approximately 50 km.

Station pegs were placed along the route at 25 m intervals. Permanent markers were placed at the beginning and at the end of the line, at road intersections, and at intermediate points of any gap exceeding 5 km.

3.3 VIBROSEIS: THE SEISMIC SOURCE

A Vibroseis unit (Fig. 3.1) consists of a baseplate, held in contact with the earth's surface by the mass of the truck. A time varying sinusoidal signal is applied to the baseplate, via the hydraulic circuitry, for a period of time known as the "sweep" (Brown and Moxley, 1964; Goupillaud, 1976). This input signal, when applied as a linear function of time and frequency, is of the form

$$S(t) = A(t)\ \sin(at + \frac{b}{2}t^2)$$

where $A(t)$ is a time varying envelope function. The constants, a and b, are related to the initial frequency and the rate of change of frequency with time respectively (Waters, 1978). Generally, three to five Vibroseis units comprise a source array. A more complete description of the workings of a Vibroseis unit is presented by Brown and Moxley (1964).

The duration of a sweep varies according to the survey objectives. During the sweep the receivers are activated. Due to the length of the Vibroseis signal input to the ground, the reflected signals from the various reflectors overlap. This results in a shot record which is visually incoherent. Cross-correlation of the recorded data and input sweep is carried out in order to collapse the input sweep (convolved with the earths reflectivity function) into a (zero phase) Klauder wavelet (Geyer, 1969; Lines and Clayton, 1977).

Cross-correlation involves multiplying the two signals, sample by sample, and adding these products. The output values are the cross-correlation values for given time shifts. The cross-correlation values can be viewed as a measure of how closely the two signals resemble each other for that specific time shift. The Klauder wavelet, resulting from the crosscorrelation, is the autocorrelation of the input sweep signal. The operation of cross-correlation enhances visual recognition of reflection events on the recorded trace (Lines and Clayton, 1977).

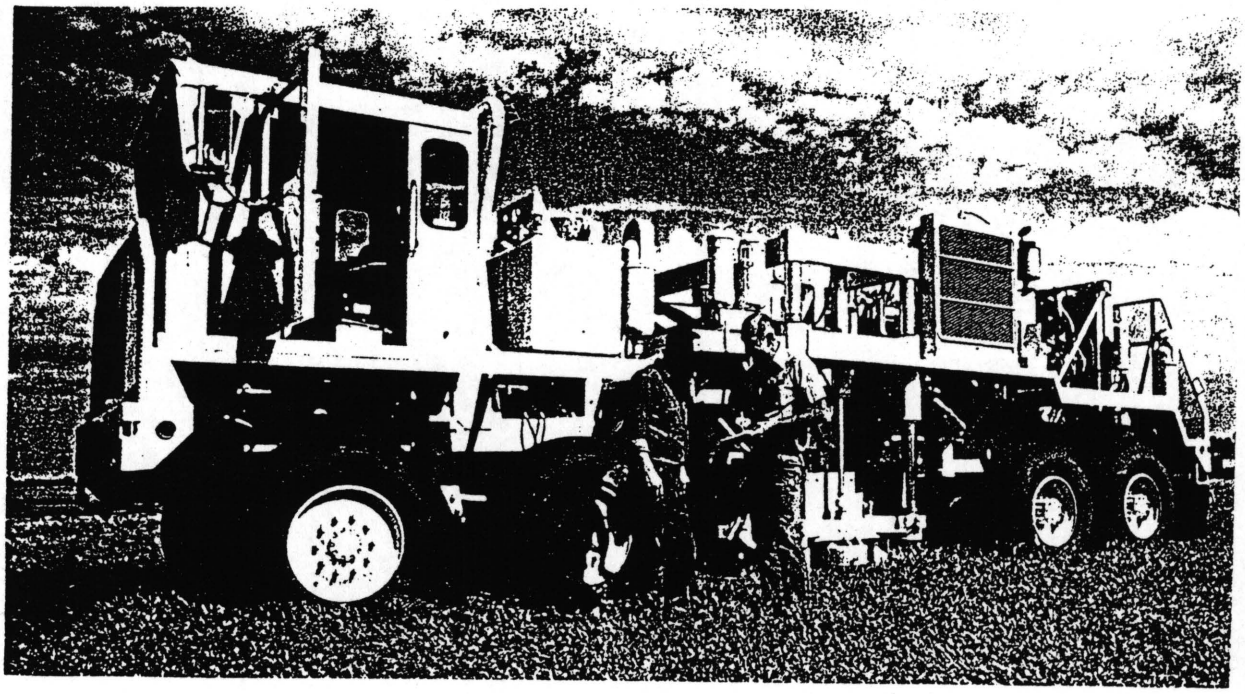

Fig. 3.1 An example of a Vibroseis unit.

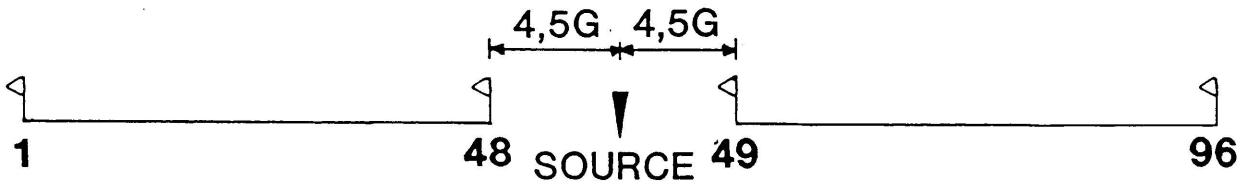

Fig. 3.2 Split-spread geometry used in the P1-86 seismic survey.

In using impulsive seismic sources such as explosives or the dropping of a large weight, the frequency content of the released energy is, to a large extent, non-controllable (Lines and Clayton, 1977). The input frequencies of the Vibroseis sweep and the duration of the time that the unit inputs any respective frequencies into the earth (Crawford *et al.*, 1960; Brown and Moxley, 1964; Waters, 1978), however, is pre-determined. By monitoring the motion of the baseplate it is possible to obtain an approximate measure of the motion of the earth's surface. A feedback system from the baseplate allows the force applied and the phase of the sweep to be varied in an effort to obtain consistency (Lerwill, 1981). Force control feedback is utilized to maintain maximum coupling between the baseplate and the earth. As the baseplate-earth coupling decreases, the applied force is reduced until maximum coupling has again been achieved. Phase lock feedback attempts to remove phase differences between the programmed signal and the compressional wave transmitted through the earth (Lerwill, 1981). The phase changes can be attributed to elasticity in the hydraulic fluid of the drive mechanism (Lerwill, 1981), soil compaction, and physical changes in the soil structure caused by heat buildup.

The frequencies generated by the vibrator circuitry can range from approximately 10 Hz, up to about 200 Hz (Chapman *et al.*, 1981), depending on the objectives of the survey. The earth-vibrator coupled unit has a resonant frequency range, typically between 15 and 30 Hz, at which the generation and coupling of energy to the earth becomes easier (Chapman *et al.*, 1981). To generate frequencies outside this midband requires increasingly higher drive forces to generate sufficient energy. A solution to this operational drawback is to bias the energy content of the sweep towards the higher frequencies (Chapman *et al.*, 1981).

The signal-to-noise ratio can be enhanced by increasing the length of the sweep. The signal-to-noise ratio is increased at a rate proportional to the square root of the sweep length (Crawford *et al.*, 1960).

An environmental advantage of the Vibroseis unit as a seismic source is the low energy density of the transmitted signal. This allows the Vibroseis source to be used on roads and other damage sensitive areas.

3.4 DATA ACQUISITION PARAMETERS

A noise analysis survey was not conducted. The recording and array parameters used during data acquisition were selected by the contractor.

The data were recorded using a split-spread geometry (Fig. 3.2), with 48 receiver stations on either side of the seismic source (96 channels in total). Connected to each receiver takeout were 24 geophones, forming an array (Fig 3.3). The sampling interval of the recorded data is 2 ms, and the cross-correlated output length is 5 seconds.

A shot-gap of 9 station spacings (4.5 on either side) was used in order to minimize near-trace noise. The source interval was two stations (50 m). The Vibroseis source pattern (Fig. 3.4) employed three Vibroseis units in line, with a 12 m baseplate separation between units. Eight sweeps were performed at each source station, with each unit advancing 3 m between sweeps.

The source pattern was centred between station pegs. The frequency range of the sweep was 20 - 90 Hz. The raw Vibroseis records were correlated and summed in the field.

The multiplicity of the data recorded, or fold-coverage, is given by the relation (Sheriff and Geldart, 1985)

$$\text{FOLD} = \frac{(\text{No. of geophones}) \times \Delta G}{2\Delta S}$$

where

ΔG = geophone station spacing

ΔS = source station spacing

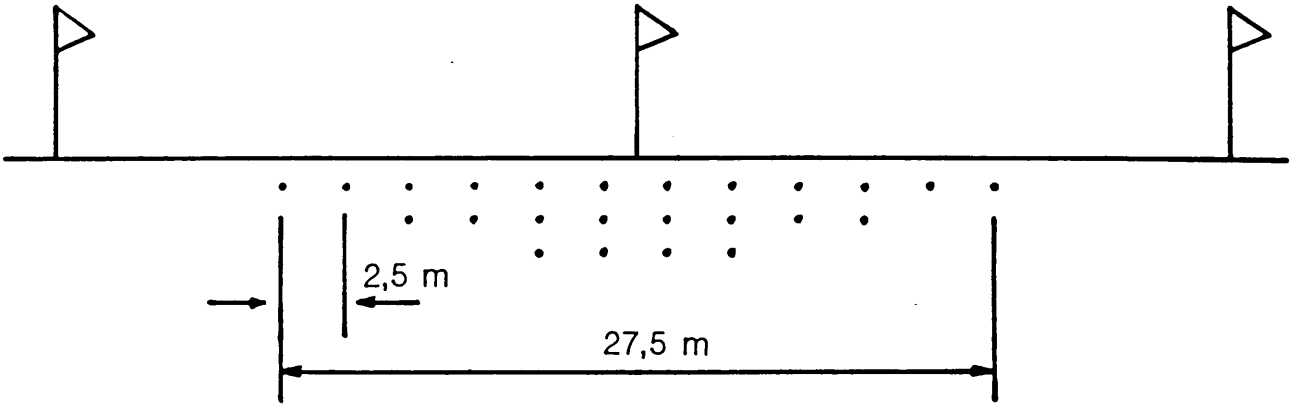

Fig. 3.3 Geophone array used in the P1-86 seismic survey.

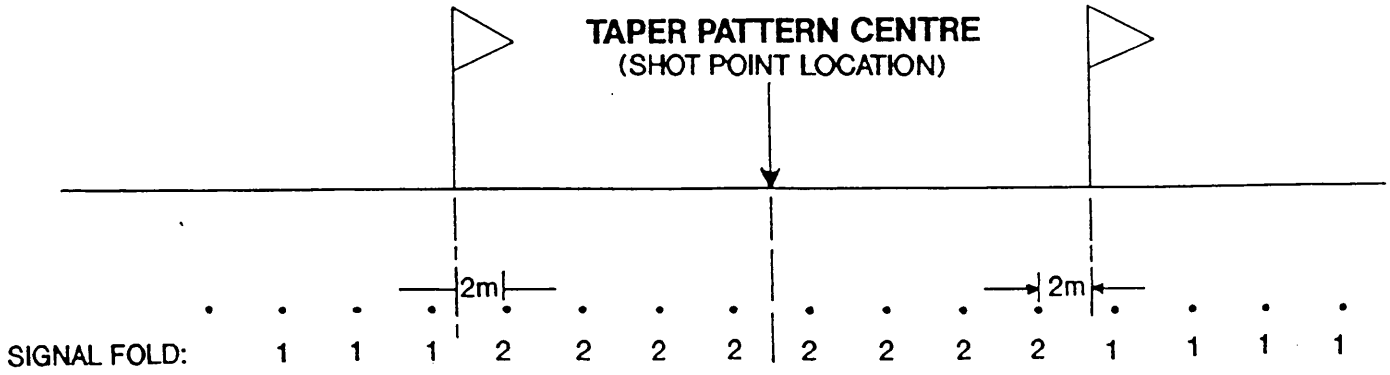

Fig. 3.4 Seismic source pattern used in the P1-86 seismic survey.

The geophone station spacing used for the survey was 25 m, and over the majority of the survey a source station spacing of 50 m was used. This provided 24-fold coverage. At the beginning and end of the line, however, the shot spacing was reduced to one station interval (25 m) in order to build up sufficient coverage at the earliest point.

CHAPTER 4

PRESTACK PROCESSING

4.1 INTRODUCTION

The data processing steps and relevant theoretical background of the prestack processing will be reviewed in this chapter.

The prestack processing may be divided into the following phases:

1. demultiplexing;
2. pre-processing of the input demultiplexed common shot gathers;
3. refraction analysis;
4. stacking velocity analysis;
5. deconvolution;
6. residual statics analysis; and
7. stacking of the common-midpoint gathers.

4.2 DEMULTIPLEXING

In the field, seismic data are recorded onto tape in time sequential format (Sheriff and Geldart, 1983; Sheriff and Geldart, 1985). This may be represented by the matrix of elements:

$$\begin{pmatrix} A_{11} & A_{21} & A_{31} & \cdots & A_{N1} \\ A_{12} & A_{22} & A_{32} & \cdots & A_{N2} \\ A_{13} & A_{23} & A_{33} & \cdots & A_{N3} \\ \cdot & \cdot & \cdot & \cdot & \\ \cdot & \cdot & \cdot & \cdot & \\ \cdot & \cdot & \cdot & \cdot & \\ \cdot & \cdot & \cdot & \cdot & \\ A_{1,M-1} & A_{2,M-1} & A_{3,M-1} & \cdots & A_{N,M-1} \\ A_{1M} & A_{2M} & A_{3M} & \cdots & A_{NM} \end{pmatrix} = A_{ij}$$

where: i = trace no. = 1,...N

j = time sample no. = 1,...M.

The data matrix is recorded row-by-row, until all times have been sampled. During demultiplexing a matrix transpose is performed on the field data. The data are thus rearranged into trace sequential format, represented by the matrix transpose:

$$A_{ij}^{T} = A_{ji}$$

The data are written to one of the standard magnetic tape formats recognized by the Society of Exploration Geophysicists (Sheriff, 1984).

4.3 PRE-PROCESSING OF INPUT DEMULTIPLEXED COMMON SHOT GATHERS

Pre-processing of the input common shot gathers consisted of the following:

1. application of geometry information to the trace headers (shot and receiver configuration, and geographical location);

2. gain application (geometrical divergence correction and cosmetic gain); and
3. interactive editing of noisy data and "first-break" picking.

4.3.1 *APPLICATION OF GEOMETRY INFORMATION*

The physical location and elevation of each shot and receiver are entered into the trace headers of the recorded data. The shot and receiver coordinates are used to determine the bin locations for sorting into common shot, receiver, offset or midpoint gathers. Elevations are used in the refraction static and datum corrections.

4.3.2 *GAIN AND AMPLITUDE BALANCING*

The amplitude of the seismic wave decays with distance from the shot (Claerbout, 1985; Yilmaz, 1987). This decay is due to a number of factors, including geometrical spreading of the wavefront, reflection and transmission losses, and anelastic absorption.

To prevent data loss due to clipping of the signal when the dynamic range of the seismograph is exceeded, gain ranging is employed during signal recording (Sheriff and Geldart, 1985; Yilmaz, 1987). When the signal reaches a minimum threshold amplitude, the gain is adjusted so that the input signal is recorded at an approximately constant amplitude. Before processing, the effect of gain ranging is removed. Since the gain function of each sample is known, removal of gain ranging is a simple arithmetic operation (Yilmaz, 1987).

Reflected seismic signal from deep acoustic impedance interfaces may have very low amplitudes on the gain recovered traces, so it may be necessary to scale the signal to enable interpretation (Claerbout, 1985). This scale or gain function can be chosen deterministically or statistically (Wood, 1982).

The true amplitudes of the reflection events are lost following cosmetic gaining (Sheriff and Geldart, 1983). If one is only interested in the location of the reflectors, amplitude information may not be of prime importance. However, if amplitude differences are to be used to infer lithological parameters of the interfaces (Claerbout, 1985), then the relative amplitude differences must be preserved (McQuillin *et al.*, 1984). Under these conditions, gain application should be confined to correcting for gradual amplitude decay with time (spherical divergence and energy absorption), and those for which there is a physical basis, such as changes in input power (Waters, 1978).

Signal amplitude decay

Gain-recovered traces show a considerable decrease in amplitude with time, spanning a signal range in excess of 100 dB (Hatton *et al.*, 1986). In this section a few of the mechanisms causing signal amplitude decay will be reviewed.

Spherical divergence of wavefronts (Sheriff and Geldart, 1985): Considering a spherical wavefront diverging from a seismic shot (Fig. 4.1); as the energy flow is exclusively radial, it is possible to define two portions of wavefronts with areas W_1 and W_2, such that the flux through W_1 is equal to that through W_2. By definition of the flux, f :

$$f_1 = W_1 I_1 = W_2 I_2 = f_2 \qquad (4.1)$$

where I is the intensity, defined as the amount of energy flowing through unit area in unit time.

As the areas of the wavefronts are proportional to the square of the radii, equation (4.1) can be rewritten as:

$$I_2/I_1 = W_1/W_2 = (r_1/r_2)^2 \qquad (4.2)$$

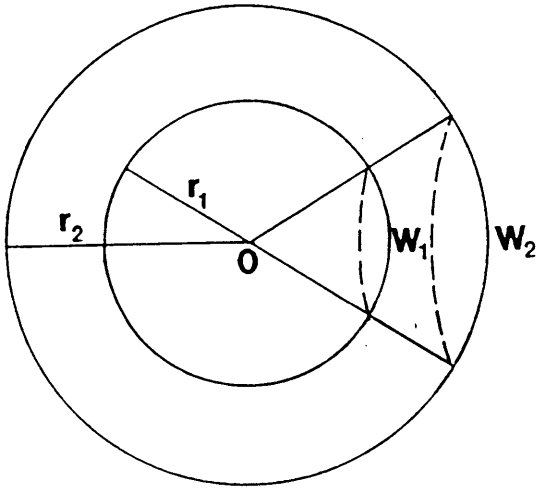

Fig. 4.1 Divergence of a wavefront from a point source in a homogeneous medium (after Sheriff and Geldart, 1985).

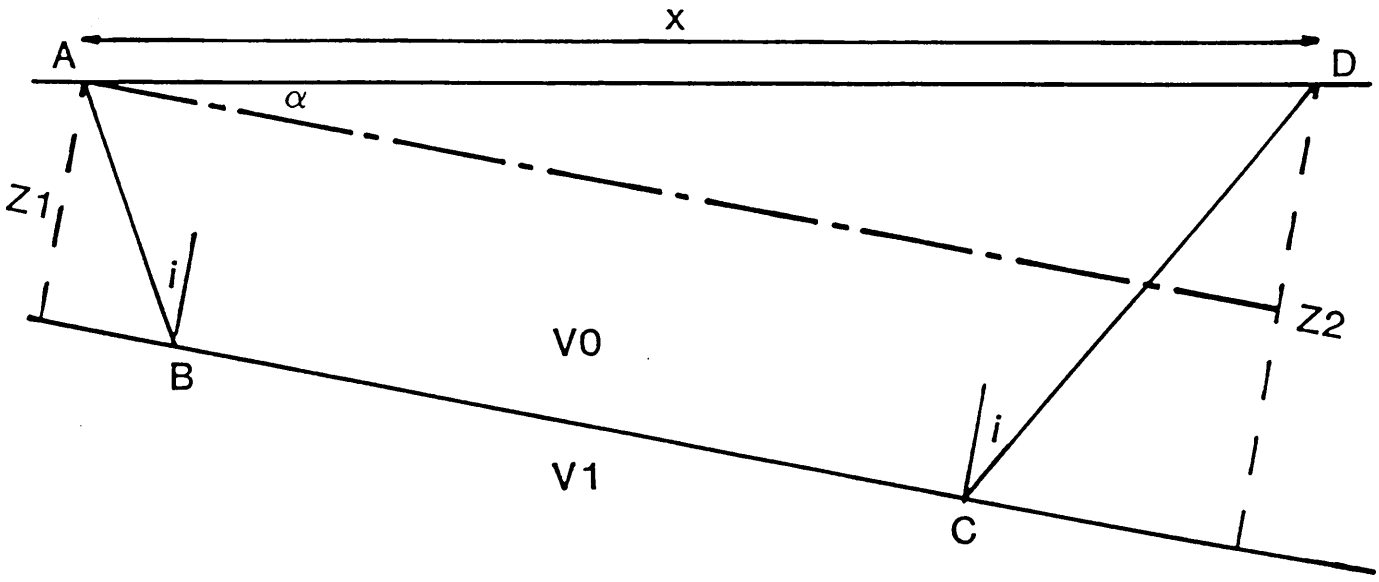

Fig. 4.2 Raypath geometry of the time-term method of refraction static calculation. V_0 and V_1 are the weathering and sub-weathering layer seismic velocities respectively; x is the shot-receiver offset.

As the intensity I is proportional to the energy density E, equation (4.2) can be written as:

$$I_2/I_1 = E_1/E_2 = (r_1/r_2)^2 \qquad (4.3)$$

The energy density and intensity of spherical waves decrease as the inverse of the square of the distance from the source. This decrease in intensity with distance is called spherical divergence (Sheriff and Geldart, 1985).

Energy absorption: The mechanisms of absorption (Sheriff and Geldart, 1985) include internal friction (sliding friction and viscous losses in interstitial fluids), generation of heat during the compressive phase of the wave (McQuillin *et al.*, 1984), and piezoelectric effects.

Determining the magnitude of absorption *in situ* is very difficult since the absorption varies with frequency, higher frequencies undergoing a higher degree of absorption than lower frequencies (McQuillin *et al.*, 1984; Sheriff and Geldart, 1985). Thus absorption models which are designed under high frequency conditions in the laboratory may not be a realistic model of the relatively low frequency signal-media interaction (Sheriff and Geldart, 1985). Expressions for absorption related amplitude decay in terms of distance and time, however, have been empirically determined.

Signal amplitude decay for a given frequency may be modeled as being exponential with distance from the source (Sheriff and Geldart, 1985) and the decrease in amplitude due to absorption may be expressed as:

$$A = A_0 e^{-\mu x} \qquad (4.4)$$

where A and A_0 are signal amplitudes a distance x apart, and μ is the coefficient of absorption.

Another expression for absorption is based on amplitude decay with time, and assumes a cyclic waveform:

$$A = A_0 e^{-ht} \cos \omega t \qquad (4.5)$$

where h is the damping factor.

Sheriff and Geldart (1985) note that, due to the frequency dependance of absorption, the low frequencies losses due to geometrical spreading are more significant than corresponding low frequency losses due to absorption. At higher frequencies, the opposite is observed.

Transmission losses and scattering: Transmission losses caused by partial reflections at interfaces are dependant on geology (Hatton *et al.*, 1986). A series of relatively thin layers of contrasting acoustic impedance will have greater effect than a gradually varying thick layer. Scattering due to inhomogeneities is also geology dependant, becoming important in highly fractured environs (Hatton *et al.*, 1986).

Mode conversion: Energy partitioning in the form of mode conversion (compressional to shear) occur when wavefronts are incident on an interface at angles less than 90° (Sheriff and Geldart, 1985). Reflected and transmitted shear waves are generated, resulting in significant loss of compressional wave energy at angles of acute incidence.

Statistical approach to gain function selection

The deterministic approach to gain function selection considers the causes of amplitude decay, while the more common statistical approach is concerned with negating the effects of amplitude decay.

Automatic gain control (AGC): Most AGC methods use a scaling window and associated scale factor to boost the signal amplitude to the desired output

level (Yilmaz, 1987). The scale factor, SF , takes the form:

$$SF = \frac{DOL}{AAA} \tag{4.6}$$

where DOL represents the desired output level and AAA is the average absolute amplitude of the samples in the window.

Each sample in the time window is multiplied by the scale factor for that window. Generally a sliding window is used in the gaining, and this is known as "time variant trace equalization" (Yilmaz, 1987). The scale factor for a window is calculated and applied to the sample at the centre of the window. The window is then moved down one sample and the process repeated. In this manner a different scale factor is applied to each time sample.

The amount of trace equalization that occurs is dependant on the length of the scaling window. At the long limit (where the window covers the entire trace) each time sample is multiplied by the same scale factor and there is thus no trace equalization. At the short limit (the window covers only one time sample) each sample is boosted to the DOL and thus the trace becomes meaningless.

Exponential gain control: A t^n scaling factor is often applied to the data. The value of $n = 2$ is used to account for geometrical spreading and energy absorption (Claerbout, 1985). In the application of a t^2 gain correction, every data sample is multiplied by the square of the corresponding traveltime.

The seismic shot may be considered to be a point source which generates a spherical wavefield (Claerbout, 1985) (Fig. 4.1). As the energy density decay is proportional to $\frac{1}{t^2}$, and, if we assume that seismic velocity generally increases with depth (Claerbout, 1985), the energy density decreases as a function of $\frac{1}{t^2}$.

This may be expressed as:

$$E \propto \frac{1}{t^2} \tag{4.7}$$

The wave amplitude, however, is proportional to the square root of the energy (Claerbout, 1985; Yilmaz, 1987):

$$\begin{aligned} A &\propto \sqrt{E} \\ A &= \beta\sqrt{E} \\ &= \beta\sqrt{\frac{1}{t^2}} \\ &= \beta\frac{1}{t} \end{aligned} \tag{4.8}$$

where β is a constant of proportionality. The geometry of the energy spreading predicts only a single power of t for the spherical divergence correction (Claerbout, 1985).

The additional factor of t arises from the energy absorption conditions (Claerbout, 1985). Absorption causes high frequencies to decay more rapidly than low frequencies (McQuillin *et al.*, 1984; Sheriff and Geldart, 1985). Assuming a broad-band source, after time t the original broadband spectrum can be replaced by a damped exponential function of frequency:

$$t \rightarrow e^{(-\alpha\omega t)} \tag{4.9}$$

where α is the decay constant (Claerbout, 1985).

The seismic energy available at any time is given by the area under the exponential; integrating this over all frequencies results in an inverse power of t (Claerbout, 1985):

$$E_t = \int_0^{\infty} e^{(-\alpha\omega t)} d\omega$$

$$= \left\{ 0 - \left(\frac{1}{-\alpha t} \right) \right\}$$

$$= \frac{1}{\alpha t} \qquad (4.10)$$

From equations (4.8) and (4.10), compensating for the effects of both geometrical spreading and energy absorption involves correcting with a t^2 scaling function (Claerbout, 1985).

Data balancing: Data amplitude balancing may be performed by applying a gain function, obtained from a smoothed trace envelope, to the trace.

The envelope of the function is the curve obtained by smoothly joining adjacent peaks or troughs along a trace, and is a reliable attribute describing the rate of amplitude decay (Yilmaz, 1987). Such an envelope is fitted to each trace, and the envelope is then bandpass filtered with a low frequency window (typically less than 5Hz). A new envelope is then fitted to the trace obtained as a result of bandpass filtering the original envelope function. The amplitude at each time sample in the original trace is then divided by the corresponding amplitude in the filtered trace envelope.

Deterministic approach to gain function selection

Geometrical spreading correction: The geometrical spreading gain correction applied to the data utilized stacking velocities to calculate the approximate distance travelled by the seismic wavefront, for each time sample in the trace. The gain-corrected output is the input sample amplitude multiplied by the calculated travel distance.

4.3.3 *TRACE EDITING AND FIRST BREAK PICKING*

Interactive processing was used to remove from the seismic shot records any noisy or dead traces, and to perform first break picking.

Traces removed were those containing abundant high frequency noise in the absence of seismic reflection signal, those displaying a continuous mono-frequency response, and those that represented dead receivers.

First break picking is performed in order to facilitate the calculation of refraction static corrections.

4.4 REFRACTION STATIC CORRECTIONS

Static corrections are designed to remove path-dependent variations in shot-to-receiver traveltimes in a shot record. These variations may be caused by changes in surface elevation and near-surface velocity inhomogeneities (Sheriff, 1984). Due to the generally low seismic velocity of the weathering layer (Taner *et al.*, 1974), small changes in the near surface velocity may cause significant static shifts in the data. Variations in thickness and elevation also result in static distortions of the data (Farrell and Euwema, 1984; Rothman, 1986). Using the picked first break times or low velocity layer (LVL) survey information (Rogers, 1985), the weathering layer velocity and thickness are calculated under each geophone and shot station (Farrell and Euwema, 1984). From these calculated values, the refraction static

corrections for the shots and receivers are computed. These corrections are then applied to the data by performing a bulk time shift to each trace, as determined by the calculated static corrections (Farrell and Euwema, 1984). Common midpoint gathers may later be corrected to an elevation datum in order to reduce the data to a survey constant datum.

Most automated static correction techniques are based on the assumption that the seismic waveform is invariant with time (a static temporal shift of the traces in a gather will compensate for path dependant variations in seismic traveltimes (Farrell and Euwema, 1984)). Despite the fact that the earth acts as a low pass frequency filter, the great success of automatic static corrections in improving the signal-to-noise ratio serves to justify the assumption that a temporal translation of a trace can be employed to reduce path-dependent traveltime variations (Wood, 1982).

The method used in this research for the computation of refraction statics is based on the time-term method of Farrell and Euwema (1984).

4.4.1 *TIME-TERM METHOD*

Surface consistent refraction statics are calculated using a time term method (Farrell and Euwema, 1984). If a refraction statics problem can be formulated into a linear system of equations, then least-squares decomposition can be used to derive a solution (Yilmaz, 1987). This forms the basis of the time-term method as applied here.

The time-term related to the individual static correction is decomposed into the downgoing and upgoing time components, and the refractor time component. The fundamental equations of the method are reviewed below. The time-term method is reviewed in detail in Appendix A.

Considering the raypath geometry of Figure 4.2, the traveltime between source (A) and receiver (D) can be partitioned into 3 time-term components (Farrell

and Euwema, 1984):

$$T_{AD} = T_{AB} + T_{BC} + T_{CD} \tag{4.11}$$

Equation (4.11) may be written as:

$$T_{AD} = P_1 + P_2 + \frac{x \cos\alpha}{V_1} \tag{4.12}$$

where

$$P_1 = \frac{Z_1\sqrt{1 - \left(\frac{V_0}{V_1}\right)^2}}{V_0} \tag{4.13}$$

$$P_2 = \frac{Z_2\sqrt{1 - \left(\frac{V_0}{V_1}\right)^2}}{V_0} \tag{4.14}$$

P_1 and P_2 are the static time shifts associated with the shot and receiver, respectively. The refracted arrivals are usually corrected for linear moveout (LMO) by using an estimated refractor velocity V_1 and replacing each sample time t with the LMO-corrected time, $t' = t - x/V_1$ (Claerbout, 1985). The third term can be interpreted as residual linear moveout (Yilmaz, 1987). Since the third term contains no weathering layer structure components (Z_1 , Z_2 , V_0), any long wavelength static anomaly can be partitioned between the first and second terms (Farrell and Euwema, 1984).

For shallow dip angles ($\cos\alpha \approx 1$), equation (4.12) may be simplified to:

$$T_{AD} = P_1 + P_2 + \frac{x}{V_1} \tag{4.15}$$

For station x_1 positioned at A, and station x_2 positioned at D, equation (4.15) becomes:

$$T_{AD} = P_1 + P_2 + \frac{x_2 - x_1}{V_1} \tag{4.16}$$

A laterally varying refractor velocity may be approximated using a least squares procedure. The reciprocal of the refractor velocity is expanded to a quadratic or cubic power of the station number along the seismic line (Farrell and Euwema, 1984). This may be described as:

$$\frac{1}{V_1} = a + bx + cx^2 + dx^3 \qquad (4.17)$$

where x is the station number.

The traveltime using the laterally varying velocity is given by:

$$T_{AD} = P_1 + P_2 + \int_{x_1}^{x_2} \frac{dx}{V_1(x)} \qquad (4.18)$$

Replacing the velocity term with the cubic polynomial (Eqn. 4.17) and evaluating the integral between the limits x_1 and x_2 results in:

$$\begin{aligned} T_{AD} = P_1 + P_2 + (x_2 - x_1) \cdot \\ \{a + \frac{b}{2}(x_2 + x_1) \\ + \frac{c}{3}(x_2^2 + x_2 x_1 + x_1^2) \\ + \frac{d}{4}(x_2^3 + x_2^2 x_1 + x_2 x_1^2 + x_1^3)\} \end{aligned} \qquad (4.19)$$

The first break picks are organized in a matrix of linear equations, with rows in the form equation (4.19) (Camina and Janacek, 1984). These equations are solved in a least-squares sense for the weathering layer depth and weathering velocity at the shot and receiver locations. Using the depth and velocity values, the refraction statics corrections for the shots and receivers are computed. These corrections are then applied to the data by performing a bulk time shift to each trace, as determined by the calculated static corrections.

A similar approach is used for the multiple layer case. For each layer, minimum and maximum offset limits are specified to ensure that the picked first arrivals correspond to the appropriate interface.

Figure 4.3 shows a CMP stacked section before and after application of refraction static corrections. Note the significant improvement in coherency of the shallow, high frequency events in the window CMP's 6055 - 6655, between 0,5 - 1,25 s. Coherency and continuity of seismic events is generally improved throughout the section. A marked improvement in the continuity of the medium wavelength events occurring between 1,5 and 2,5 seconds is also noted.

4.4.2 *REFRACTION STATICS ANALYSIS*

The quality and coherency of the stacked section was the criteria by which the application of refraction statics was judged. During the analysis, two variables were evaluated; weathering velocity initial value, and the number of refractors. The refraction static corrections were then applied to the data, followed by stacking in the common midpoint domain. The interpretability of each stacked section was then evaluated. The parameters corresponding to the most effective static correction were then used in further processing.

The weathering velocity initial values used for the testing were 3500, 4500 and 5800 m/s. In all cases, the velocity of the refractor was maintained at 6000 m/s as an initial constant velocity stack using this velocity showed acceptable coherency. Refraction statics corrections were calculated for each initial velocity, for conditions of one and two refracting layers.

The differences in the quality of the stacks were subtle for the tests conducted. It was determined, however, that there appeared to be a general improvement in interpretability for all velocity cases when a single refracting layer was specified. Of the single refractor tests, that using a initial value of 3500 m/s for the weathering velocity appeared to provide slightly better results.

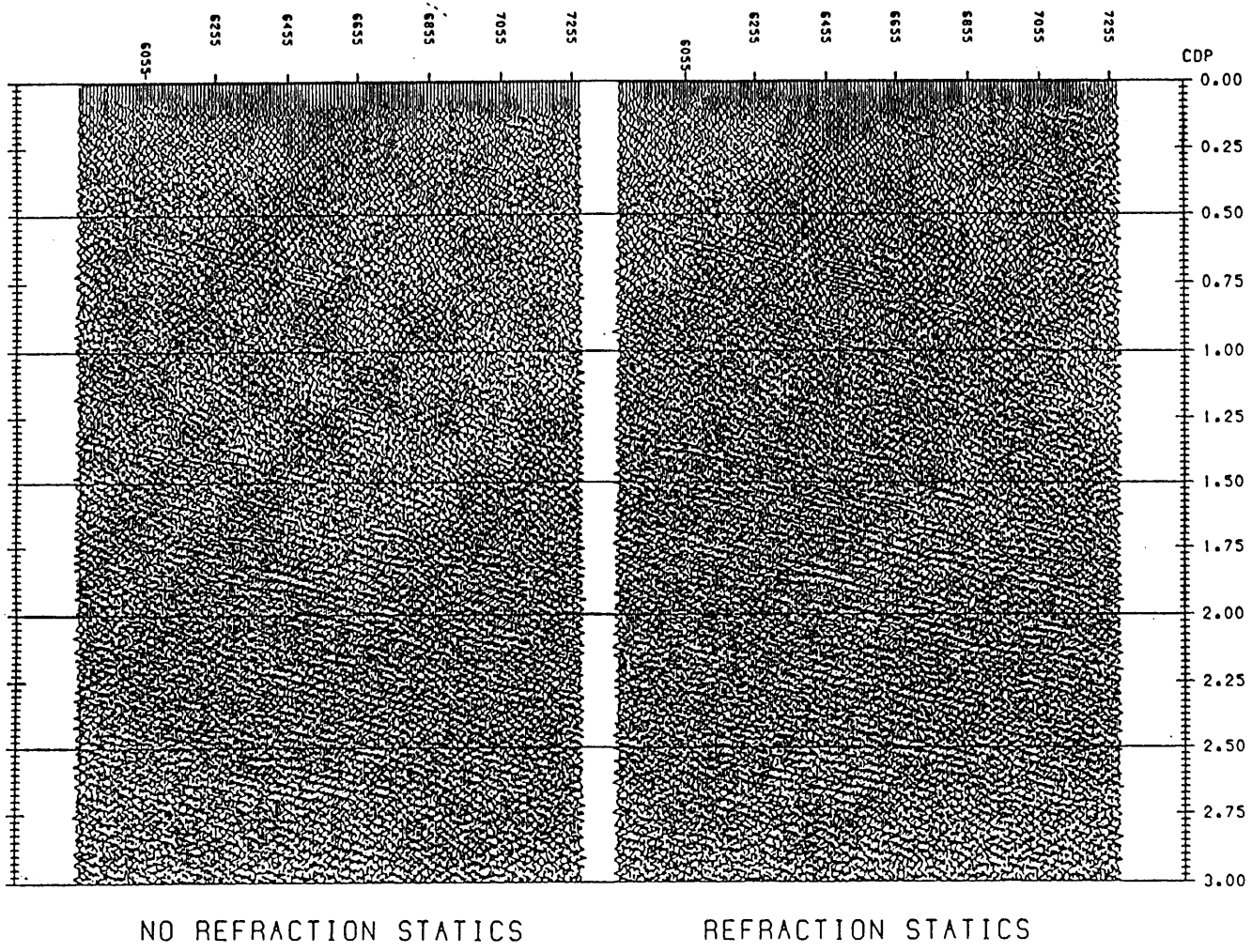

Fig. 4.3 Stacked section before and after the application of refraction static corrections. In general, an improvement in the continuity of events occurs in the time section.

Figure 4.4 illustrates the improvement in the stacked section using static corrections obtained with the single refractor assumption, and a weathering velocity of 3500 m/s. In comparison to the case of the single refracting layer with weathering velocity starting value of 4500 m/s, there is a small improvement in the coherency of the dipping events. A more significant improvement is noted when a comparison is made to the double refracting layer case; the continuity of the prominent event dipping from left to right between 1,4 s and 2,0 s is degraded when using the double layer assumption. A general decrease in the coherency of both shallow and deep events is observed over the seismic section.

4.5 VELOCITY ANALYSIS

Velocity analysis is the process whereby the stacking velocity function to be used in normal moveout (NMO) correction is estimated (Sheriff, 1984). Correction for NMO (normal moveout) is necessitated since the event image of a reflector in the CMP gather occurs at increasingly longer traveltimes with increasing source-receiver offset. NMO corrections attempt to remove the offset dependance of traveltimes in the CMP gather, thereby approximating a zero-offset representation of the event on the CMP gather (Yilmaz, 1987). Horizontal stacking of the NMO corrected CMP traces results in a maximum amplitude for a given reflection event.

The stacking velocity was estimated using both velocity semblance and constant velocity analysis methods.

In this section the following are reviewed:

1. NMO correction;
2. velocity analysis techniques; and
3. practical application of the techniques to the CMP gathered data.

Fig. 4.4 Stacked sections illustrating results of refraction static testing for single and multiple refracting layers. There is an improvement in event coherency using the single refractor model with 3500 m/s velocity.

4.5.1 *NORMAL MOVEOUT*

The hyperbolic approximation to the NMO curve

Using the geometry shown in Figure 4.5, the NMO correction may be derived for the single layer case. The model consists of a homogeneous layer having seismic velocity v, with a reflecting interface at the base. The variable x represents the source-receiver offset. The recorded two-way traveltime is given by t, and the zero-offset two-way traveltime is given by t_0.

From the geometry shown in Figure 4.5:

$$t^2 = t_0^2 + \left(\frac{x}{v}\right)^2 \qquad (4.20)$$

(Yilmaz, 1987)

which is a hyperbolic equation.

For a single constant-velocity layer, the travel time curve as a function of offset is a hyperbola (Yilmaz, 1987). Velocity analysis is based upon this assumption.

Correction for the NMO effect

The magnitude of the NMO correction is given by the difference between the source-receiver offset two-way traveltime and the zero-offset two-way traveltime (Yilmaz, 1987):

$$\Delta t_{NMO} = t - t_0 \qquad (4.21)$$

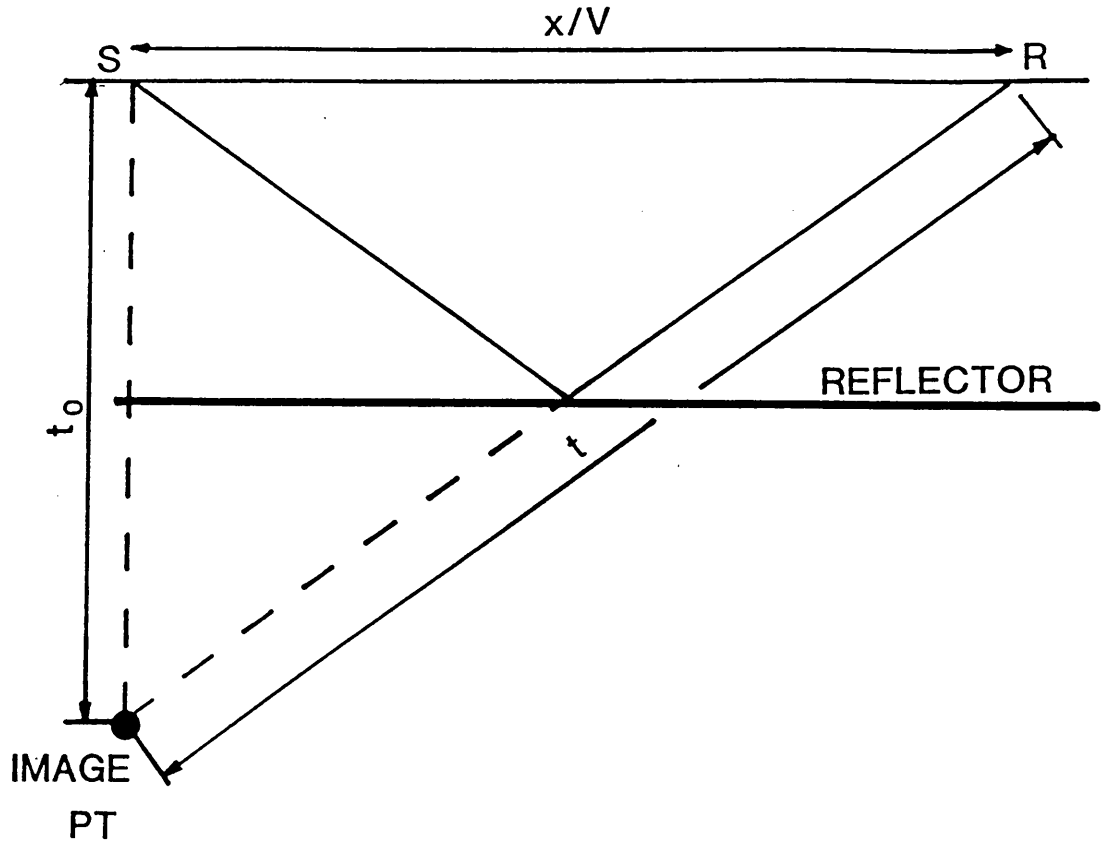

Fig. 4.5 Earth model illustrating the hyperbolic correction for NMO. t is the recorded two-way traveltime; t_0 is the zero-offset two-way traveltime.

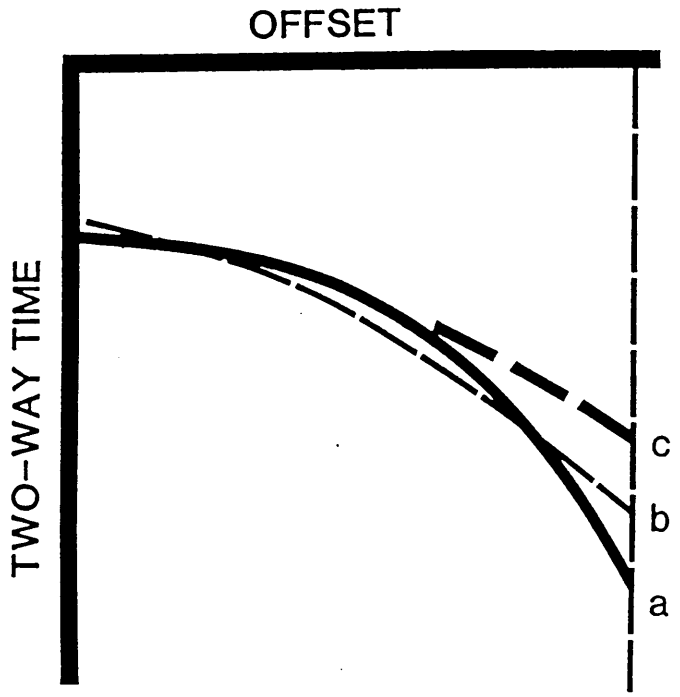

Fig. 4.6 Schematic of the small-spread and best-fit hyperbolae. "a" represents the recorded seismic event; "b" represents the best-fit hyperbola; "c" represents the small-spread hyperbola.

Substituting equation (4.20) into (4.21) results in the NMO equation (Yilmaz, 1987):

$$\Delta t_{NMO} = \sqrt{t_0^2 + \left(\frac{x}{v}\right)^2} - t_0 \qquad (4.22)$$

The NMO equation is generalized for a system of n horizontal layers in Appendix B.

Subject to the small-spread (Fig. 4.6) and small dip approximations (Yilmaz, 1987), for a system of n horizontal layers, the NMO equation (equation 4.22) may be written as:

$$\Delta t_{NMO} = \sqrt{t_0^2 + \left(\frac{x}{\overline{v}_n}\right)^2} - t_0 \qquad (4.23)$$

where $\overline{v}_n$ is the rms (root mean squared) velocity (Taner and Koehler, 1969; Al-Chalabi, 1973), as shown in Appendix B.

Figure 4.7 illustrates a CMP gather before and after the application of NMO corrections. Note how the events at 1,42 , 1,70 , and 2,30 seconds are flattened by application of the NMO corrections.

NMO stretch

As NMO correction is velocity dependent, a dynamic time shift is applied to the seismic trace. Thus, after the application of NMO correction, the waveform along the seismic trace may be stretched. This stretching is more severe at low velocities and large offsets (Yilmaz, 1987).

The NMO-corrected CMP gather shown in Figure 4.7 depicts NMO stretch at early times. Data from the first-break to approximately 0,4 s have been severely stretched by the application of the NMO correction. Data that have been stretched excessively must be muted out to prevent distortion and contamination of the data during stacking (Yilmaz, 1987). This is generally implemented in the NMO correction process by specifying a threshold stretching factor.

4.5.2 *SELECTION OF STACKING VELOCITIES*

Two methods of choosing stacking velocities commonly used are:

1. velocity spectrum analysis; and
2. constant velocity stack methods.

Velocity spectrum analysis

For a given stacking velocity, lateral signal coherency is computed by stacking a CMP gather along a hyperbolic trajectory calculated from the NMO equation (Taner and Koehler, 1969). This procedure is carried out for all times, and for a range of stacking velocities. Semblance values are calculated horizontally from the NMO corrected CMP stacks (for a given velocity value) and this trace of semblance values becomes a single trace in the semblance gather. The semblance gather is a velocity versus two-way traveltime plot, with contoured semblance values (Yilmaz, 1987).

Velocity-time pairs corresponding to maximum coherence are picked from the spectra. This process is repeated at a number of CMP positions along the line. In this manner a velocity function for the entire line may be determined. Velocity spectrum analysis suffers from a lack of resolution in regions characterized by high seismic velocities with relatively low variation of velocity with depth. For this reason velocity spectrum analysis proved to be unsuitable for use on the P1-86 data set.

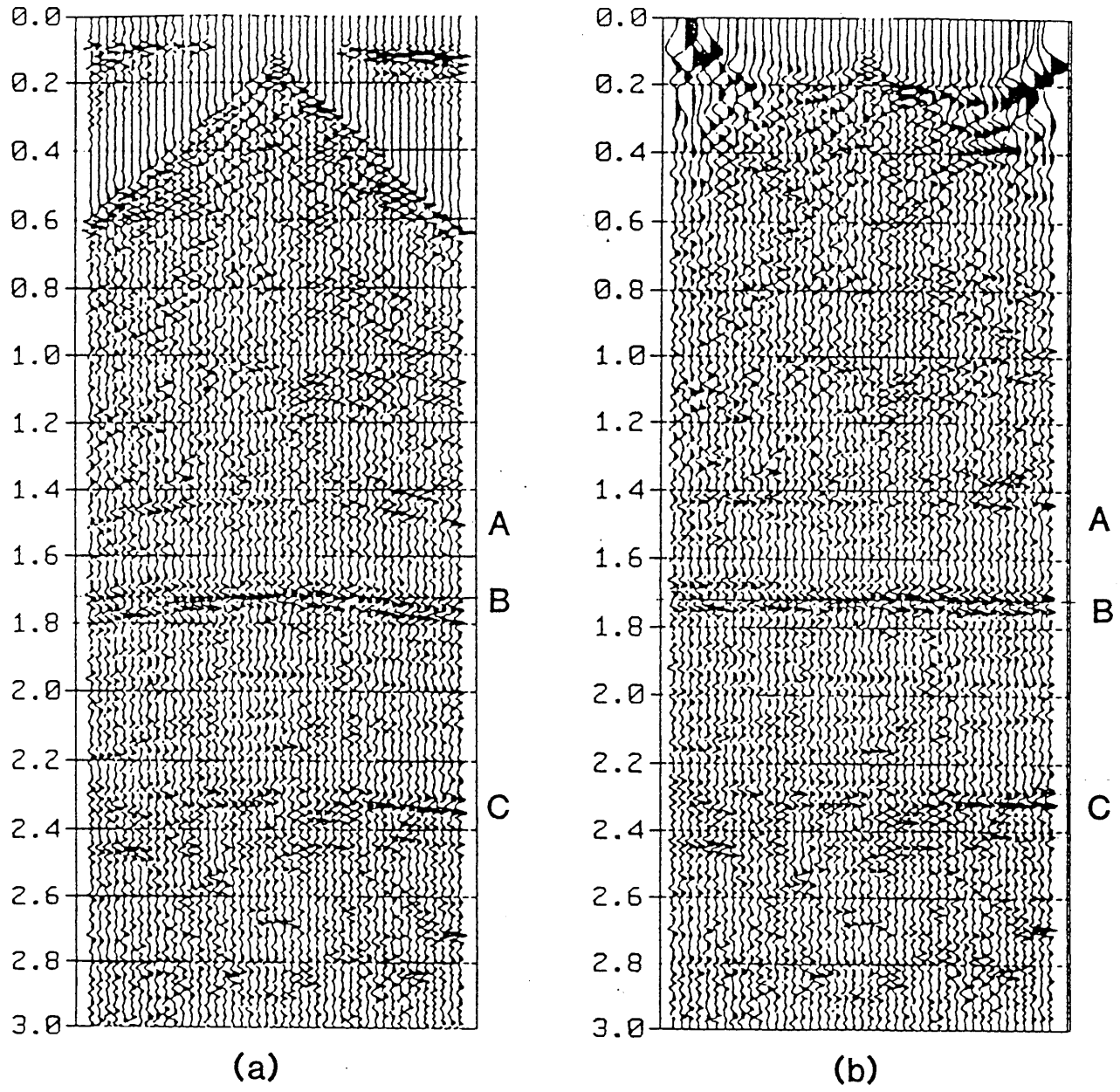

Fig. 4.7 CMP gather (a) before, and (b) after the application of NMO correction. Events at A, B, and C are flattened by application of NMO correction. Data from the first break to approximately 0,4 s on the NMO corrected record have been NMO stretched excessively.

Constant velocity stacks (CVS)

There are two approaches to choosing stacking velocities using constant velocity stacks. The first involves NMO-correcting and stacking a small number of CMP gathers repeatedly, (typically 5-10) using a series of constant velocities (Yilmaz, 1987). The NMO corrected gathers are evaluated, and the velocity which best flattens a given event is chosen as the stacking velocity for that event. By making this comparison for each event, one may construct a stacking velocity versus time function which would align the events in the CMP stack. This approach is suitable in regions of shallow dip and slow lateral structural variations.

The second approach to constant velocity stacks (CVS) is more appropriate for regions of complex structure and lateral structural variation. A relatively large section of the seismic data is repeatedly NMO corrected and stacked using a range of stacking velocities. For each event, stacking velocities are picked directly from the stacked section displaying greatest coherency and interpretability.

This "global" CVS method provided the best results of the three velocity analysis methods tested on this data. The *entire seismic section* was NMO corrected and stacked using a range of velocities which varied from 5000 m/s to 8000 m/s in increments of 500m/s, and from 8000 m/s to 10 000 m/s in increments of 1000 m/s. These stacked sections were evaluated for coherency and resolution and, based on the interpretive results, a velocity function was compiled for the entire survey. Selected panels from the CVS tests are depicted in Figure 4.8. Note that the events between CMP's 2855 - 3255 and times 0,0 - 0,75 s are best corrected for NMO using a stacking velocity of 6000 m/s. For stacking velocities over 6000 m/s these events are under corrected and thus stack incoherently. Also note that deeper events are NMO corrected more successfully at higher velocities.

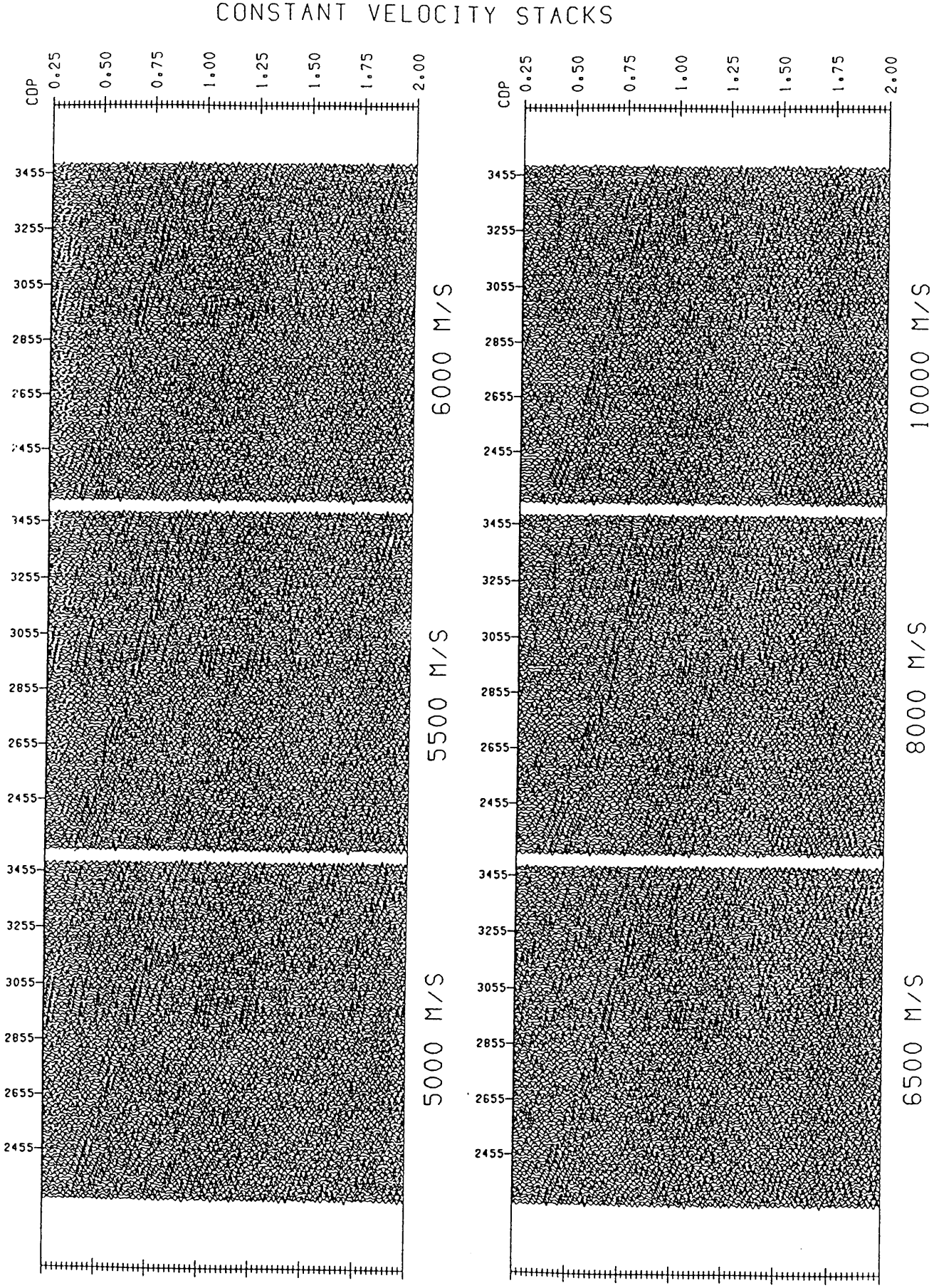

Fig. 4.8 Constant velocity stacks illustrating an improvement in stacking quality at low velocities for shallow events, and at higher velocities for deeper events.

Global CVS methods are more suitable in areas of complex structure and in areas characterized by high seismic velocities, where the relative increase in stacking velocity with depth is small. These global CVS methods appear to provide better resolution of stacking velocities than do spectral analysis methods or the CVS method which utilizes 5-10 CMP gathers.

The CVS method is particularly useful in that it allows the interpreter to directly pick stacking velocities which correspond to maximum continuity and interpretability of an event.

4.6 DECONVOLUTION

The objective of deconvolution is to improve the temporal resolution of the stacked seismic section (Berkhout, 1981; Yilmaz, 1987).

The following aspects of deconvolution will be reviewed:

1. the convolutional model;
2. inverse filtering;
3. least-squares filter;
4. phase considerations; and
5. trace and gather oriented deconvolution.

4.6.1 *CONVOLUTIONAL MODEL*

Deconvolution is based upon the convolutional model (Yilmaz, 1987; Russel, 1988) for the seismic trace (Appendix C). The convolutional model for a seismic trace is expressed as:

$$x_t = rc_t * w_t + n_t \tag{4.24}$$

where x_t is the seismic trace, rc_t is the reflection coefficient time series, w_t is the seismic wavelet, and n_t is random noise (Fig. 4.9).

Assumptions in the convolutional model are:

1. the earth is made up of horizontal layers of constant velocity (Yilmaz, 1987);
2. only P-wave reflection and transmission occur (Yilmaz, 1987);
3. the waveform of the source is stationary (Yilmaz, 1987);
4. the noise component is white (Stone, 1977); and
5. the reflection coefficient time series is white (Claerbout, 1985).

Although the above assumptions may be violated in many cases (areas of complex structure or lateral facies changes), the convolutional model has proven to be a sound base on which to develop the theory of deconvolution (Russel, 1988).

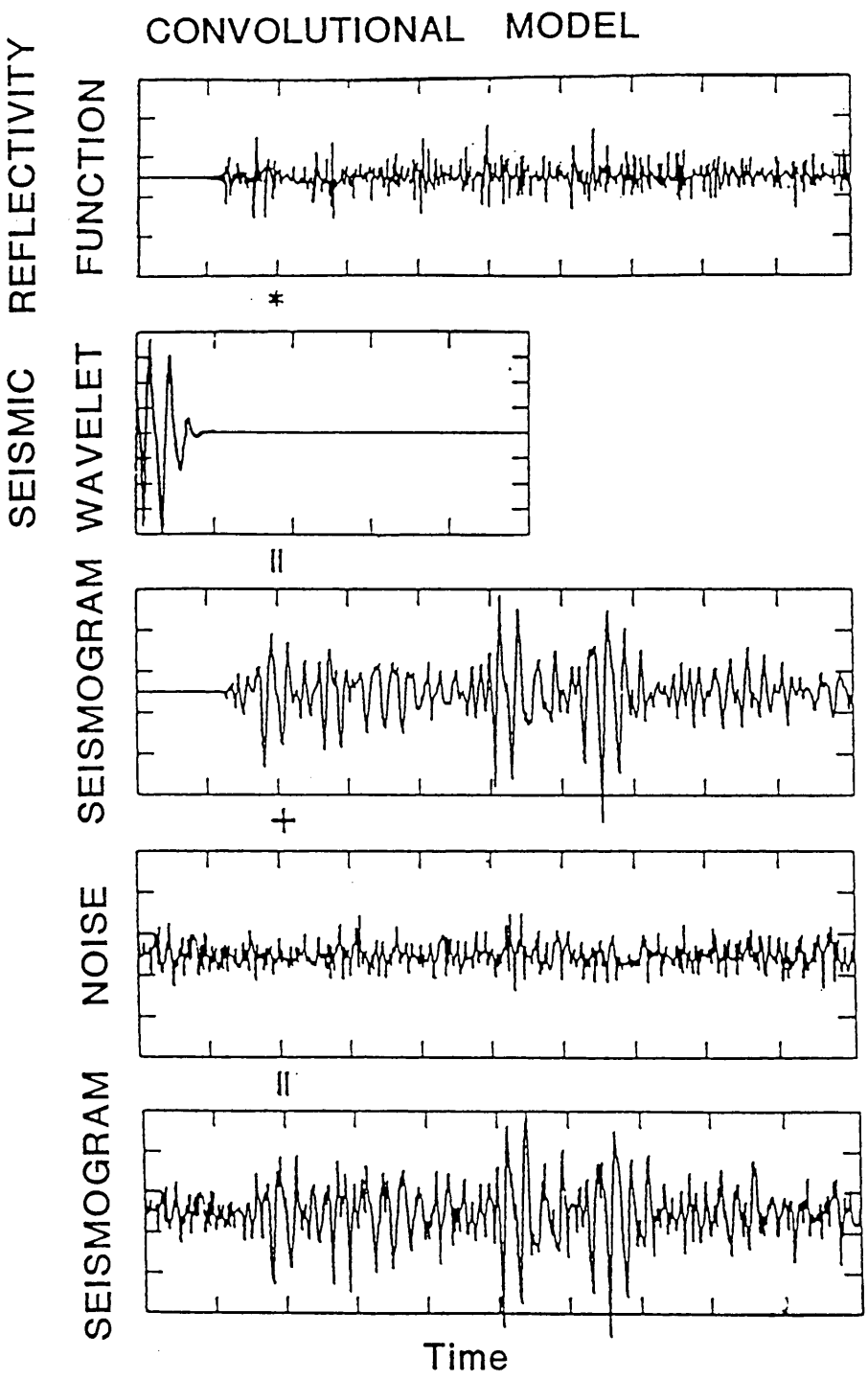

Fig. 4.9 Convolutional model (after Yilmaz, 1987).

4.6.2 *INVERSE FILTERING*

Deconvolution may be viewed as convolving the seismic trace with an inverse representation of the seismic wavelet, with the purpose of retrieving the reflectivity function from the seismic trace (Sheriff and Geldart, 1983).

The seismic wavelet may be determined using the autocorrelation of the convolutional model of the seismic trace (Yilmaz, 1987; Russel, 1988):

$$\Phi_{xx} = \Phi_{ww} * \Phi_{rc\,rc} + \Phi_{nn} \tag{4.25}$$

The reflection coefficient time series and the noise are assumed to be random (white) (Stone, 1977; Claerbout, 1985). Ignoring the constants $\Phi_{rc\,rc}$ and Φ_{nn}, resulting from the autocorrelation, equation (4.25) may thus be rewritten:

$$\Phi_{xx} \approx \Phi_{ww} \tag{4.26}$$

Assuming w_t to be minimum phase (Yilmaz. 1987), it is possible to design an operator (the inverse filter of w_t) that will remove the seismic wavelet from the seismic trace.

4.6.3 *LEAST SQUARES (WIENER) FILTER*

Due to assumptions made in both the convolutional model of the seismic trace and the inverse filter theory, the inverse filter obtained is not the filter required to perfectly remove the seismic wavelet from the seismic trace. The method of least-squares is used to design a filter that will most accurately reproduce a desired output from the input. Such a filter known as the optimum filter (Robinson and Treitel, 1967) or the Wiener filter (named after Norbert Wiener, who first used this technique).

The set of linear simultaneous equations, whose solution represents a least-squares fit to the data, is known as the normal equations (Appendix D) for the least-squares filter (Sheriff, 1984). During this research the Levinson recursion algorithm (Levinson, 1947; Claerbout, 1976) was used in order to solve the normal equations for the least-squares filter.

4.6.4 *TRACE AND GATHER ORIENTED DECONVOLUTION*

Deconvolution may be applied in either a gather oriented or a trace oriented sense. During gather oriented deconvolution, a single deconvolution operator is designed for each shot or receiver gather. This "averaged" operator is then applied to each trace in the gather. During trace oriented deconvolution, however, a deconvolution operator is designed for each individual trace. Each seismic trace is then deconvolved by application of that traces unique operator.

Trace oriented deconvolution is generally used when lateral variations in the seismic wavelet are inherent in the common shot or receiver gathers. Gather oriented deconvolution implies that the lateral variation in the frequency spectrum of the deconvolution operator may be approximated through a smoothed average, using all the traces in the gather.

Both gather and trace oriented deconvolution were tested on the P1-86 seismic data and the results evaluated. Application of trace oriented deconvolution to the data resulted in an improvement in lateral coherency of events, and generally improved interpretability of the stacked section (Fig. 4.10). The prominent marker observed between approximately 0,25 s at CMP 1455 to approximately 2,0 s at CMP 5255 is more continuous and easier to interpret than on the gather oriented deconvolved section. The seismic signature of the event is more consistent, allowing greater confidence in interpretation across discontinuities. The events occurring from 0,75 s to 1,5 s between CMP's 4455 and 5255 show greater coherency and much of the reverbatory nature of the signal has been removed. An improvement is noted in the continuity

and interpretability of the lower amplitude, northerly dipping events below the most prominent marker, between CMP 1255 and CMP 2655. These events can be followed with some confidence, despite the presence of linear noise.

Since trace oriented deconvolution provided significantly improved results, a laterally varying acoustic impedance is inferred for the subsurface. The effect of the earth filter on the spectral characteristics of the seismic wavelet, or the coupling of the source to the surface, may also be inferred to vary laterally.

Although computationally more expensive, trace oriented deconvolution merits application in regions of complex structure and lateral velocity variations.

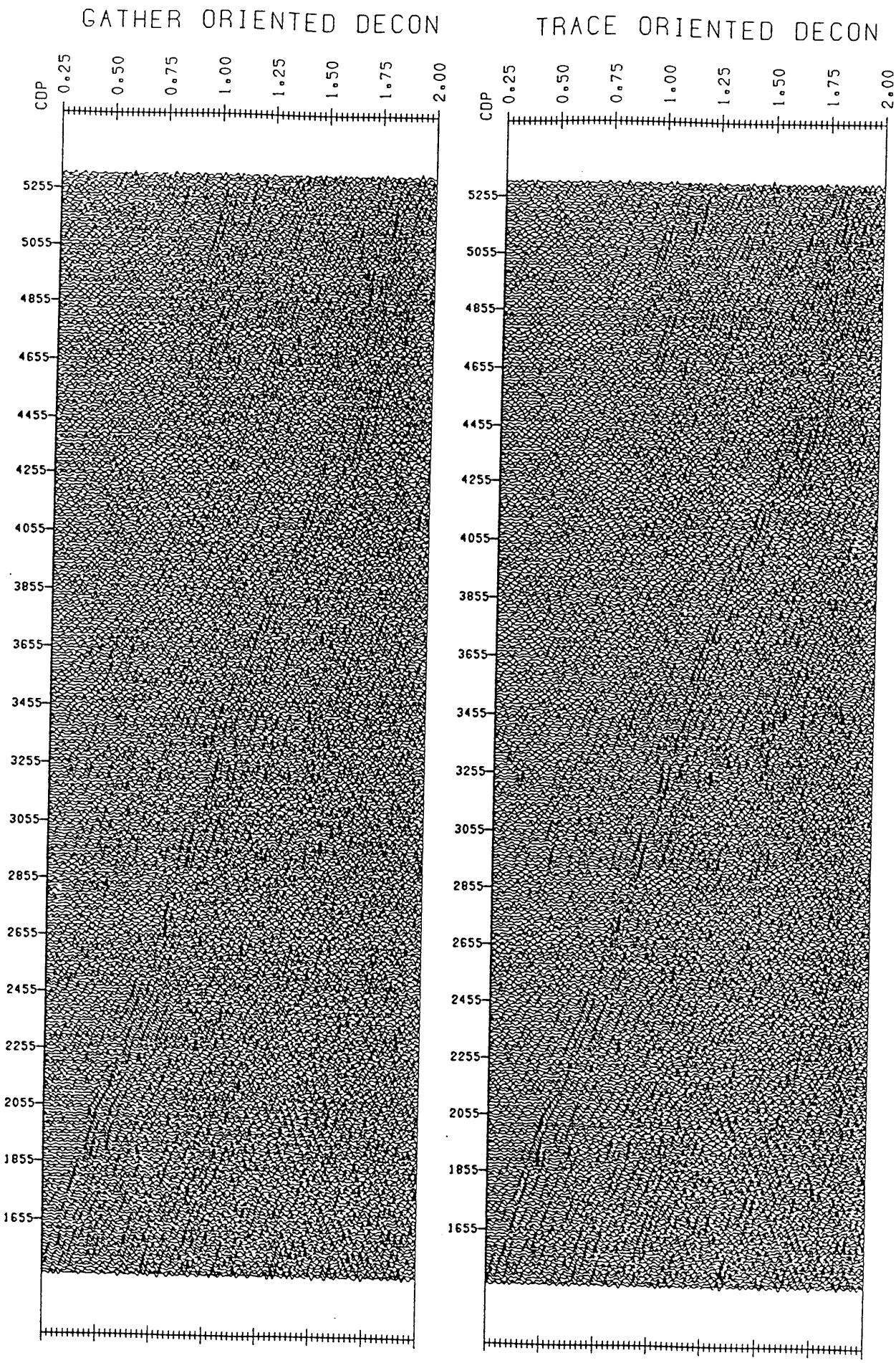

Fig. 4.10 Gather and trace oriented deconvolution applied to the data. Application of trace oriented deconvolution resulted in an improvement in coherency.

CHAPTER 5

POSTSTACK PROCESSING

5.1 BRUTE STACK

Several areas of interest were identified on the brute stack seismic section. The characteristics of these features constrained the poststack processing parameter selection. This method of parameter selection forms the basis of interpretive processing.

The seismic events annotated on the brute stack section (Fig. 5.1a, b, c) were those identified as being of primary interest:

Event 1. The high amplitude seismic event (Fig. 5.1a), which dips northwards from the southern limit of the line at approximately 0,25 s, to 1,5 s at CMP 4255.

Event 2. Relatively high frequency package of northerly dipping events occurring from 0,5 s at CMP 5855, to 1,0 s at CMP 7255 (Fig. 5.1a).

Event 3. The high amplitude events occurring between 1,25 s and 2,0 s at CMP 6055, dipping northwards to between 1,5 s and 2,75 s at CMP 7055 (Fig. 5.1a).

Event 4. The isolated high amplitude, relatively low frequency event extending from approximately 2,4 s at CMP 3055, to approximately 2,8 s at CMP 3855 (Fig. 5.1a).

Event 5. The high amplitude, relatively low frequency event occurring at approximately 3,2 s between CMP 5855 and CMP 6855 (Fig. 5.1a).

Event 6. Diffractions, the apex of which is at approximately 0,85 s, at CMP 9855 (Fig. 5.1b).

Event 7. Diffractions, the apex of which is at approximately 1,6 s, at CMP 11455 (Fig. 5.1b).

Event 8. The high amplitude, relatively low frequency event at approximately 3,2 s at CMP 17055 (Fig. 5.1c).

Event 9. The sequence of high amplitude events to the north of CMP 20255, observed from 3,0 s down to 4,5 s (Fig. 5.1c).

Interpretive poststack processing proceeded in an attempt to analyze the effect of the processing steps on the seismic events identified above. Comparison of the input and output data for a particular process enabled decisions to be made as to whether the processing had improved the interpretation of the data, or whether the processing had complicated the interpretation by introducing processing artifacts.

5.2 RESIDUAL STATICS

Lateral velocity variations and near surface inhomogeneities cause the moveout of an event in a CMP gather to deviate from an idealized hyperbolic shape (Rogers, 1985; Yilmaz, 1987). This deviation from hyperbolic moveout results in static distortions in the NMO corrected CMP gathers. Such static distortions manifest themselves as poorly defined stacked traces. To improve stacking quality, the calculation of residual statics corrections is performed on the NMO corrected CMP gathers in a surface consistent manner; static shifts are dependant only on the shot and receiver locations, and *not on the raypaths travelled* (Yilmaz, 1987). The calculated residual static corrections are applied to the CMP gathers having no NMO correction. Velocity analysis may be repeated to improve the choice of stacking velocities (Sheriff and Geldart, 1983; Rogers, 1985), and hence the quality of the stacked section.

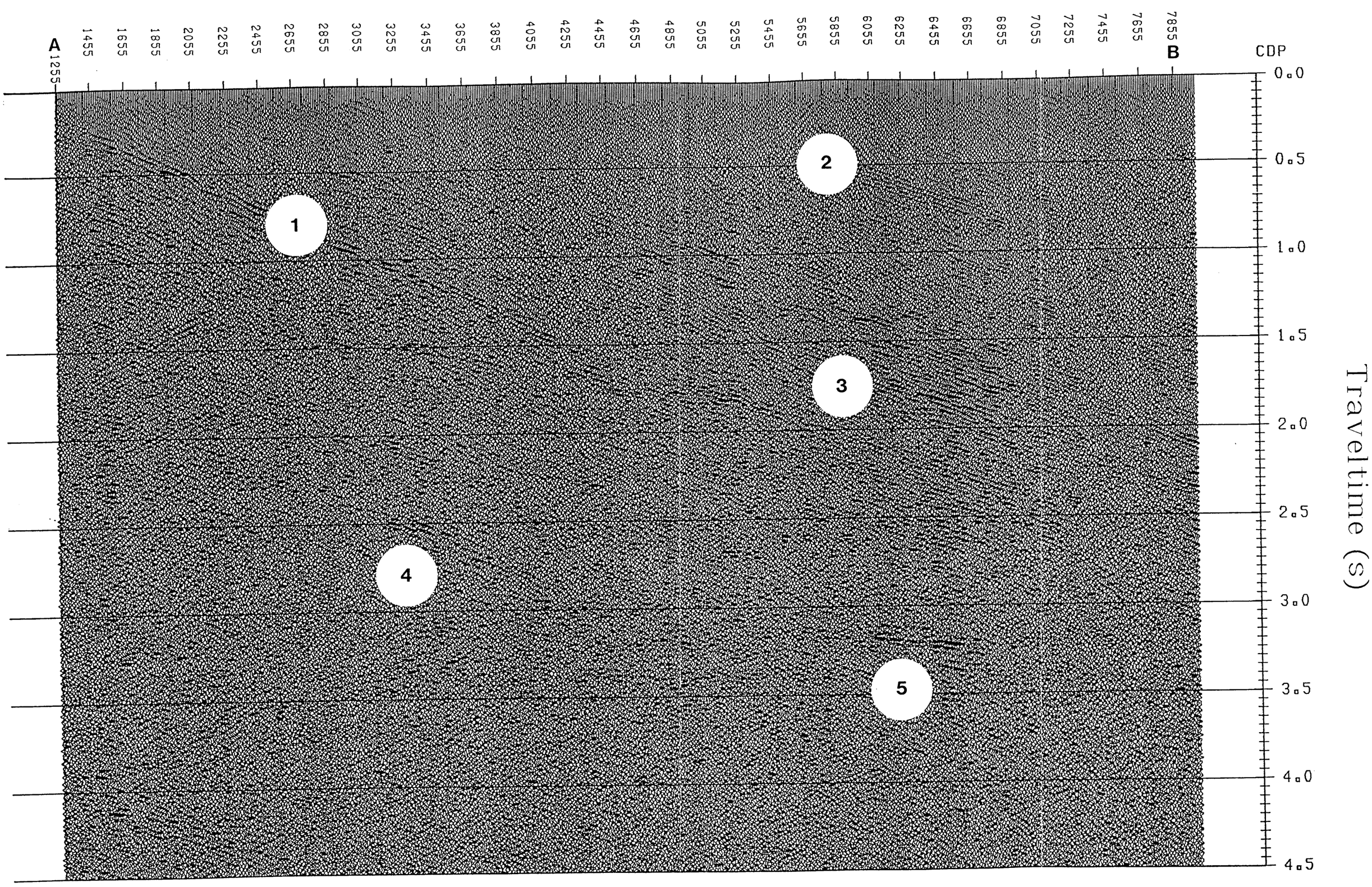

Fig. 5.1a Brute stack section displaying events of primary interest (section A-B on Fig. 2.2).

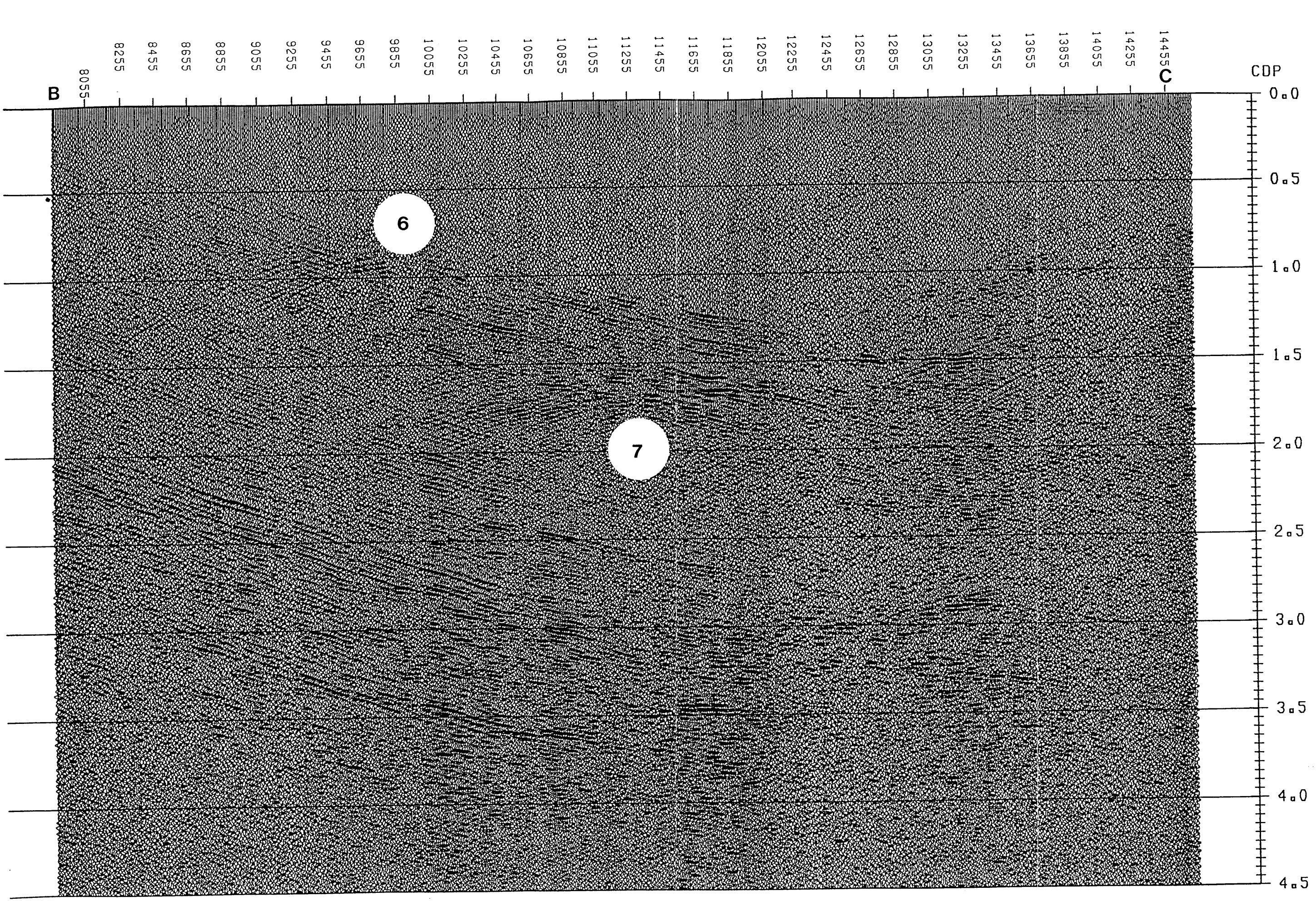

Fig. 5.1b Brute stack section displaying events of primary interest (section B-C on Fig. 2.2).

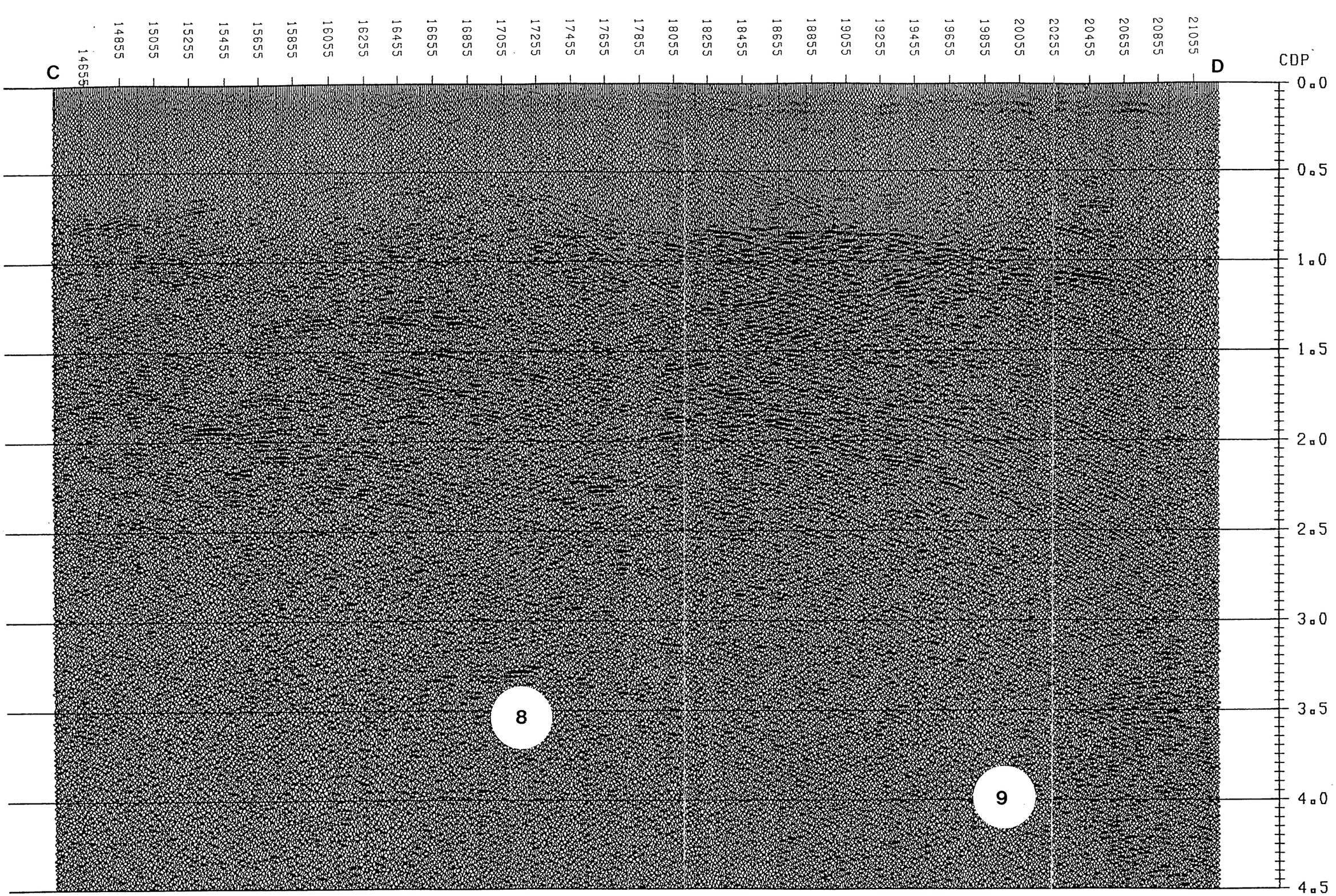

Fig. 5.1c Brute stack section displaying events of primary interest (section C-D on Fig. 2.2).

The residual static correction algorithm is based on the Dahl-Jensen modification (1989) to the method of Ronen and Claerbout (1985). Ronen and Claerbout consider methods based directly on the crosscorrelation of traveltimes to be susceptible to failure in the presence of ambiguities or noise.

The use of the crosscorrelation method in residual static calculation, is based on the proposition that the time delay corresponding to the maximum amplitude of a time series, resulting from the crosscorrelation between two similar traces, indicates the optimal time shift that can be used to physically align the traces along maximum coherency (Foster and Guinzy, 1967).

Ronen and Claerbout propose that the estimation of the surface-consistent statics by maximization of the sum of squares (power) of the stacked section is a better measure of quality, especially in the case of a low signal-to-noise ratio. The method of Ronen and Claerbout evaluates surface consistent static shifts by comparing the power of a "super trace", constructed using all the traces in the shot profile in sequence, with that of a super trace consisting of the CMP stacked traces to which each shot profile contributes. The maximum of the crosscorrelation between the two super traces is then picked as the relative time shift to be applied in the residual static correction.

Dahl-Jensen (1989) suggests that the existence of local maxima in the stack power may result in incorrect alignment of signal peaks if the search for the maximum stack power is localized. The existence of local maxima may be attributed to noise spikes and the choice of the detection threshold. A modified approach to the method of super trace crosscorrelation uses a randomly varying sequence of parameters within each iteration, in order to improve the likelihood of obtaining a global stack power maximum.

As the method employed to calculate residual static corrections depends upon obtaining a stack power maximum (Ronen and Claerbout, 1985; Dahl-Jensen, 1989), the method is susceptible to failure in the presence of high amplitude

linear noise. The calculated static shifts may thus be determined on maximum coherency of the linear noise. The design window in which the stack power is to be maximized should therefore be selected in regions displaying little linear noise.

Figure 5.2a, b, and c shows the CMP stacked section after the application of residual static corrections. Seismic events 1 - 9 are those annotated in Figure 5.1a, b, and c. The seismic section shows a marked improvement in continuity of events. The design window was chosen outside regions of linear noise in order to preferentially enhance seismic events.

5.3 MIGRATION

Migration locates events on a seismic section in their true spatial positions by collapsing hyperbolic diffractions to the diffractor, and by correcting for the distortion in position and amplitude of dipping reflectors observed on non-migrated data (Berkhout, 1981; Sheriff, 1984; Claerbout, 1985; Yilmaz, 1987).

Since a stacked section is assumed to be equivalent to a zero-offset seismic survey, zero-offset traces may be used to illustrate the effect of migration on the spatial characteristics of the seismic event of a dipping reflector (Yilmaz, 1987). In Figure 5.3, two zero-offset rays originating at points A and B are reflected off a dipping reflector at points C and D, respectively. The two seismic traces containing the reflection event are plotted directly beneath geophone locations A and B (at their apparent positions C' and D'), rather than in the true spatial positions, C and D, respectively. Migration attempts to translate the reflection segment C'D' below A and B, to the true spatial position CD. Migration of a dipping layer moves the reflection segment updip, increasing the dip and shortening the segment. This results in an improvement in the resolution of the shape and position of a reflector (Berkhout, 1981; Yilmaz, 1987). Diffraction energy is migrated towards the apex of the hyperbolic diffraction curve (Berkhout, 1981; Yilmaz, 1987).

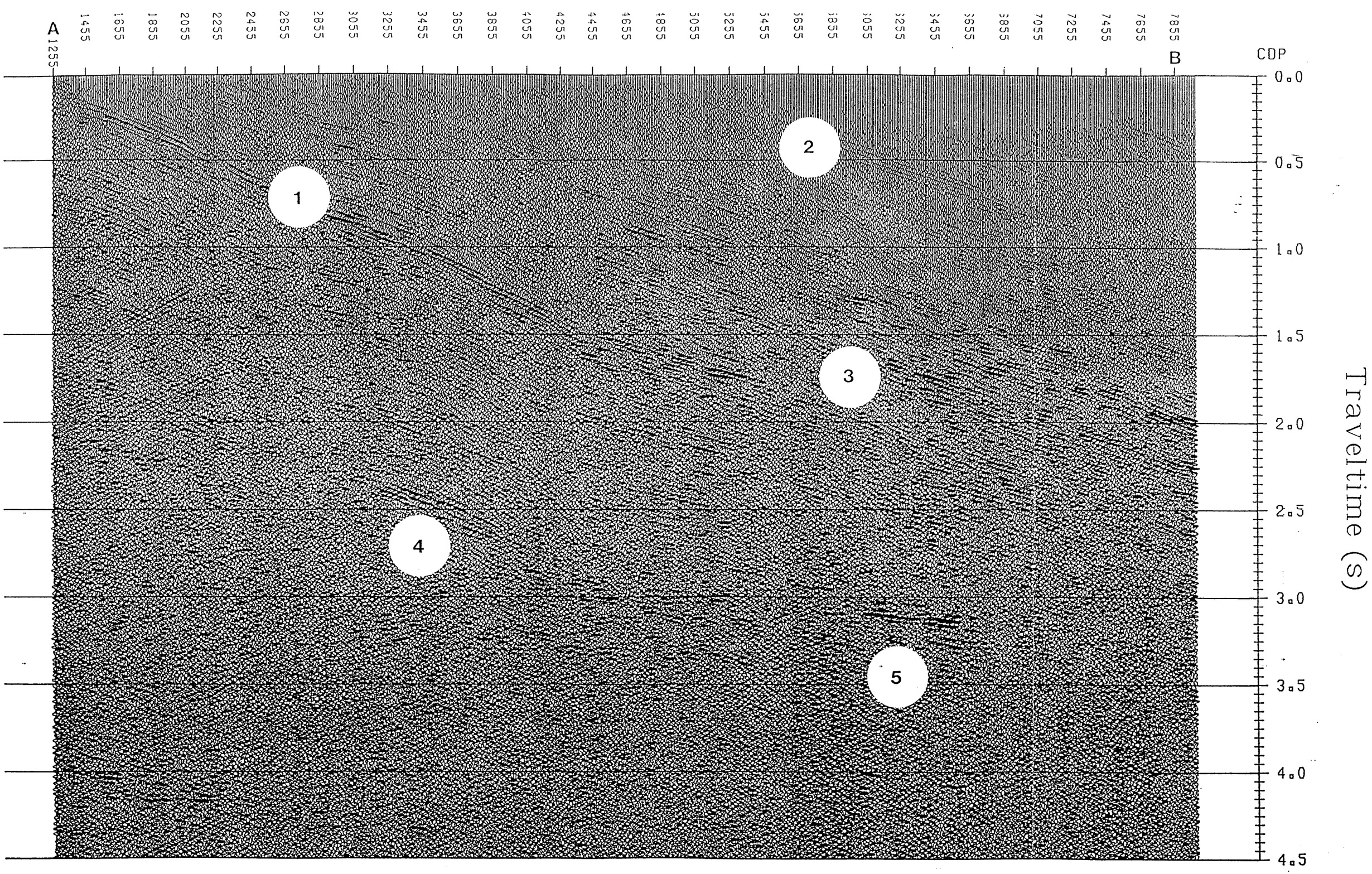

Fig. 5.2a CMP stacked section after the application of residual static corrections (section A-B on Fig. 2.2). The residual static corrected section shows a marked improvement in continuity of events in comparison to the brute stack section of figure 5.1.

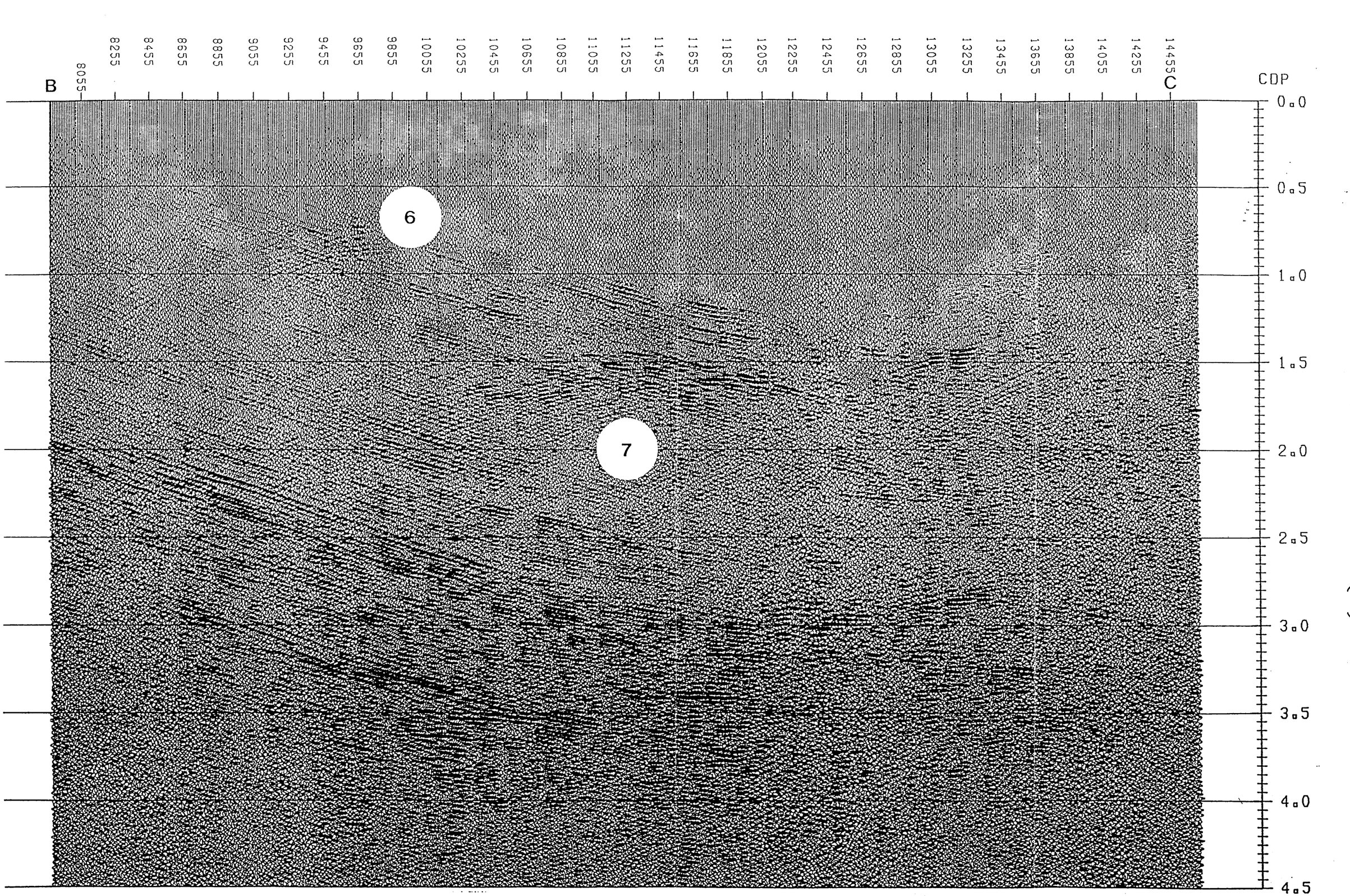

Fig. 5.2b CMP stacked section after the application of residual static corrections (section B-C on Fig. 2.2). The residual static corrected section shows a marked improvement in continuity of events in comparison to the brute stack section of figure 5.1.

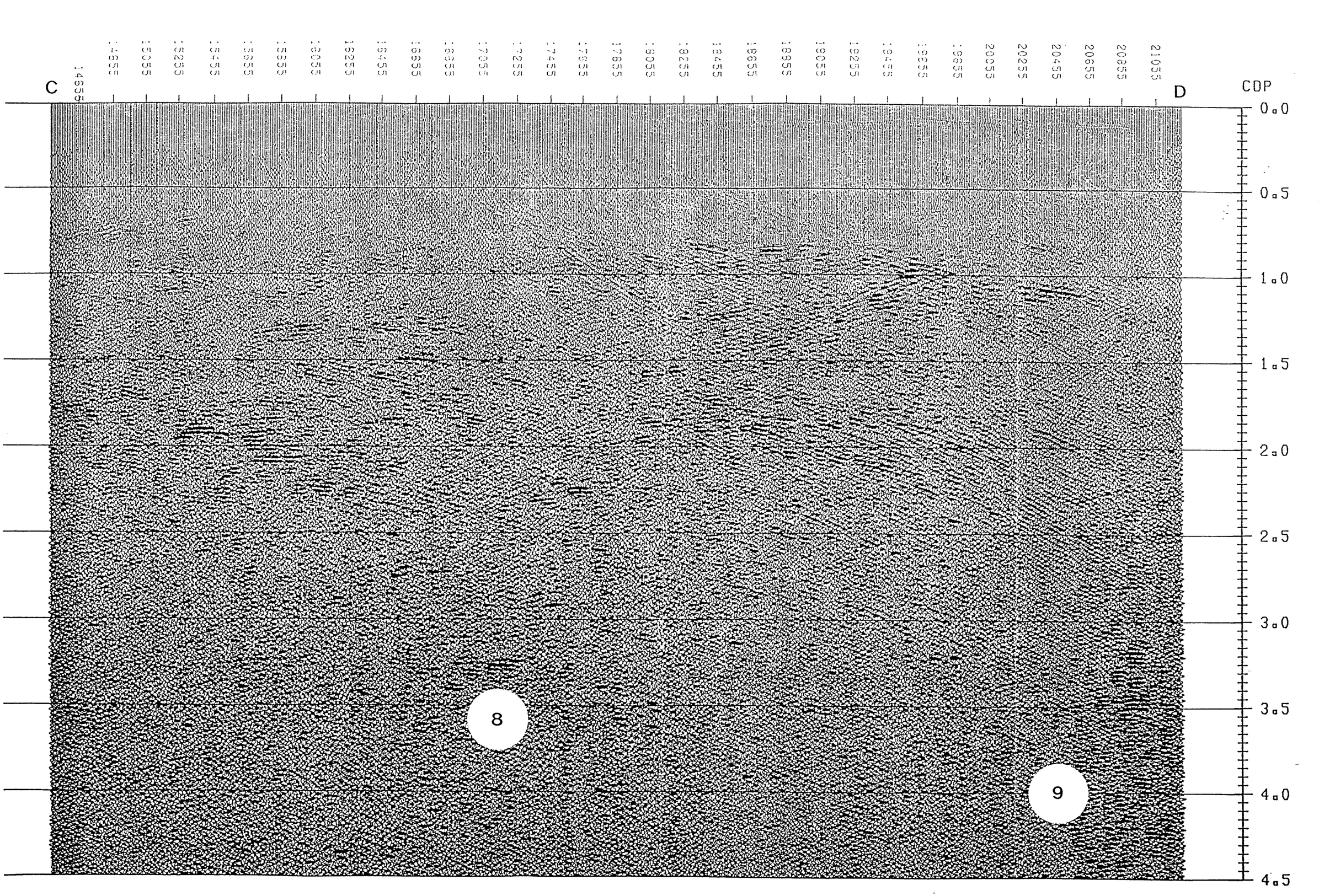

Fig. 5.2c CMP stacked section after the application of residual static corrections (section C-D on Fig. 2.2). The residual static corrected section shows a marked improvement in continuity of events in comparison to the brute stack section of figure 5.1.

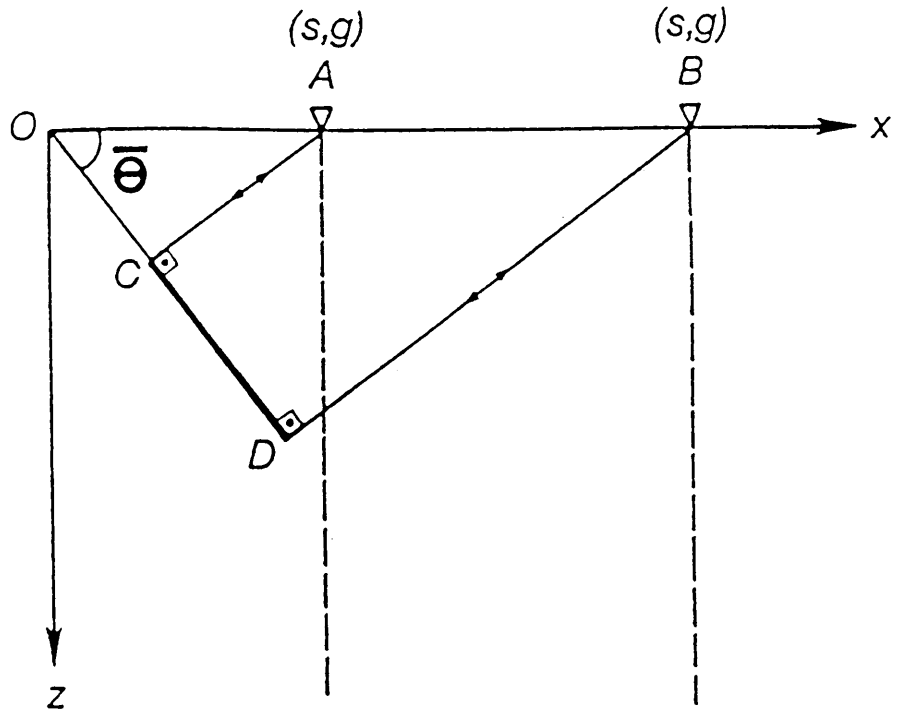

(a)

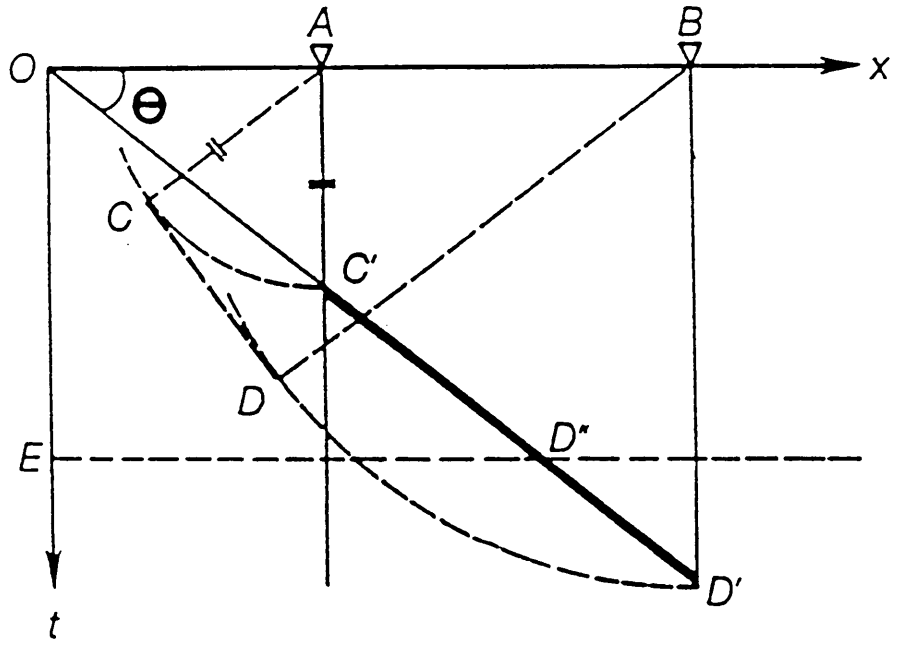

(b)

Fig. 5.3 Zero-offset representation of migration principles in the x-t domain. The reflection segment C'D' in the time section (b), when migrated, is moved updip, steepened, shortened, and mapped onto the true subsurface location CD (a) (after Chun and Jacewitz, 1981; Yilmaz, 1987).

Two migration techniques are:

1. wavefront migration; and
2. wave equation migration.

Wavefront migration is based on the superposition of semicircles upon the diffraction hyperbolae, while wave equation migration algorithms are based upon manipulations of the scalar wave equation (Loewenthal *et al.*, 1976). A list of migration algorithms includes:

1. the semicircle superposition method;
2. diffraction summation (Kirchoff) migration (Schneider, 1978);
3. finite difference migration (Claerbout, 1970);
4. frequency-wavenumber (F-K) migration (Stolt, 1978); and
5. phase-shift migration (Gazdag, 1978).

The migration methods used in the processing of the P1-86 seismic data are F-K migration and phase-shift migration (which is based upon F-K migration). F-K migration was used to evaluate the optimum migration velocity function, which was subsequently used in the phase-shift migration.

F-K migration and phase-shift migration are time migrations; the output time section allows direct comparison between pre- and post-migration data. Time migration methods are based on the assumption that lateral velocity variations are gradual (Gazdag, 1978; Stolt, 1978; Hosken and Deregowski, 1985; Yilmaz, 1987).

The review of migration is partitioned into the following topics:

1. the 2-D Fourier transform as the basis of frequency-wavenumber domain migration
2. the F-K (Stolt) migration algorithm;

3. the ability of F-K migration to deal with temporally varying velocity (Stolt stretch); and
4. phase-shift migration.

5.3.1 *THE 2-D FOURIER TRANSFORM*

In the F-K migration technique (Stolt, 1978), the data are transformed from the (x,t) domain to the (x,f) domain, and then to the (k,f) domain. The wavenumber, k, is the number of cycles per unit distance. The data P(x,z,t) are transformed to the migrated data $P(k_x,z,\omega)$ (Yilmaz, 1987) (Appendix E).

The inverse of the stepout (or slope) of a dipping linear seismic event in the (x,t) domain is equal to the frequency-wavenumber ratio associated with the event in the (k,f) domain (Yilmaz, 1987). This can be expressed

$$\frac{dx}{dt} = \frac{f}{k} \tag{5.1}$$

From this expression:

1. for a given dip, a change in temporal frequency of the event corresponds to a change in the spatial wavenumber;
2. for a given temporal frequency, steeper dips have greater spatial wavenumbers; and
3. an event containing a continuous range of frequencies maps as a radial line passing through the origin.

A convention used in the transformation of seismic data from the (x,t) plane to the (k,f) plane is that events with downdip to the right are considered positive and are mapped to the right quadrant in the (k,f) plane, while events with downdip to the left are considered negative and map to the left quadrant (Yilmaz, 1987). Dipping events in (x,t) space map as radial lines passing

through the origin in the (k,f) domain, with steeper dipping events mapping closer to the horizontal wavenumber axis. Events with zero dip map to the frequency axis ($k_x = 0$) (Yilmaz, 1987).

Spatial aliasing of migrated data occurs when the time difference between the arrival of a wavefront at two adjacent receivers is greater than, or equal to, half the dominant period of the wavefront (Sheriff, 1984; Yilmaz, 1987). Spatially aliased frequency components will be migrated in the wrong direction, generating dispersive noise and degrading the quality of the resultant section (Sheriff and Geldart, 1983; Yilmaz, 1987).

The threshold frequency for the zero-offset case (CMP gathered data), above which spatial aliasing occurs, is given by:

$$f_{max} = \frac{v}{4\Delta x \sin\theta} \tag{5.2}$$

where v is the medium velocity, Δx is the CMP trace interval, and θ is the structural dip angle (Yilmaz, 1987). In general, the steeper the structural dip and the coarser the CMP trace interval, the lower the frequency at which spatial aliasing occurs (Yilmaz, 1987).

5.3.2 *F-K (STOLT) MIGRATION*

A derivation of the constant velocity F-K migration equation is presented in Appendix F

Given the upcoming seismic wave field P(x,z=0,t) recorded at the surface, migration attempts to reconstruct the reflectivity function P(x,z,t=0). The wave field is extrapolated down to depth z (the reflector in depth), and the diffracted energy is migrated back to the point of emanation (Stolt, 1978). This is equivalent to invoking the imaging principle. The imaging principle

assumes that the spatial position and shape of the wavefront emanating from an exploding reflector at t = 0, corresponds to the true spatial position and shape of the reflector (Claerbout and Doherty, 1972).

To utilize the separability of monochromatic linear dipping events in F-K space, a 2-D Fourier transform over x and t is applied to obtain $P(k_x,0,\omega)$.

The non-migrated seismic data is then represented in the F-K domain by the expression

$$P(x,z,t) = \int\int P(k_x,0,\omega)e^{i\left(\omega t - k_x x + \sqrt{\frac{\omega^2}{v^2}-k_x^2}z\right)}\, dk_x d\omega \qquad (5.3)$$

For a constant velocity model, the change of variables from ω to k_z is effected using the relationships (Stolt, 1978)

$$k_x^2 + k_z^2 = \frac{\omega^2}{v^2} \qquad (5.4)$$

and

$$\frac{d\omega}{dk_z} = \frac{vk_z}{\sqrt{k_x^2+k_z^2}} \qquad (5.5)$$

Substitution of the above two relations into equation (5.3) results in the constant velocity F-K migration equation (Stolt, 1978):

$$P(x,z,0) = \int\int P(k_x,0,\omega[k_x,k_z])e^{i(k_z z - k_x x)}\frac{vk_z}{\sqrt{k_x^2+k_z^2}}\, dk_x dk_z \qquad (5.6)$$

During the migration procedure, each event in the (x,t) domain is rotated about the projected intersection with the surface (Fig. 5.3) (Yilmaz, 1987). The

horizontal spatial frequency is not altered by migration. This implies that k_x does not change (Chun and Jacewitz, 1981). In the (k,f) domain, during migration each element of a dipping reflector is rotated about the projected intersection with the vertical wavenumber axis (Fig. 5.4) (Yilmaz, 1987). The intersection of the rotation and the line k_x = constant is the true spatial position of the element. Elements of both diffraction hyperbolae and dipping events are treated identically under migration.

Stolt stretch

While the Stolt method is formulated for a medium of constant velocity, the method may be extended to account approximately for velocity variations by applying a time stretch to the section (Stolt, 1978) as shown in Appendix G. As noted in Stolt (1978), the applied stretch modifies the input wave field so that the wave field appears to be the response to a constant velocity earth. After application of the Stolt constant velocity F-K migration algorithm (Stolt, 1978), and inverse double Fourier transformation of the migrated data in stretched coordinates, the time stretch is removed.

Use of the Stolt stretch factor produces acceptable results provided the velocity variations are within limits of time migration (Yilmaz, 1987). This implies that the velocity variations are sufficiently gradual, so that the diffraction hyperbolae are not excessively distorted. Violation of this assumption would result in the diffraction energy not migrating consistently to the diffraction apex.

Despite the constant velocity limitation inherent in the Stolt method, it has a useful application in that the algorithm is computationally fast in comparison to phase migration (Hosken and Deregowski, 1985; Yilmaz, 1987). The efficiency of the Stolt method is a result of the direct mapping of ω to k_z as shown in equations (5.4) and (5.5), for a constant migration velocity (Yilmaz, 1987).

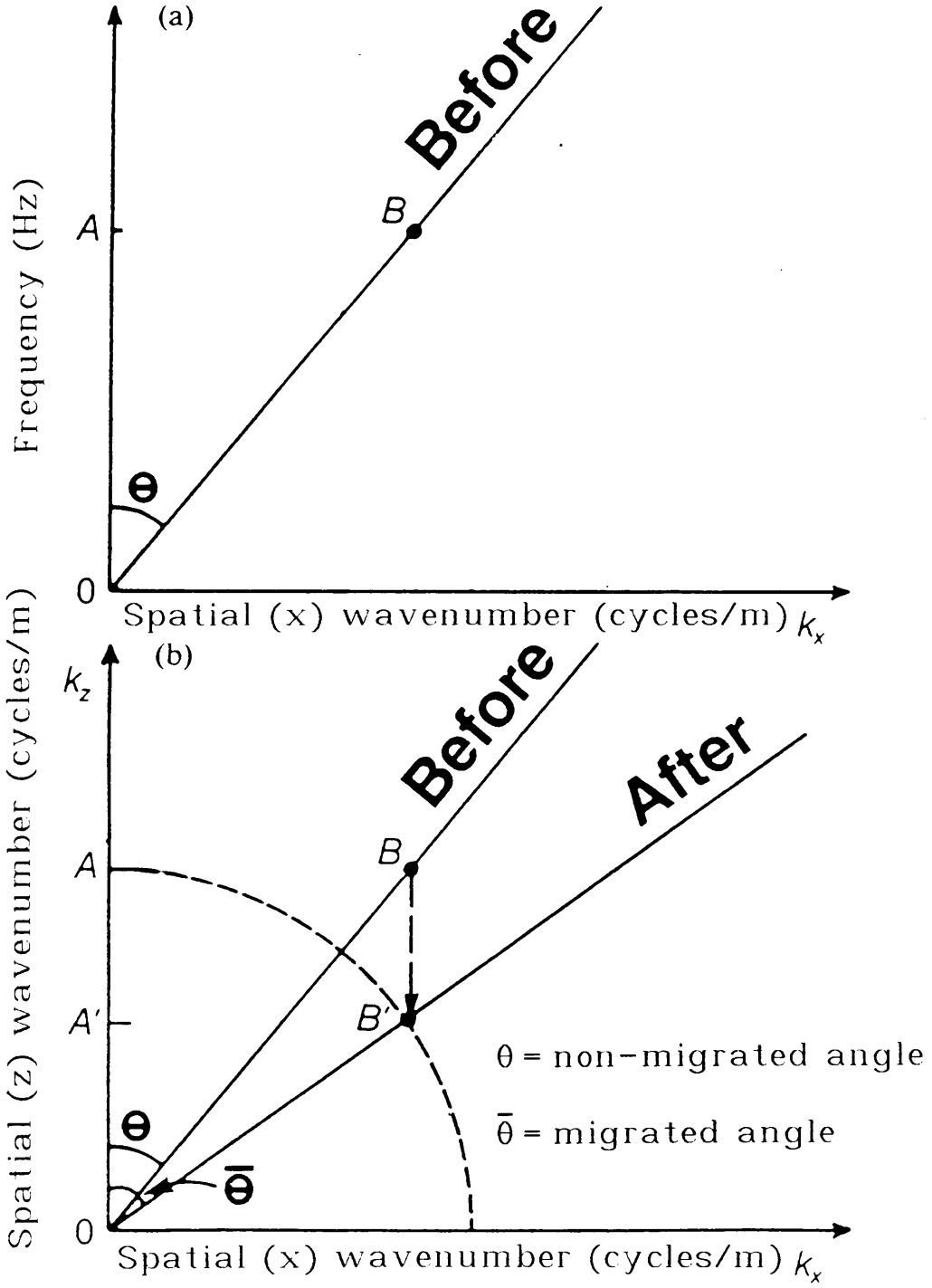

Fig. 5.4 Schematic representation of migration principles in the F-K domain (adapted from Chun and Jacewitz, 1981).

Because of the computational efficiency, the Stolt method was used in the evaluation of the optimum migration velocity function for phase-shift migration.

5.3.3 *PHASE-SHIFT METHOD*

Phase-shift migration (Gazdag, 1978) transforms the surface-recorded, upgoing seismic wavefield $P(x,z=0,t)$ into the wavefield $P(x,z,t=0)$ by repeatedly applying a $k_z\Delta z$ phase-shift to the recorded wavefield.

A 2-D Fourier transform over x and t is applied to the CMP stacked data to obtain $P(k_x,0,\omega)$. Downward continuation of the surface data to a depth Δz is achieved by applying to the 2-D Fourier transformed data the phase-shift term

$$e^{ik_z\Delta z} \tag{5.7}$$

In the ω-k_x domain, the dispersion relationship between k_z, ω, and k_x is invoked, resulting in the downward extrapolation operator

$$e^{-i\sqrt{\frac{\omega^2}{v^2}-k_x^2}\,\Delta z} \tag{5.8}$$

Given an input time signal with constant time-sampling interval, the operator is converted to the single time unit downward extrapolation operator by substituting $\Delta z = v\Delta\tau$, where $\Delta\tau$ is the sample time-interval. Equation (16) becomes

$$e^{-iv\sqrt{\frac{\omega^2}{v^2}-k_x^2}\,\Delta\tau} \tag{5.9}$$

The single time unit downward extrapolation operator is continuously applied to the input data in the FK domain. At each application of the phase-shift operator to the monochromatic wave, the imaging condition ($t = 0$) is met by

summation over all frequency components of the 2-D Fourier transformed data (Yilmaz, 1987). In this manner, each component of the wavefield recorded at the surface is extrapolated down to a depth z by application of the phase-shift operator (equation 5.9). A two-dimensional inverse Fourier transform from the ω-k_x domain to the t-x domain, at t = 0, yields the migrated seismic section.

The phase-shift method is an F-K migration method which is suitable for the migration of seismic data containing a temporally varying velocity function and steeply dipping events (Gazdag, 1978). The phase-shift method allows vertical variations in velocity and is accurate for dips of up to 90°. Dip filtering may be achieved by limiting the width of the migration aperture. Summation over all frequency components of the 2-D Fourier transformed data for each depth step, however, makes the phase-shift method computationally more expensive than the Stolt method (Yilmaz, 1987).

5.3.4 *MIGRATION EVALUATION*

Parameters evaluated in the Stolt F-K migration method included:

1. the number of traces and trace overlap of the individual migration panels; and
2. migration velocities.

In order to test the effect of varying panel widths and overlap, widths of 100, 200, and 512 traces, with corresponding overlaps of half the panel width, were used. A constant migration velocity of 4500 m/s was used.

The results indicated that the small panels do not contain sufficient lateral representation from the diffracting events to adequately reconstruct the migrated event. Migration with a panel width of 512 traces provided maximum trace-to-trace coherency and improved resolution.

The results of the panel testing are displayed in Figure 5.5. The width of the panels had a direct influence on the migration aperture. The migration aperture is related to the number of traces that the diffraction hyperbola spans. The optimum aperture value is defined as twice the maximum horizontal displacement in migration, for the event with the steepest dip (Yilmaz, 1987). The horizontal displacements for the events are directly proportional to the square of the velocity (Yilmaz, 1987). The average seismic velocity of the reflectors in the P1-86 survey is approximately 5500-6000 m/s, implying that a large migration aperture would be required. An equivalent explanation is to note that diffractions in high velocity media exhibit less moveout than do diffractions in low velocity media. This implies that the limbs of the diffraction hyperbola spans more CMP's in a high velocity media than in a low velocity media. Thus, in high velocity media, wider migration panels are needed to successfully migrate the diffraction energy to the diffraction apex.

A base velocity function was chosen empirically from the optimum velocity functions determined during velocity analysis. The base function was perturbated to evaluate the sensitivity of the migrated data to variations in migration velocity. The data were migrated using the base function, and the base function less 10% - 80%, in steps of 10% (Table 5.1). The columns labelled "TWT", "BASE", and "FINAL" represent the two-way traveltime, the base velocity function, and the final velocity function, respectively.

TABLE 5.1 F-K migration velocity testing

TWT (s)	BASE (m/s)	-10%	-20%	-30%	-40%	-50%	-60%	-70%	-80%	FINAL
0.4	3500	3150	2800	2450	2100	1750	1400	1050	700	1750
1.0	4000	3600	3200	2800	2400	2000	1600	1200	800	2000
2.0	6000	5400	4800	4200	3600	3000	2400	1800	1200	2400
4.5	10000	9000	8000	7000	6000	5000	4000	3000	2000	4000

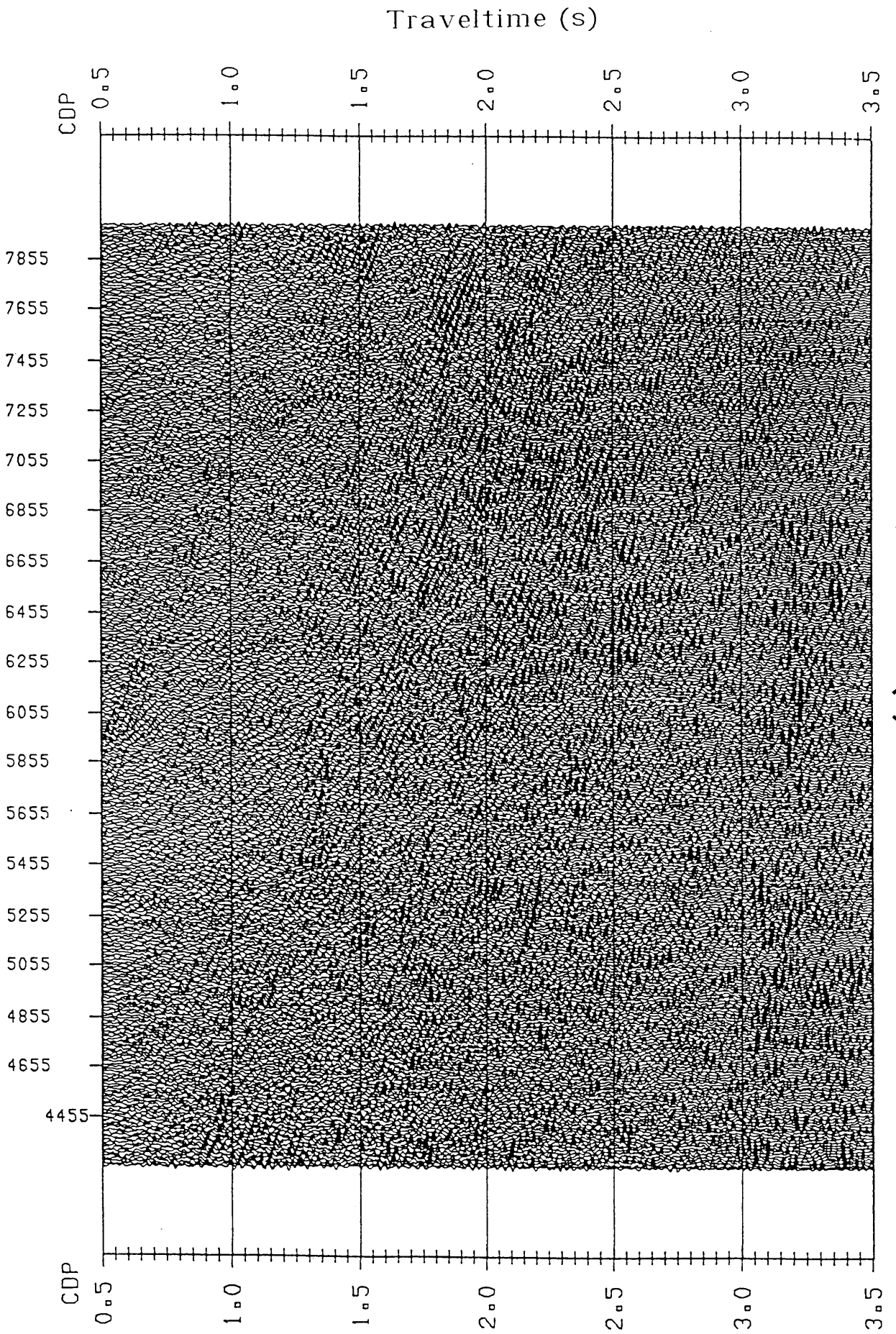

Fig. 5.5a F-K migrated section illustrating the results of the 100 trace migration panel-width test.

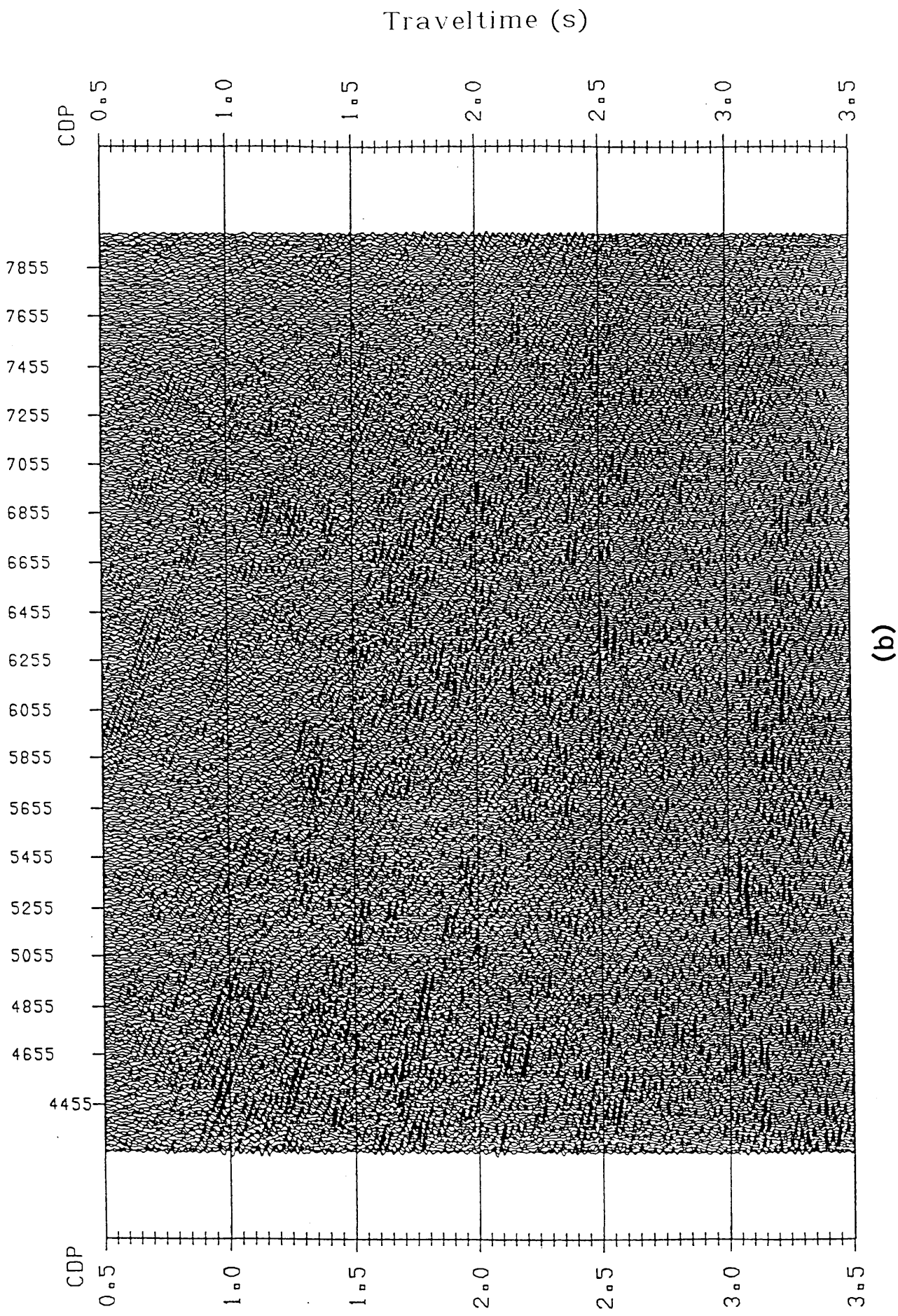

Fig. 5.5b F-K migrated section illustrating the results of the 200 trace migration panel-width test.

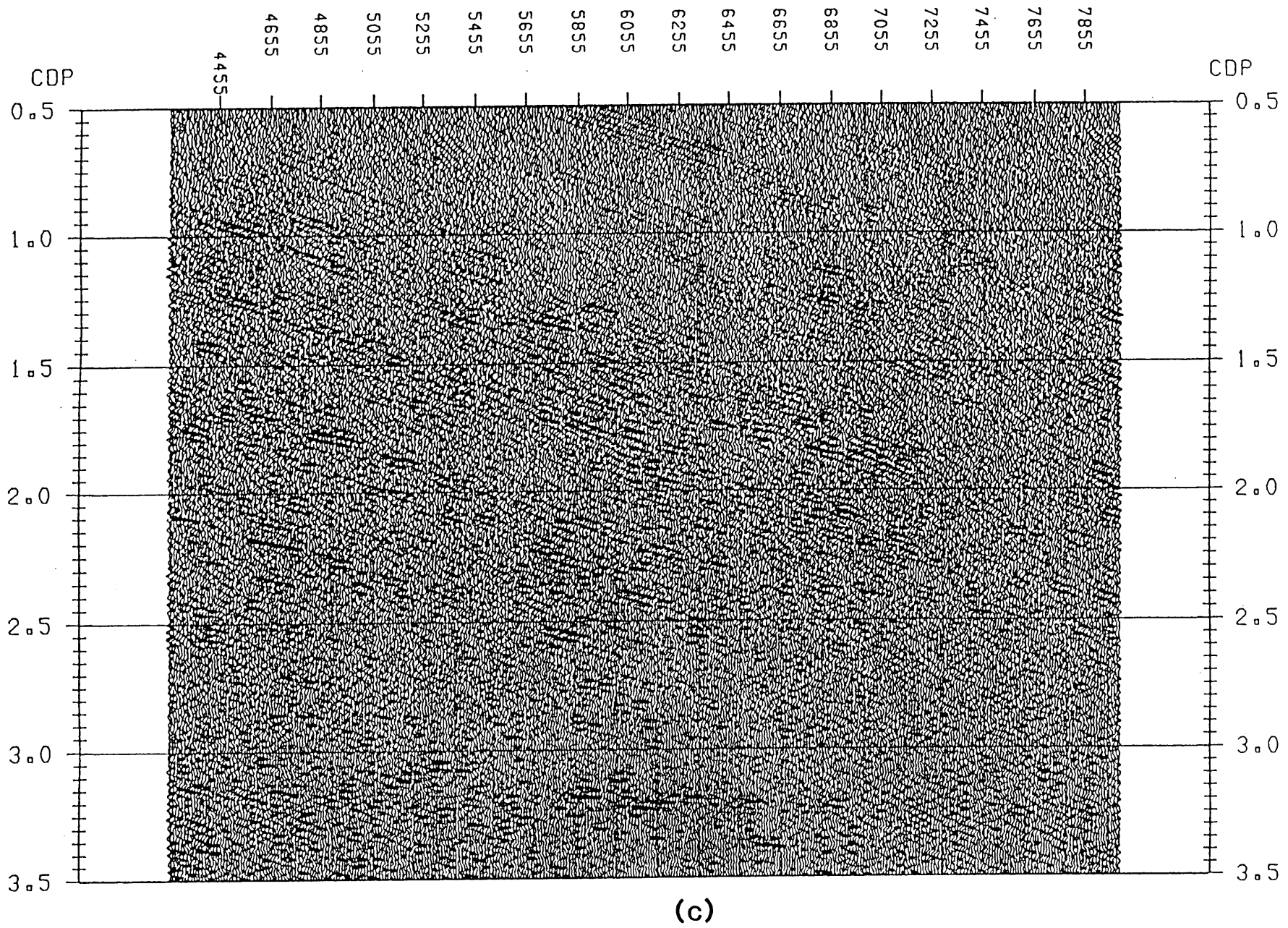

Fig. 5.5c F-K migrated section illustrating the results of the 512 trace migration panel-width test. Migration using the 512 trace panel width appears to provide the greatest coherency and resolution.

Figure 5.6 depicts the results of migration with the base velocity, the base less 70%, and the results of migration with the final velocity function. All events on the section migrated at the base velocity are over migrated. This is indicated by the characteristic "smiles" observed on the migrated section (McQuillin *et al.*, 1984; Yilmaz, 1987). Conversely, the section migrated with base less 70% is under migrated. The final velocity function was determined by interpreting the effect of migration on the data for all test velocities. Using interpretive processing, a final velocity function to be used in the phase-shift migration testing was constructed. The final velocity function used in the phase-shift migration testing is shown in Table 5.1.

The parameter tested for phase migration was the aperture width. Apertures of 15°, 30°,45°,60° and 90° were evaluated. The migration velocity function used was that determined as optimum from results of F-K migration testing. The 15° aperture resulted in under migration and excessive dip-filtering of the data (Fig 5.7). Use of a 30° aperture resulted in significant improvement, however the data are still under migrated. Subtle improvements exist between the 45°, 60°, and 90° cases, with the migration being most effective in the 90° case. As processing time was not a criterion upon which the results were based, it was decided to migrate the data with the 90° aperture.

5.4 F-K DIP FILTER

Events displaying differences in dip (apparent velocity) in the (x,t) plane map to different regions in the (k,f) plane (Fig. 5.8). This property enables the selective filtering of events that are represented by specific dips (Yilmaz, 1987).

Coherent linear noise (ground roll), guided waves and sideswipe energy are generally represented by steeply dipping events in the (x,t) plane (Yilmaz, 1987). The reject zone of the F-K dip filter is designed as an apparent-velocity

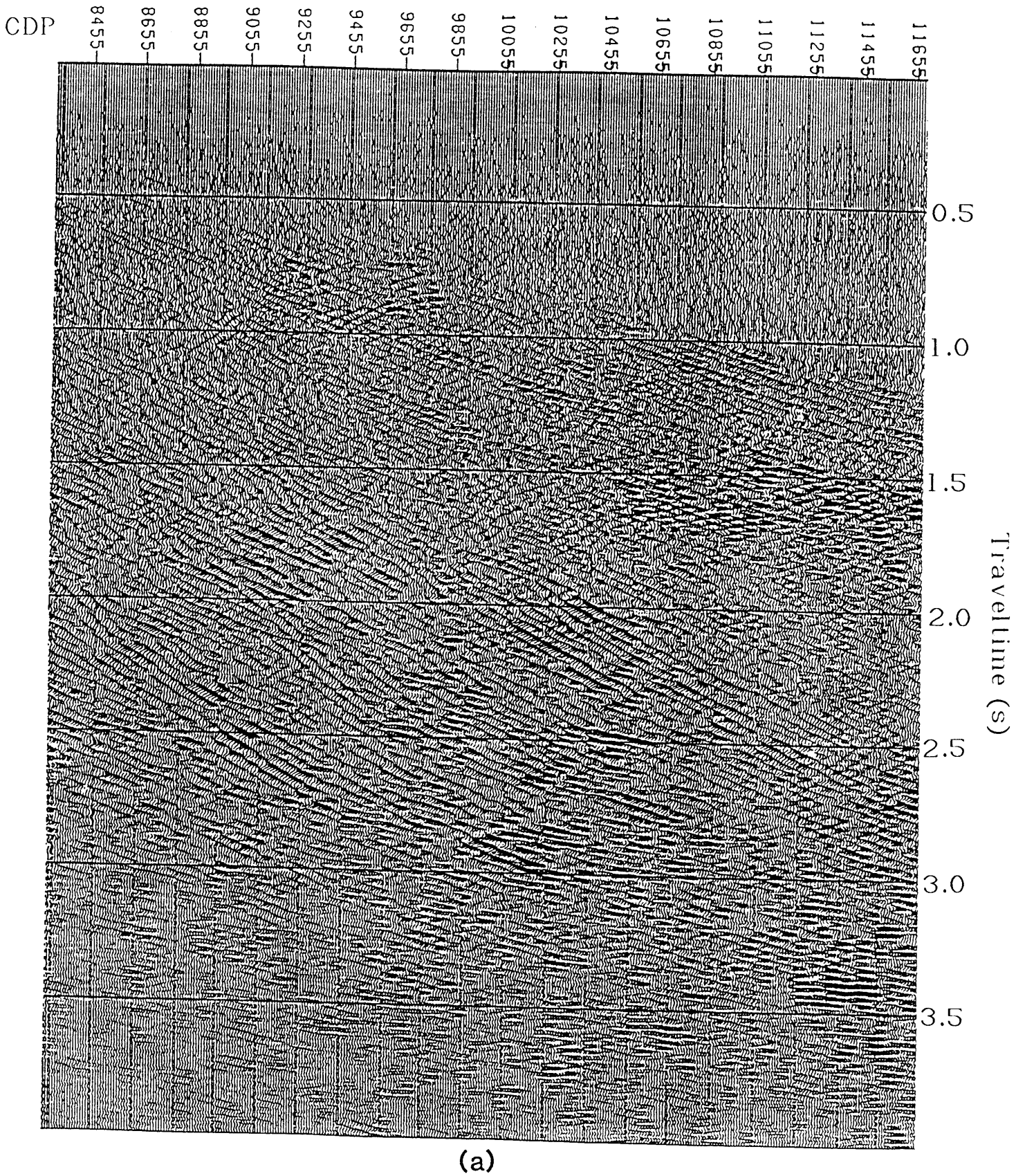

Fig. 5.6a F-K migrated section illustrating the results of migration velocity testing using the base velocity function. All events on the section are overmigrated.

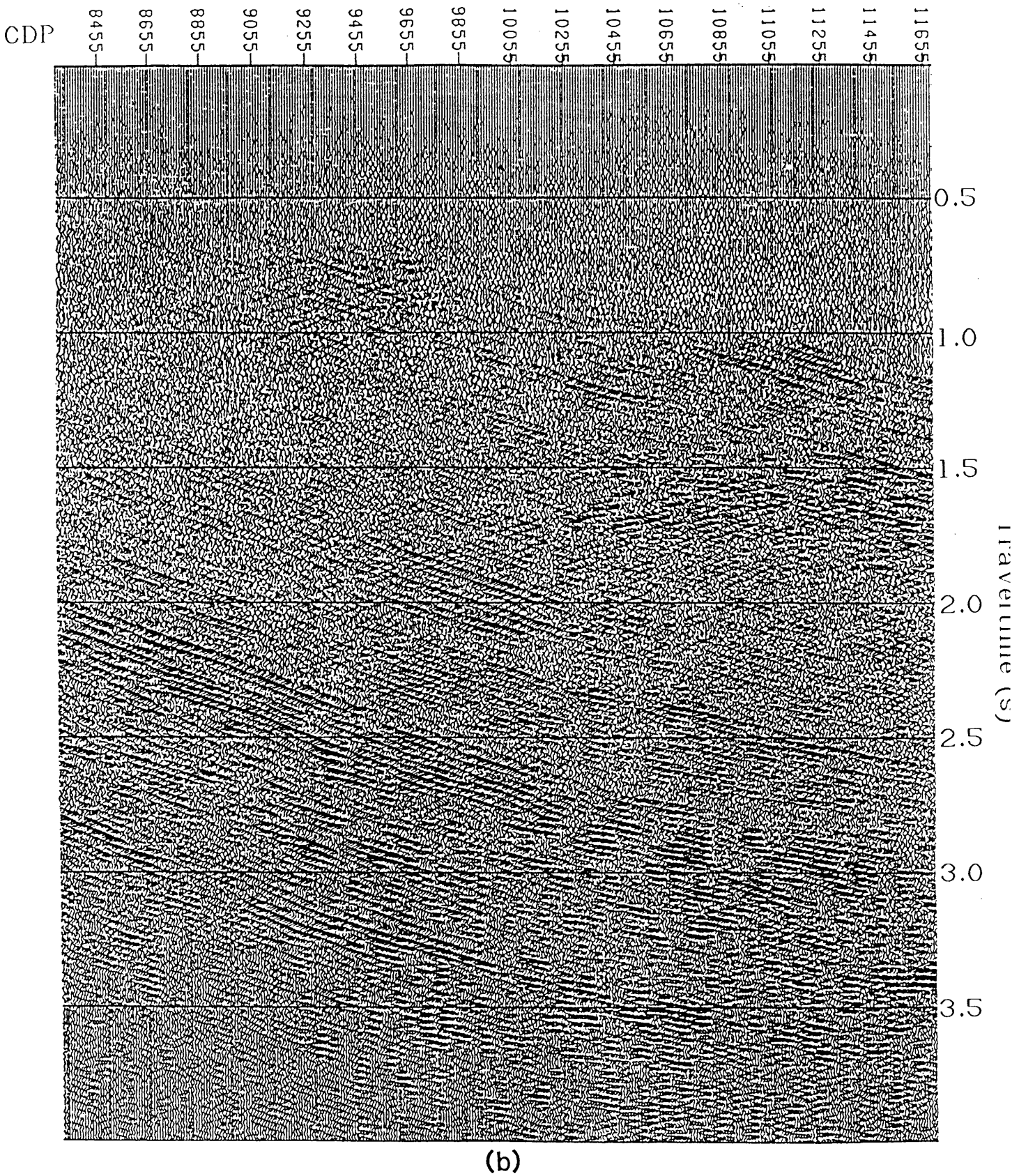

Fig. 5.6b F-K migrated section illustrating the results of migration velocity testing using the base function less 70%.

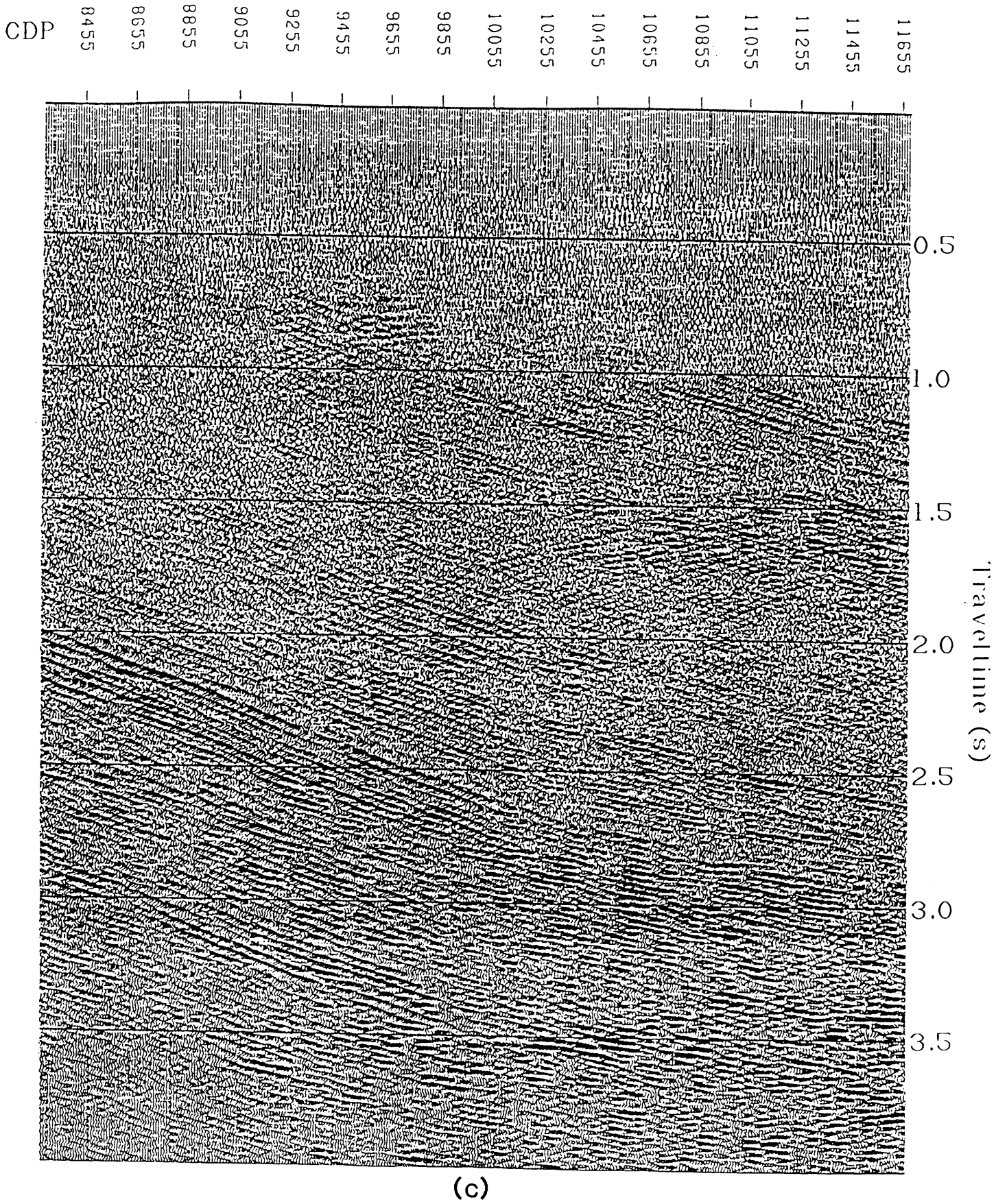

Fig. 5.6c F-K migrated section illustrating the results of migration velocity testing using the final velocity function.

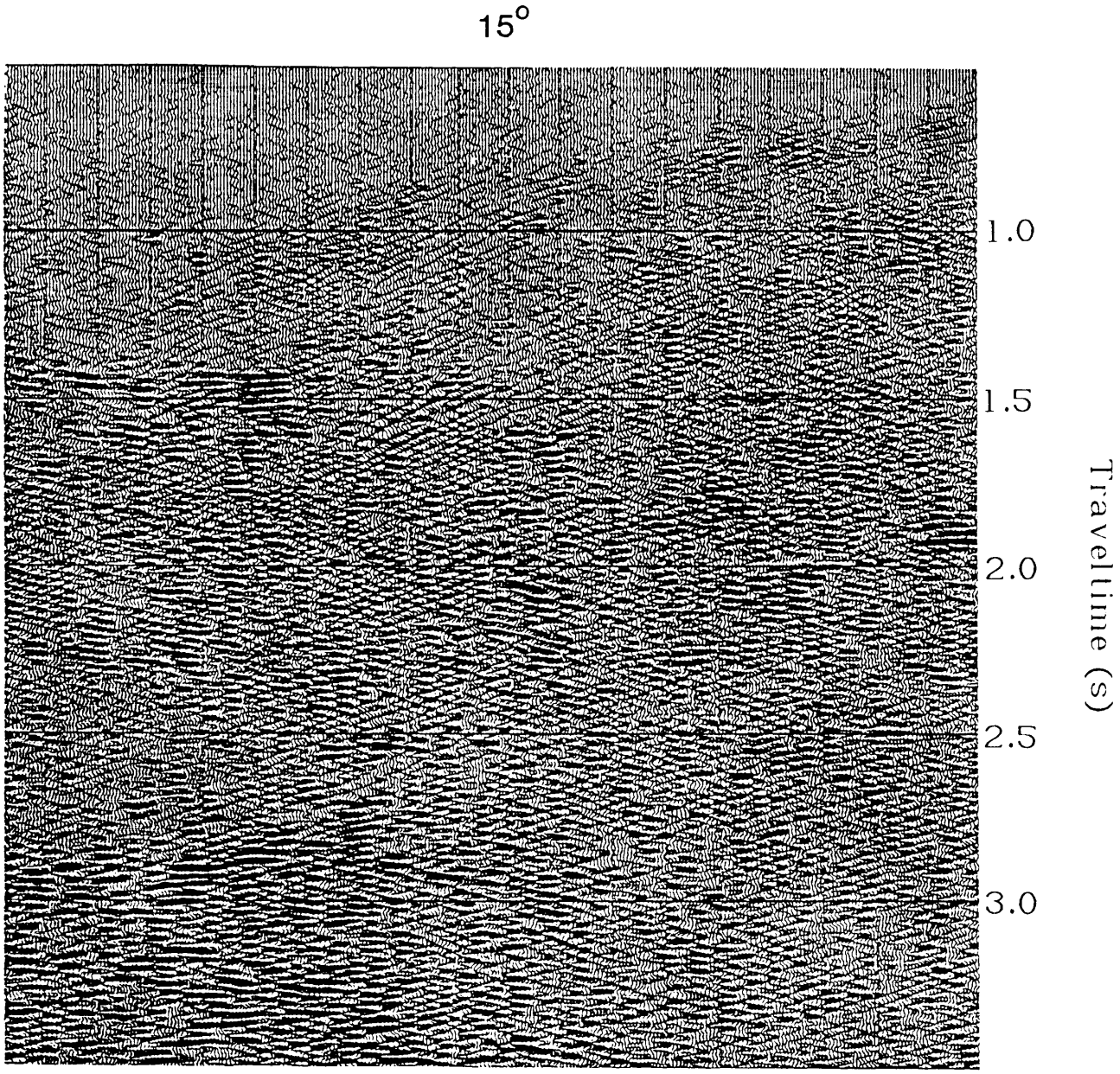

Fig. 5.7a Phase-shift migrated section illustrating the results of aperture testing for a 15° aperture. The data are undermigrated and excessively dip-filtered.

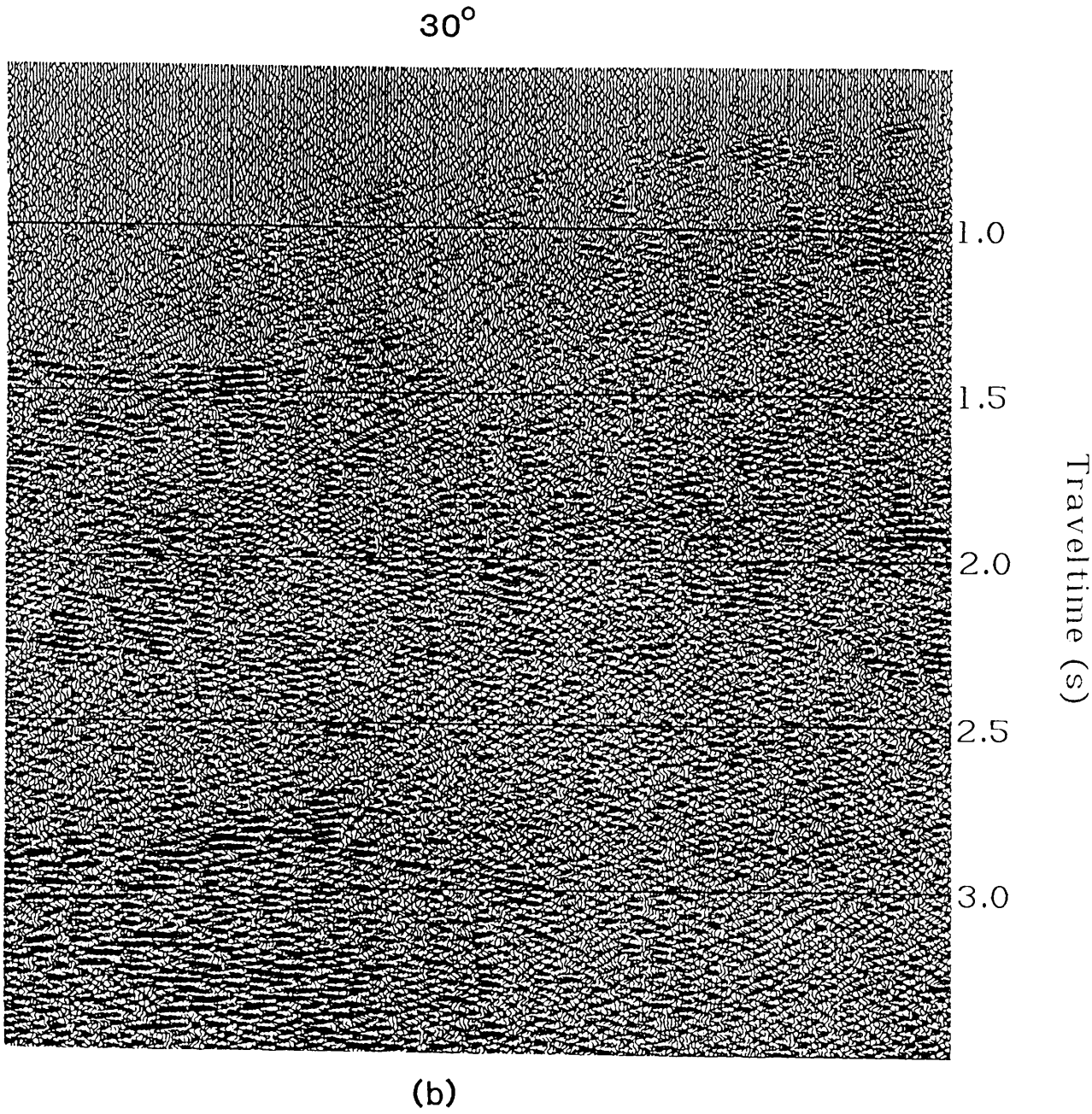

Fig. 5.7b Phase-shift migrated section illustrating the results of aperture testing for a 30° aperture. The data are undermigrated.

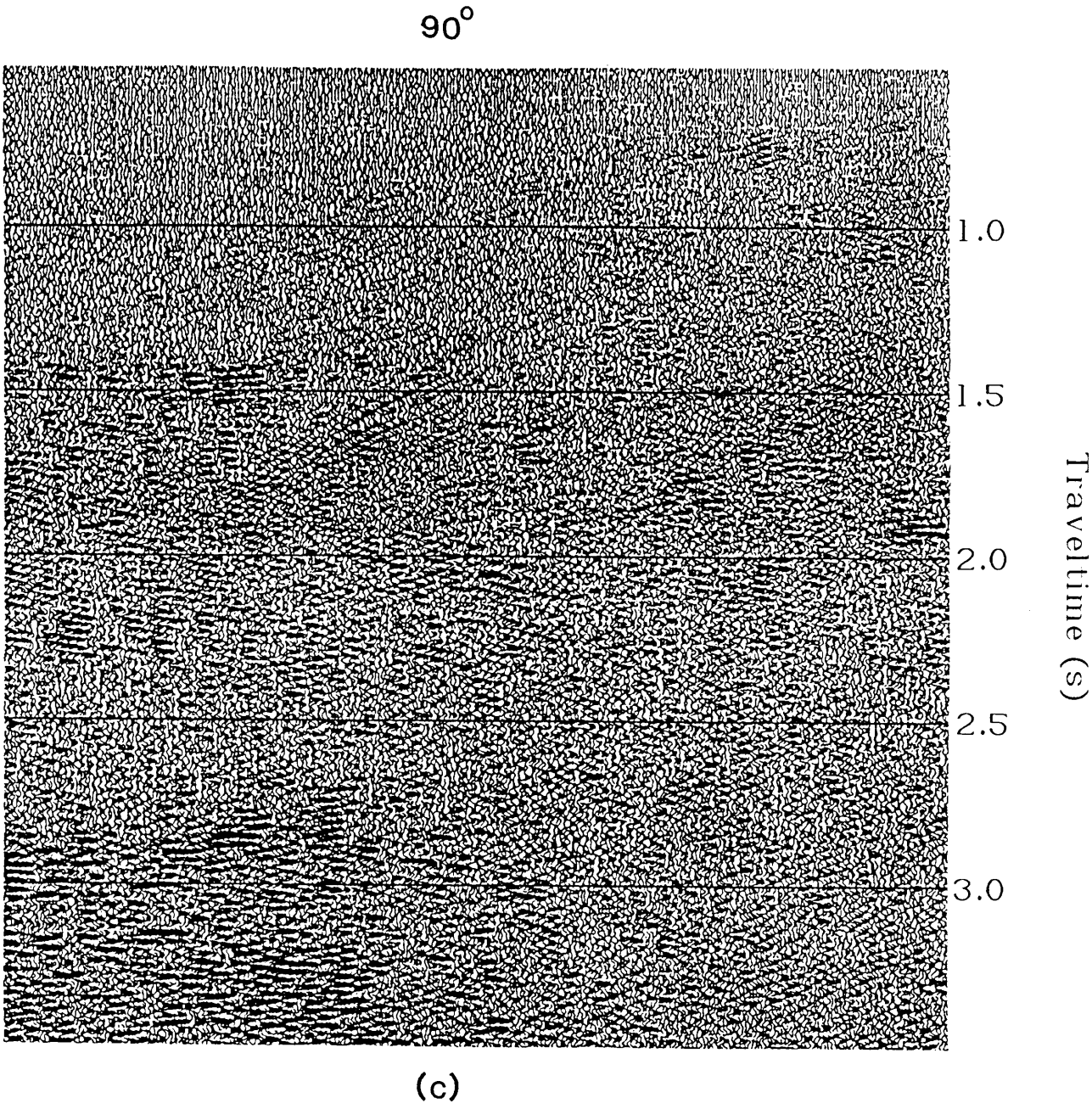

Fig. 5.7c Phase-shift migrated section illustrating the results of aperture testing for a 90° aperture. Migration is most effective for the 90° case.

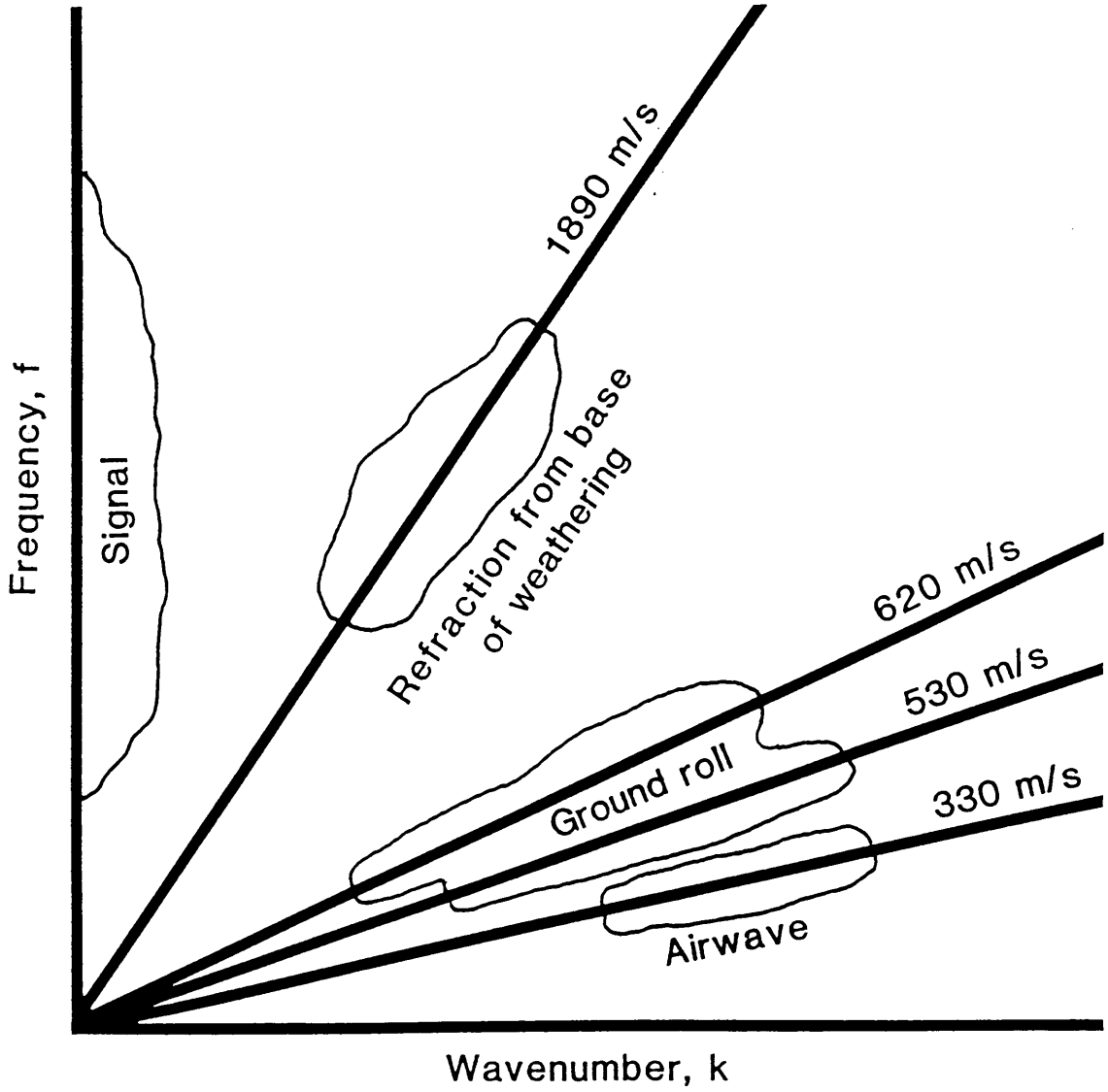

Fig. 5.8 Schematic of an F-K plot illustrating separation of the signal, ground roll modes and airwave in the F-K domain.

window around the undesirable event. Where multiple dip range specification, used to filter events of differing dips, is unavailable, the F-K dip filter may be applied recursively to achieve the same effect (Hatton *et al.*, 1986).

Wraparound noise (Sheriff, 1984; Yilmaz, 1987), resulting from spatial aliasing is avoided by terminating the F-K spectra at the Nyquist wavenumber via application of a low-pass frequency filter. The fan reject/pass zone of the filter must be tapered at the edges to reduce the effects of Gibbs' phenomenon (Hatton *et al.*, 1986; Yilmaz, 1987). The filter taper should be large enough to prevent ringing, without suppressing the signal in the desired pass zone.

In order to avoid spatial aliasing, a bandpass filter with a pass zone of 20-75 Hz was applied to the poststack data. The F-K spectrum of the data set was used to calculate the apparent velocity of the linear noise components. From the F-K spectrum, it was deduced that events having apparent velocities lower than 3500 m/s constituted linear noise. These events were filtered using a tapered fan filter.

CHAPTER 6

INTERPRETATION

The objectives of the survey were to resolve:

1. the total thickness of the Rashoop Granophyre Suite and Lebowa Granite Suite assemblages;
2. the shape and extent of the Rustenburg Layered Suite (RLS);
3. the structural relationship between the RLS and the Transvaal Sequence; and
4. the shape of the Transvaal basin along the seismic traverse.

In this chapter these issues will be addressed through an interpretation of the final CMP stacked section and the migrated stacked section. Interpretation of the data proceeded by comparing both the pre- and post-migration data in order to identify processing artifacts, as opposed to reliable seismic events (Hosken and Deregowski, 1985). The procedure of simultaneously interpreting both the migrated and non-migrated data provided the optimum interpretation of the seismic sections.

6.1 SEISMIC CORRELATION TO SURFACE GEOLOGY

Interpretation began by correlating the dipping seismic events on the southern end of the seismic section (Fig. 6.1) to the mapped surface geology (Fig. 2.2). The contact between the Transvaal Sequence rocks and the overlying norites of the RLS was interpreted to correspond to the northerly dipping event boundary (marker A; Fig 6.1b), defined by a marked change in character of the seismic signal. The package of events correlated to the Transvaal Sequence is characterized by high amplitude, low frequency seismic signal, while the package interpreted as the norites is represented by lower amplitude events of higher frequency.

The norites were distinguished from the overlying gabbros of the main zone of the RLS by a denser distribution of reflecting markers. The interpreted contact between the norite and the gabbro (marker B; Fig. 6.1b) was correlated to the surface geology.

The seismic signatures of the main zone gabbros and upper zone ferrogabbros are very similar. Both are characterized by relatively low amplitude, high frequency events. The contact between the gabbros and the overlying ferrogabbros (marker C; Fig. 6.1b) was inferred from the surface geology.

The interpreted contact between the ferrogabbro and the Rashoop Granophyre Suite (marker D; Fig. 6.1b) was correlated with the mapped surface geology with a high degree of confidence. There is a distinct difference between the seismic signature of the upper zone ferrogabbros and the overlying Rashoop Granophyre Suite. The seismic response of the Rashoop Granophyre Suite is characterized by an amorphous signature displaying no coherent events.

6.2 NOISE AND SIGNAL QUALITY

The noise occurring after 2,9 s between CMP's 10055 and 12655 is interpreted to originate outside of the plane of the survey. This phenomenon may be due to a change in the direction of the survey line from the true down-dip direction. This may also be partly responsible for the apparent reduction in dip of the layered events in this region.

The region north of CMP 13055 is characterized by a low signal-to-noise ratio. This poor signal quality may be related to:

1. imaging of out-of-plane reflections due to the survey direction change.
2. out-of-plane noise-reflections and noise due to complex 3-dimensional structure.
3. reduced source coupling and high signal attenuation experienced over the less consolidated material of the Karoo Sequence; and

4. signal interference (Ohlovich, 1964) as a result of imaging complex folding/faulting within the plane of the survey.

6.3 STRUCTURAL INTERPRETATION

The high amplitude event starting at approximately 0,1 s at the southern end of the line (event 1; Fig 6.1a) is interpreted as representing the 85 m thick diabase sill which outcrops approximately 1 000 m south of the starting point of the survey (Fig 2.2), in the Silverton Shale Formation.

It proved difficult to relate the surface expression of the Hekpoort Andesite Formation to any seismic event in the Transvaal Sequence reflection package as it does not appear to have a distinct seismic signature associated with either the upper or lower contacts with the host rock. The Hekpoort Andesite Formation lies on tilloids and quartzite of the Boshoek Formation. Such a contact may not be conducive to high amplitude or coherent reflection signal (Stone, 1977). The upper contact of the Hekpoort Andesites is with the Strubenkop Shale Formation. The contact may possibly be characterized by tuffaceous or pyroclastic rocks as observed in areas to the west of the survey (Eriksson and Twist, 1986). Such a contact would result in a weak and incoherent reflection signal.

North of CMP 20855, a package of high amplitude reflectors is observed (event 2; Fig. 6.1c). The high amplitude signature of the events (relative to the adjacent zone of low signal-to-noise ratio) may be attributed to an increase in nominal fold coverage from 24 to 48. The improved signal-to-noise ratio is a result of halving the shot spacing during roll-off.

The package of events between 1,75 s and 4,25 s correlates with the ferrogabbro, gabbro and Transvaal Sequence packages interpreted in the southern portion of the line. The sequence of seismic events is interpreted to be an extension of the dipping events observed in the southern portion of the survey. By correlating the signatures of the aforementioned dipping layers with the

seismic signal occurring between CMP's 12055 and 20855, laterally discontinuous packages corresponding to the Transvaal Sequence, gabbro and ferrogabbro were interpreted. The criteria for interpretation of this region was that a correlation be found for both the low and high frequency events, representing the Transvaal Sequence and RLS respectively. This enabled an interpretation of this region, despite the low signal-to-noise ratio of the non-migrated and migrated data.

While the thickness of the alternating shales and quartzites of the Transvaal Sequence appears to remain approximately constant across the section, there is some uncertainty regarding the structure of the RLS to the north.

One possibility is that the main zone and norite packages remain approximately constant across the section, while the package of events interpreted as the upper zone of the RLS tapers towards the north.

A second possibility is that the marginal norite pinches out over an interpreted anticlinal structure occurring north of CMP 12455, while the main zone tapers drastically. The anticlinal structure may be associated with faulting, occurring in the tensional regime of the fold.

Pinching out and tapering of units in the Bushveld Complex is documented in Schwellnus (1962) and lateral discontinuity of the norite is evident in the region of Brits, west of the survey (Roberts, 1981). Conversely, many regions of the Bushveld Complex (including the Bethal area and the region north of Potgietersrus) are characterized by a wide lateral distribution of the upper zone (Von Gruenewaldt, 1979)

High amplitude, laterally discontinuous reflectors observed above the upper zone of the RLS (event 3; Fig 6.1c) may be related to the presence of felsite of the Rooiberg Group at the granite/RLS contact, to the presence of large

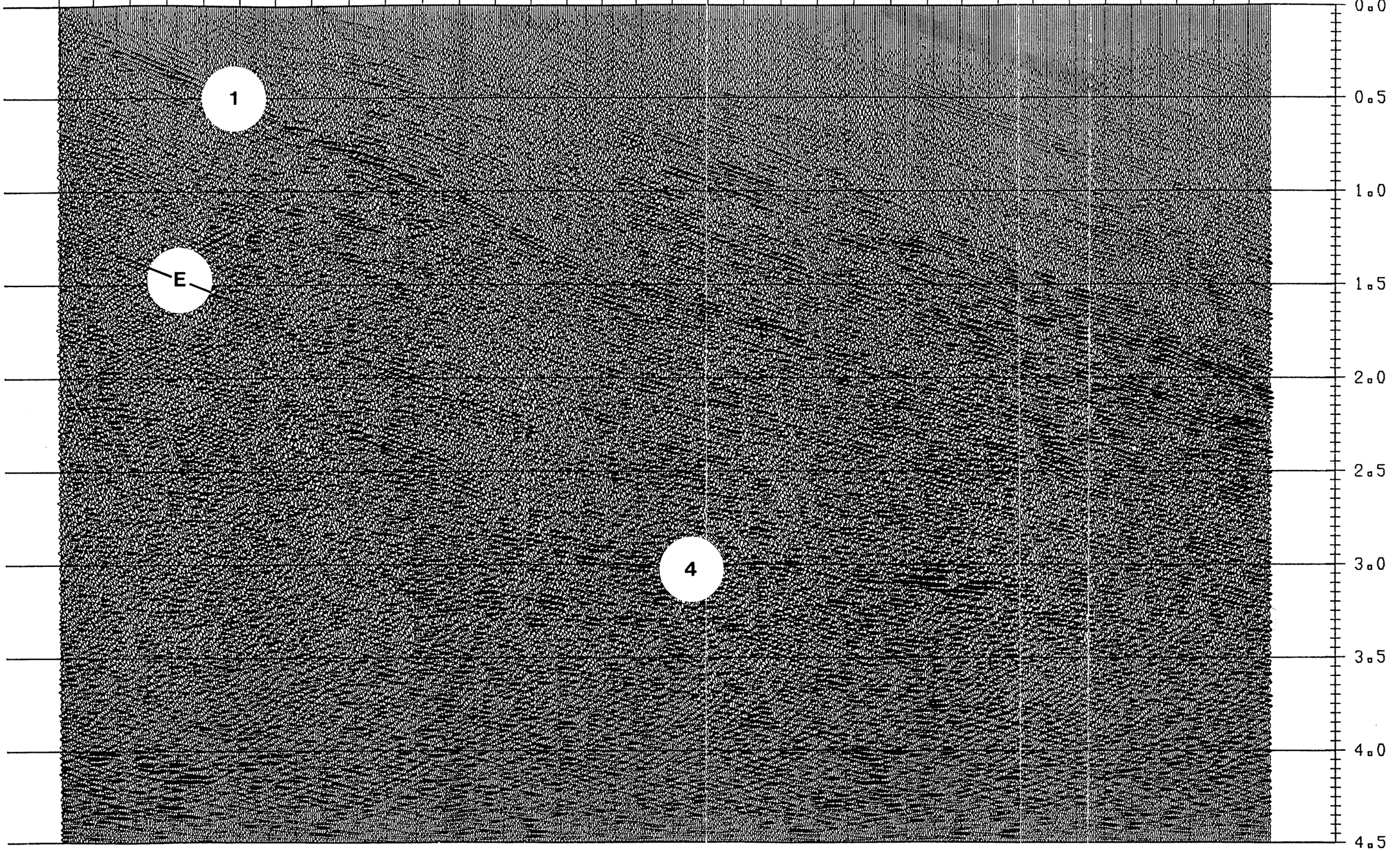

Fig. 6.1a Final migrated section showing the interpreted geophysical events (section A-B on Fig. 2.2).

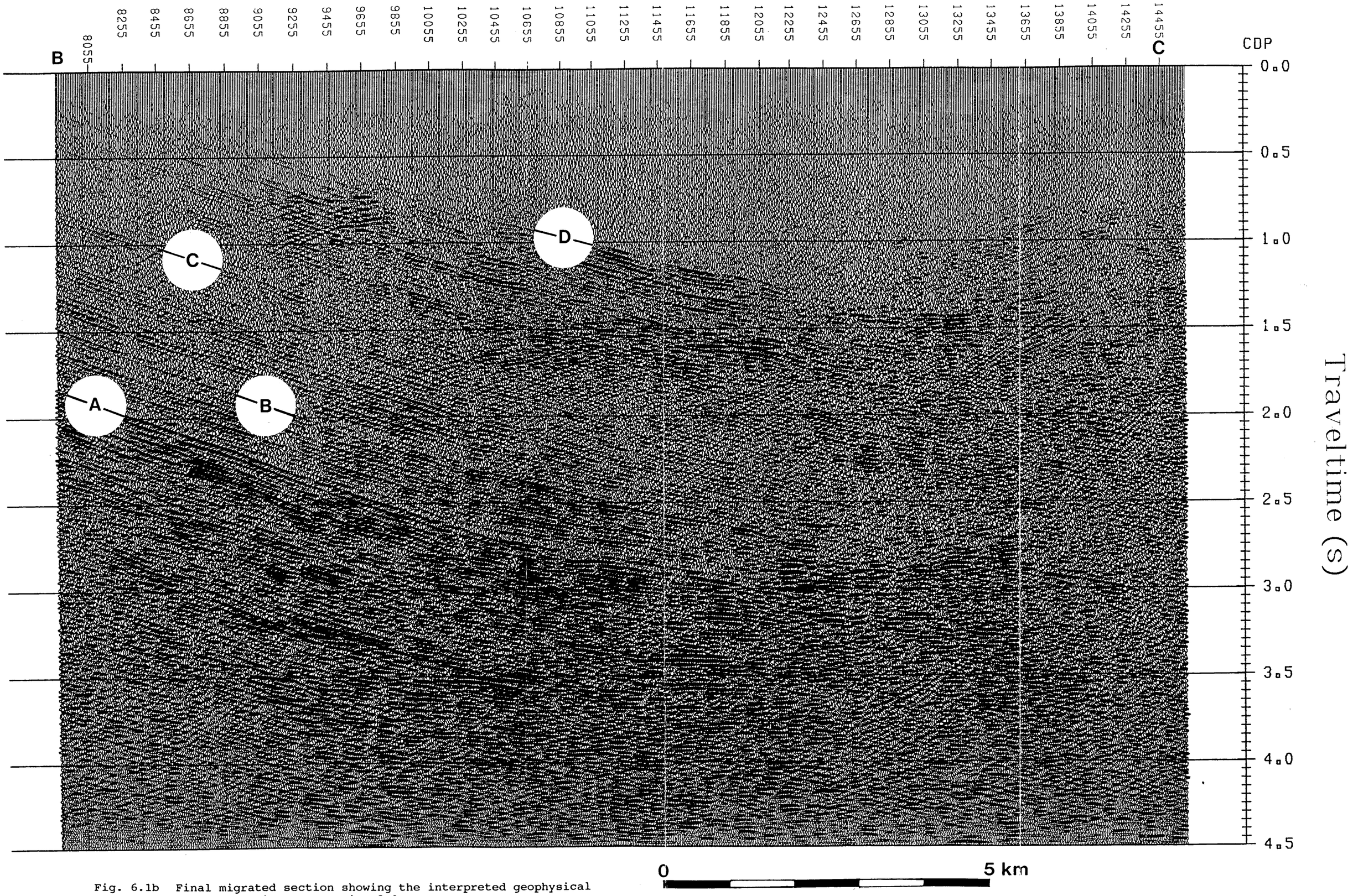

Fig. 6.1b Final migrated section showing the interpreted geophysical events (section B-C on Fig. 2.2).

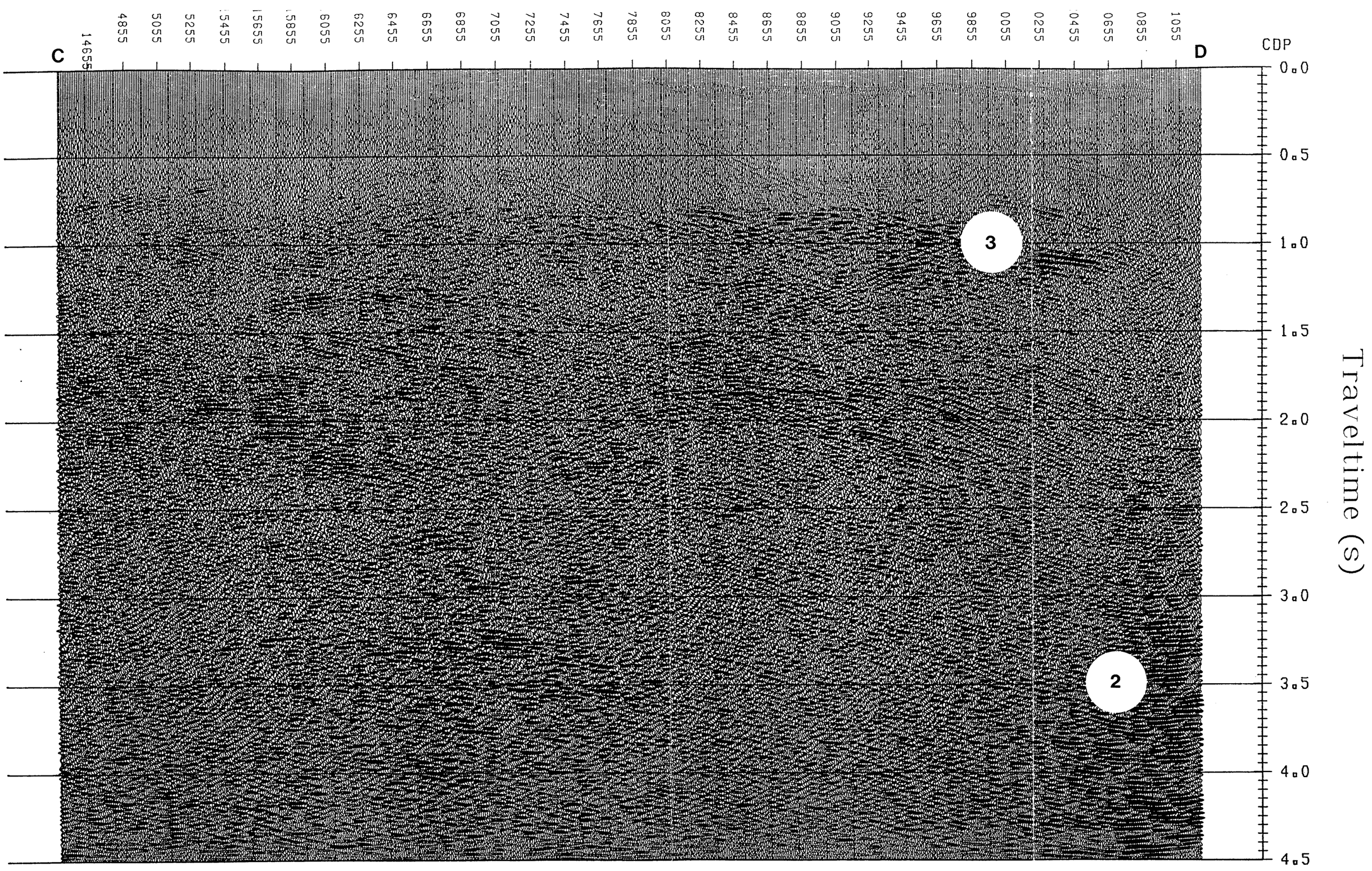

Fig. 6.1c Final migrated section showing the interpreted geophysical events (section C-D on Fig. 2.2).

quartzite xenoliths, or to the development of extensive mafic pegmatites. The development and distribution of mafic pegmatites in the RLS has been shown to be strongly controlled by floor folds (Reichhardt, 1989; Viljoen and Scoon, 1985).

6.4 PROPOSED STRUCTURAL MODEL

Although time-to-depth conversion has not been performed on the stacked section, it is possible to obtain approximate thicknesses of the interpreted units from the time section, using a replacement velocity of 5000-6000 m/s.

The shales and quartzites of the Transvaal Sequence, including the Hekpoort Andesite Formation, are interpreted to be approximately 4,25-5,1 km (1,7 s TWT) thick. This however tapers to approximately 3,75-4,5 km (1,5 s TWT) by CMP 5855. The interpretation implies that the Timeball Hill Formation of the Transvaal Sequence pinches out against the underlying Chuniespoort Group (marker E; Fig. 6.1a) in this region. This interpretation is supported by the presence of an unconformity (event 4; Fig. 6.1a) which may indicate partial to complete pinching out of the Chuniespoort Group by CMP 7055.

In the south, the marginal norite of the RLS is interpreted to be approximately 0,75-0,9 km (0,3 s TWT) thick, while the main zone gabbros are interpreted to be approximately 1,75-2,1 km (0,7 s TWT) thick. The upper zone ferrogabbros are interpreted to be approximately 1,8-2,2 km (0,75 s TWT) thick.

Two-dimensional forward modeling (Talwani *et al.*, 1959) was performed on regional gravity data (Fig. 6.2) relating to the area imaged by the seismic survey. The thickness of the Transvaal Sequence and combined norite/gabbro package was obtained from the interpreted seismic section. The density

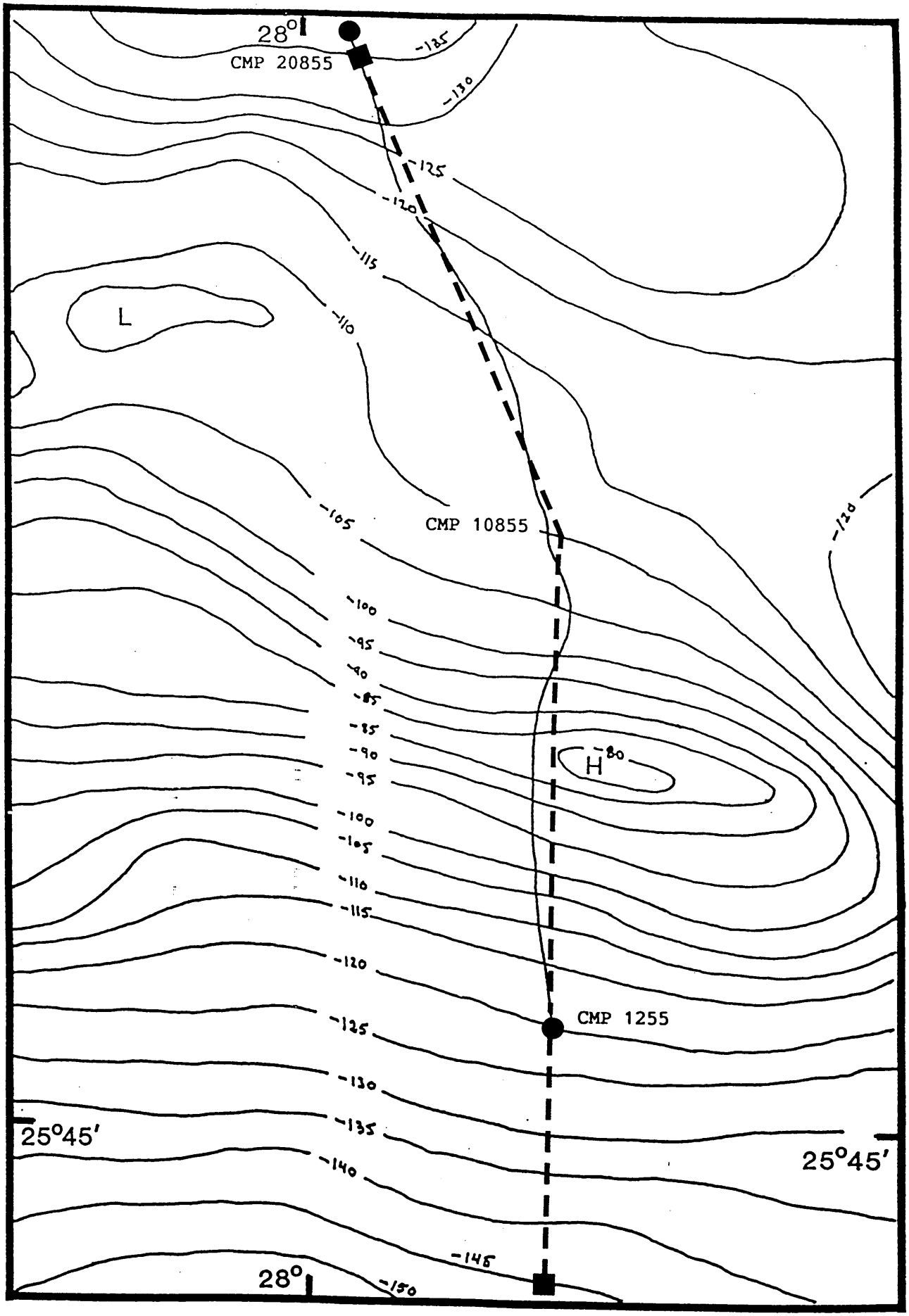

Fig 6.2 Bouguer gravity contour map of the region covered by Fig. 2.2 (after Harvey, 1981). The solid line terminated by circles represents the seismic survey route. The gravity profile is represented by the dashed line terminated by squares. Approximate CMP numbers are shown for the intersection of the gravity profile and the start of the seismic survey, the bend in the gravity profile, and the end of the gravity profile.

contrasts, relative to the basement rocks (average density 2,67g/cm^3), used in the gravity modeling were derived from values quoted by Smit and Maree (1966). A constant regional gravity field of -150 mgal was subtracted from the gravity data. The interpolated station interval used in the modeling is 2 500 m.

Preliminary gravity modeling of the postulated seismic models (the tapering upper zone model and the tapering main zone model) confirmed that it is possible to model the Transvaal Sequence, plus components of the RLS, as occurring to north of the Mabopane fault proposed by Du Plessis and Levitt (1987) (Fig. 6.3 and Fig. 6.4). In each of the gravity models, the dolomites of the Chuniespoort Group are not included in the Transvaal Sequence body, the implication being that the dolomites are of constant thickness across the gravity model. The sills occurring within the shales and quartzites of the Transvaal Sequence are included in the Transvaal Sequence body for the purposes of modeling the gravity data.

Geological studies of the Bushveld Complex (Schwellnus, 1962; Button, 1978; Molyneux and Klinkert, 1978; Roberts, 1981) suggest that the tapering main zone model is the more realistic of the two proposed models (Von Gruenewaldt, *pers. comm.*). In the postulated models the mass excess to the north of the survey area is proposed to be a result of the occurrence of the Transvaal Sequence and the occurrence of components of the RLS having significant vertical dimensions. This is in contrast to Kleywegt and Du Plessis (1986), who modeled the mass excess, necessary to successfully match the calculated gravity anomaly values to the observed gravity anomaly values in the north of the survey area, as due to the occurrence of the complete succession of Transvaal Sequence rocks without the intrusive mafic rocks. They were, however, only prepared to extrapolate RLS rocks of significant thickness for a few kilometers north of the northernmost outcrops, but accepted that they could be considerably thicker further north (in depth) due to the gravimetric interchangeability of Transvaal Sequence rocks and RLS rocks.

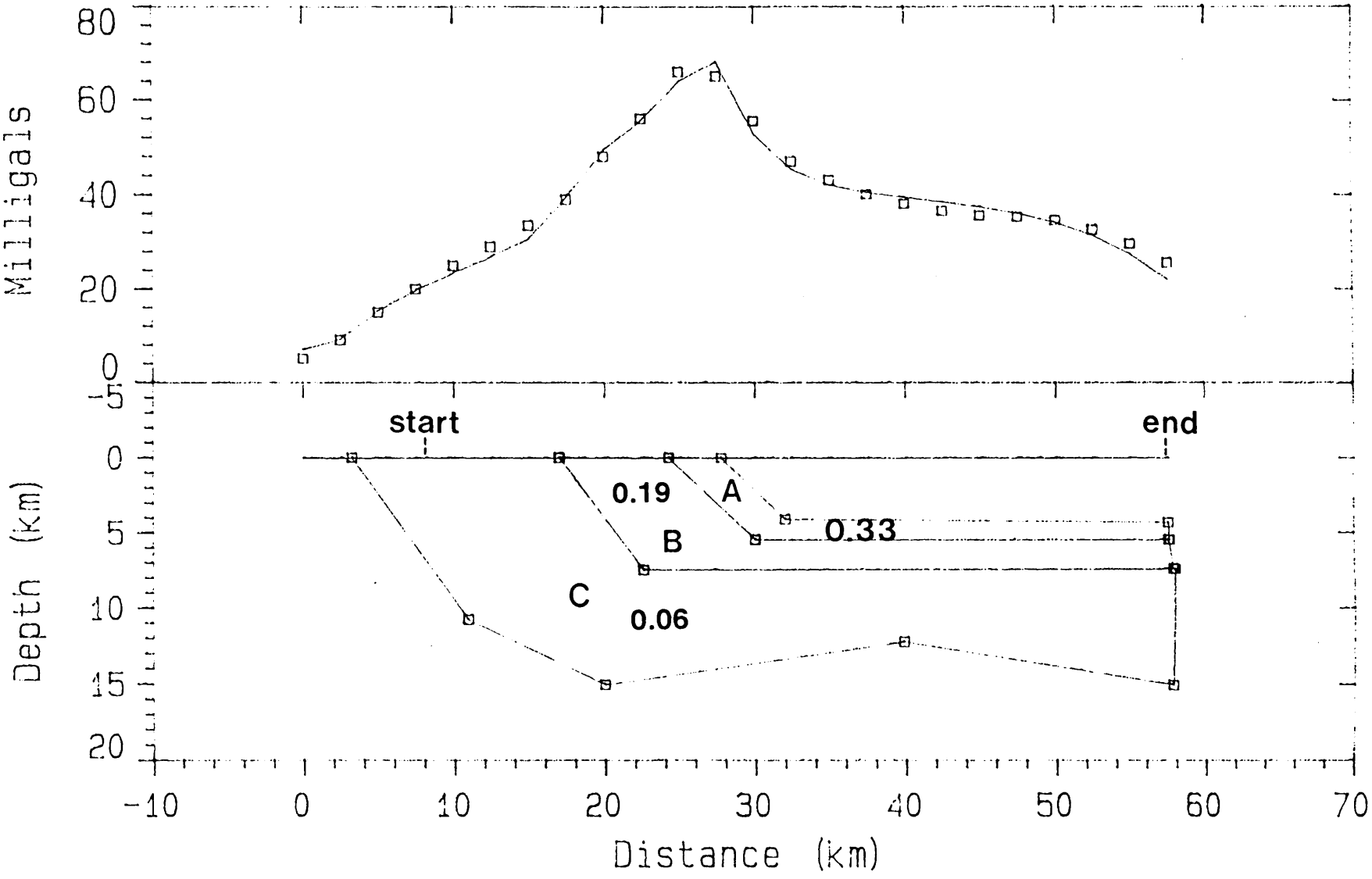

Fig 6.3 Gravity model of the region imaged by the seismic survey. A - upper zone of the RLS; B - combined Basal Norite Unit and main zone; C - Transvaal Sequence shales and quartzites (including the Hekpoort Andesite Formation). Data points are represented by the dotted line; the modeled response is represented by the solid line.

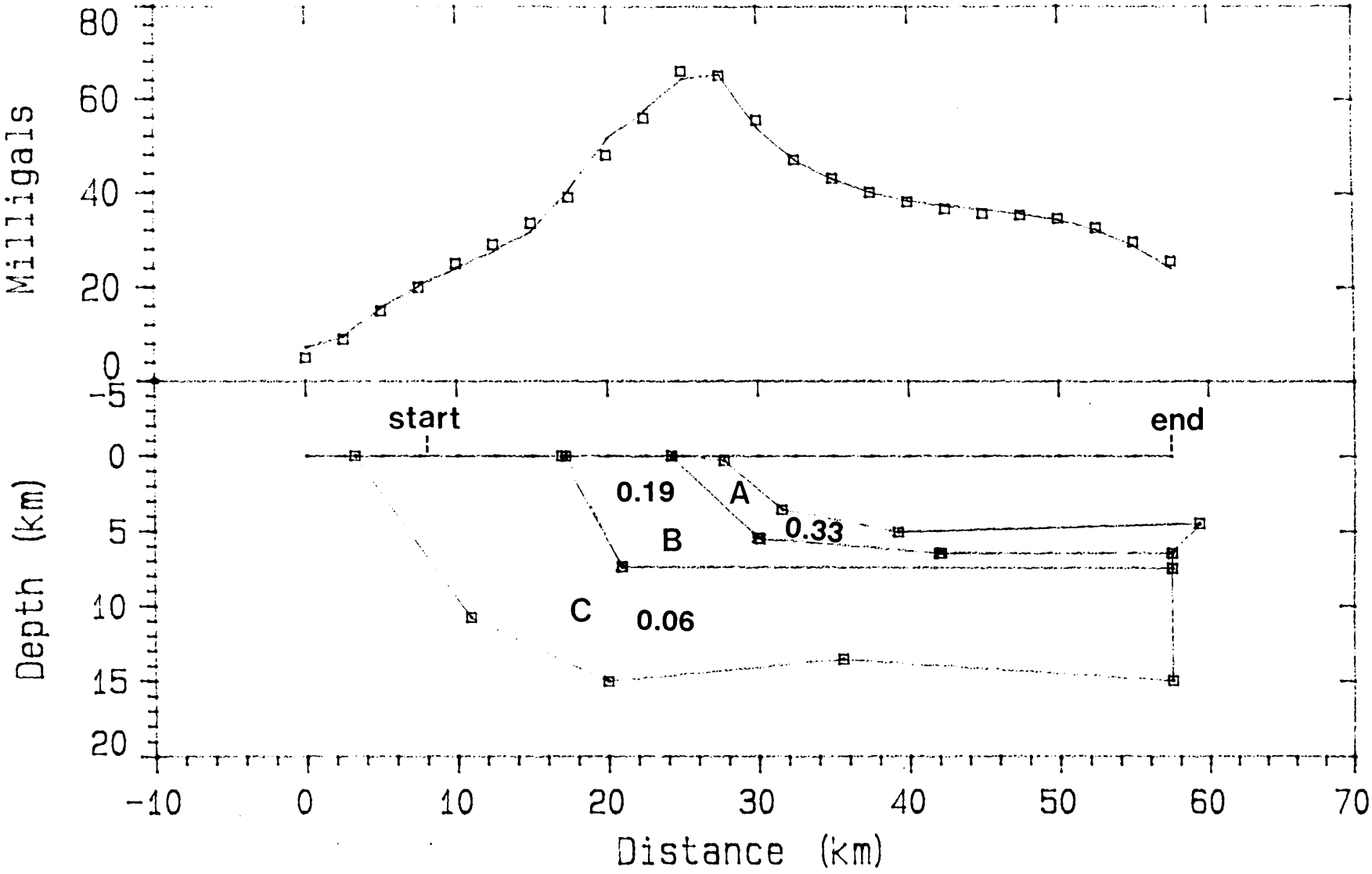

Fig 6.4 Gravity model of the region imaged by the seismic survey. A - upper zone of the RLS; B - combined Basal Norite Unit and main zone; C - Transvaal Sequence shales and quartzites (including the Hekpoort Andesite Formation). Data points are represented by the dotted line; the modeled response is represented by the solid line.

The ratio of interchangeability varies from 2,4:1 to approximately 3,1:1 (Personal communication; R. J. Kleywegt). For this reason they therefore only indicated a 'nominal' thin horizon of RLS rocks at the base of the Transvaal Sequence in their figures.

A more detailed gravity model (Fig. 6.5), proposing a tapering main zone, includes gravity data to the north of the study area. The results of the detailed gravity modeling confirm the proposal of Kleywegt and Du Plessis (1986) that the Rustenburg Layered Suite and the Transvaal Sequence are terminated at a major structural feature, north of the study area. The gravity model (Fig. 6.5) shows the proposed termination to occur approximately 2-8 km north of the end of the P1-86 seismic survey. However, by increasing the taper of the RLS and Transvaal Sequence to the north of the study area, it is possible to model the termination as occurring farther north. Although this ambiguity remains unresolved it is suggested, on the strength of the results of Kleywegt and Du Plessis (1986), that the position of the termination of the RLS and Transvaal Sequence is approximately as indicated in Figure 6.5.

The thickness of the Nebo Granite in the northern portion of the survey appears to be in excess of 3 km, attaining a maximum thickness of approximately 3,5-4,2 km (1,4 s TWT) at CMP 13255.

The region to the north of CMP 12055 is interpreted as one characterized by faulting, occurring in the tensional regime of an anticlinal structure. This anticlinal structure may be related to that described by Roberts (1981) as a "bulge" in the floor rocks. Roberts postulated that such a bulge may be responsible for the complex horst-graben faulting occurring in the RLS in the Brits area, west of Pretoria.

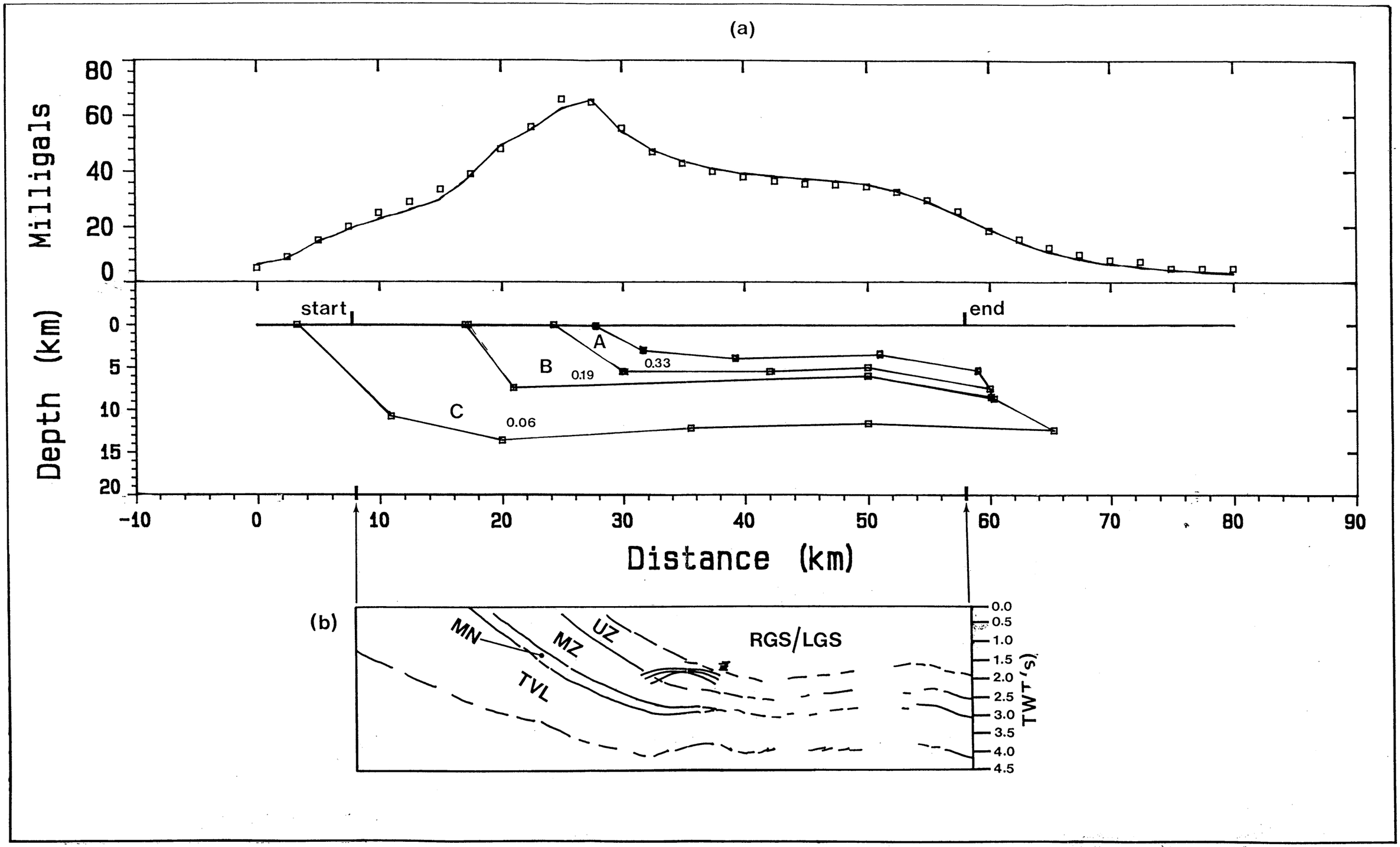

Fig 6.5 (a) - Gravity model of the region imaged by the seismic survey. A - upper zone of the RLS; B - combined Basal Norite Unit and main zone; C - Transvaal Sequence shales and quartzites (including the Hekpoort Andesite Formation). Data points are represented by the dotted line; the modeled response is represented by the solid line. (b) - Line drawing of the migrated seismic profile depicting interpreted boundaries. RGS/LGS - combined Rashoop Granophyre and Lebowa Granite suites; UZ - upper zone; MZ - main zone; MN - marginal norite; TVL - Transvaal Sequence shales and quartzites (including the Hekpoort Andesite Formation).

This bulge may have developed:

1. during isostatic readjustment related to the intrusion of the Bushveld Complex (Roberts, 1981);
2. in response to folding of the floor rocks along intersecting fold axes (Molyneux and Klinkert, 1978); or
3. as a result of diapirism of the floor rocks (Button, 1978).

Each of the above three models is associated with tensional-stress related faulting, similar to that which is interpreted in the northern part of the seismic section.

Further evidence of the influence of anticlinal features on the structure of the RLS is observed in the Crocodile River Fragment region, northwest of the survey area. The Bushveld Complex in the region of the Crocodile River Fragment is considered to be characterized by complex folding (Ferguson, 1973; Walraven and Darracott, 1976; Hartzer, 1986; Hartzer, 1989). Hartzer (1989) proposed that updoming of the Transvaal Sequence rocks in the Crocodile River Fragment area may have formed a barrier which prevented the intrusion of the RLS, from a proposed feeder site on the northwest margin of the Crocodile River Fragment, into the area beneath and to the east of the Crocodile River Fragment. Postulates that no mafic rocks of significant thickness occur beneath or to the east of the Crocodile River Fragment are supported by extensive geophysical evidence (Smit, 1961; Walraven and Darracott, 1976; Meyer and De Beer, 1987).

Folding of the floor rocks of the Bushveld Complex, observed extensively throughout the Bushveld Complex and shown in the current interpretation of the P1-86 seismic profile, has thus been shown to be a major factor controlling the extent and nature of the RLS. Interpretation of the P1-86 seismic profile in this thesis indicates that floor folds are responsible for pinching out of the marginal norite and considerable thinning of the main zone of the RLS in the survey area. Structural constraints to the north of the survey area,

identified by forward modeling of the regional gravity data, appear to cause complete pinching out of the main and upper zones of the RLS, and termination of the Transvaal Sequence.

CHAPTER 7

DISCUSSION OF RESULTS

7.1 OBSERVATIONS DURING PROCESSING

The following observations were made concerning the suitability of various processing methods to the P1-86 seismic data:

1. the data appear to be reasonably insensitive to the parameters utilized during refraction static calculation and application. There does, however, appear to be an improvement in the quality of the static corrected section when a single refracting layer is specified;

2. the data appear to be relatively insensitive to variations in the stacking velocity function. This is due to the high seismic velocities and low velocity gradient in this region. Optimum results for velocity analysis were obtained by performing constant velocity stacks over the entire section. Interpretation of these stacked sections resulted in the construction of the optimum stacking velocity function;

3. trace oriented deconvolution provided a more interpretable stacked section in comparison to gather oriented deconvolution;

4. the quality of the migrated section was found to be sensitive to variations in migration velocities. Migration velocities were tested using constant velocity F-K migration and the optimum velocity function was determined from the collection of F-K migrated sections. This velocity function was utilized during the phase-shift migration;

5. phase-shift migration with a migration aperture of 90° was used to produce the best result. The difference between the output migrated sections, however, became more subtle as the migration aperture increased above 30°; and

6. to avoid Rieber mixing (Hardage, 1983; Sheriff, 1984) care should be exercised when filtering the data in the Fourier domain. The best result for the P1-86 survey was obtained by applying a 3500 m/s tapered-fan FK filter to the poststack data.

7.2 COMPARISON OF PROCESSING RUNSTREAMS USED ON THE SEISMIC DATA

The processing runstreams applied to the P1-86 seismic data, both in this thesis and in Du Plessis and Levitt (1987), are listed in Table 7.1. A number of significant differences are apparent:

1. In Du Plessis and Levitt (1987) a tapered fan F-K filter is applied in the shot domain. Application of an F-K filter in the shot domain may remove a significant portion of diffraction energy located in the flanks of the diffraction hyperbolae. The resulting loss of diffraction energy may have deleterious effects on the migration process. Since the seismic data in this thesis were to be migrated, no such filter was applied to the prestack data.

2. Poststack predictive deconvolution was applied to the data in Du Plessis and Levitt (1987). No poststack deconvolution was applied to the P1-86 data in this research, as preliminary testing indicated that there was no significant difference between the deconvolved and non-deconvolved stacked sections.

3. The seismic data in this thesis were migrated using the phase-shift migration method. Migration of the data attempted to restore dipping

TABLE 7.1 Processing runstreams used in this research and in Du Plessis and Levitt (1987)

RUNSTREAM USED IN THIS RESEARCH	RUNSTREAM USED IN DU PLESSIS AND LEVITT (1987)
1. Demultiplexing of the SEGD field correlated vibroseis data	1. Demultiplexing of the SEGD field correlated vibroseis data
2. Trace editing and first break picking	2. Spherical divergence correction
3. Refraction statics calculation	3. Trace editing
4. Application of refraction statics	4. Refraction statics calculation
5. Spherical divergence correction	5. Application of refraction statics to a floating datum
6. Envelope-function programmed gain control	6. Velocity filtering of common shot gather using tapered-fan F-K filter
7. Trace oriented minimum phase deconvolution in the shot domain	7. Minimum phase predictive deconvolution application in the shot domain
8. Envelope-function programmed gain control	8. Scaling using whole trace equalization
9. Shot domain to CMP domain sorting	9. Shot domain to CMP domain sorting
10. Constant velocity NMO correction	10. NMO correction
11. CMP stack	11. Data corrected from floating to regional datum
12. Application of 15-20-75-90 Hz trapezoidal bandpass filter	12. Generation of a stacked section
13. Envelope-function programmed gain control	13. Surface consistent residual statics calculation and application

14. Correction of data to regional datum (1040 m)	14. Refining of stacking velocities
15 Velocity analysis using CVS	15. t-x muting application
16. Top-end mute of CMP gathers	16. Data corrected from floating to regional datum
17. Application of NMO correction	17. CMP consistent residual statics application
18. CMP stack	18. CMP stacking
19. Surface consistent residual statics calculation and application	19. Poststack minimum phase predictive deconvolution application
20. Application of NMO correction	20. Time and spatially variant bandpass filtering
21. CMP stack	21. Coherency enhancement
22. Application of 15-20-75-90 Hz trapezoidal bandpass filter	22. AGC scaling
23. Envelope-function programmed gain control	23. Generation of a stacked section
24. Correction of data to regional datum (1040 m)	
25. Migration velocity analysis using constant velocity FK migration	
26. Phase-shift migration of CMP stacked section	
27. Application of 20-75 Hz, 3500 m/s tapered-fan FK-filter	

events to their true spatial positions and collapse diffractions to the diffraction point (Berkhout, 1981; Sheriff, 1984; Claerbout, 1985; Yilmaz, 1987). Despite the inability of two-dimensional migration to provide ideal results in the presence of complex three-dimensional structure (Yilmaz, 1987), the improvement in spatial and lateral resolution enhanced interpretation of the seismic data.

7.3 DISCUSSION OF GEOLOGICAL MODELS DERIVED FROM THE SEISMIC DATA

The interpreted geological model, proposed in this thesis, suggests that the Transvaal Sequence rocks and units of the RLS are regionally continuous across the seismic section. Two variations of the model, with respect to the RLS in the northern region of the survey, are proposed:

1. The first variation interprets the upper zone of the RLS as thinning towards the northern end of the study area. Two-dimensional forward modeling of gravity data confirmed that the Transvaal Sequence and RLS may be modeled as a regionally continuous dipping structure, with the high density upper zone ferrogabbros tapering towards the northern limit of the survey (Fig. 6.3).

2. The second variation suggests that the marginal norite package may pinch out over a proposed anticlinal structure in the floor rocks, and that the main zone is laterally continuous within the study area, but considerably reduced in thickness north of the anticlinal structure. In this variation the upper zone is laterally continuous within the study area, and has approximately constant thickness (Fig. 6.4 and Fig. 6.5). Such pinching out of units has been observed in the Bushveld Complex (Schwellnus *et al.*, 1962), and lateral discontinuity of the marginal norites is illustrated in Roberts (1981).

A wider lateral distribution of the upper zone than the marginal and main zones in many regions of the Bushveld Complex is supportive of this model (Von Gruenewaldt, 1979; Kleywegt, 1988).

Interpretation of the seismic data showed that the prominent seismic events correlated well with the surface geology. Du Plessis and Levitt (1987) interpreted the prominent dipping seismic event, originating at approximately 0,1 s at the southern end of the survey (event 1; Fig. 6.1a), to be the seismic expression of the Hekpoort Andesite Formation. They were, however, unable to correlate this event with the surface expression of the Hekpoort Andesite Formation (Du Plessis, *pers comm.*). In this thesis this event is interpreted to represent a prominent diabase sill, approximately 85 m thick, which outcrops approximately 1 000 m south of the starting point of the survey. The seismic event correlates well with the surface expression of the diabase sill.

Noise observed in the central and northern portions of the seismic section was attributed, in this thesis, to the imaging of out-of-the-plane events and bends in the survey line. Additional deterioration of the signal-to-noise ratio is proposed to be a result of signal interference (Ohlovich, 1964), related to the imaging of a region of complex faulting associated with the postulated anticlinal structure. Du Plessis and Levitt (1987) propose that this noise is a result of traversing the proposed Mabopane Fault at an acute angle.

Du Plessis and Levitt (1987) imply a northerly dipping fault (Du Plessis, *pers comm.*), the northern side of which has an upthrow of approximately 8 500 m. Such a thrust fault implies that the crust was in compression during the formation of the fault. Since the Magaliesberg members of the Transvaal Sequence are present to the south of the fault, the implication is that the fault post-dates the Magaliesberg Quartzite Formation. The Pretoria Group rocks have been dated at 2 224 m.y. ± 21 (Burger and Coertze, 1975), while the RLS has been dated at 2 050 m.y. (Kruger *et al.*, 1986; Sharpe *et al.*, 1986) to 2 100 m.y. (Hamilton, 1977). This implies that a relatively short

period was available for the crustal environment to change from one of compression (favouring the formation of a thrust fault), to the extensional environment necessary for the intrusion of such a large volume of igneous material. For the model of Du Plessis and Levitt (1987) to be valid, 8 500 m of material would also need to be eroded from the upthrown (northern) side of the fault during this time period. These factors place constraints on the feasibility of the model proposed by Du Plessis and Levitt (1987).

The model suggested in this thesis describes an anticlinal structure which is proposed to influence the structure and occurrence of the RLS within the study area. This model is supported by extensive documentation of large-scale folding in the floor rocks of the Bushveld Complex, and the effect such folding has upon the structure and distribution of the RLS (Ferguson, 1973; Walraven, 1974; Hunter, 1975; Walraven and Darracott, 1976; Button, 1978; Molyneux and Klinkert, 1978; Roberts, 1981; Hartzer, 1986; Engelbrecht, 1987; Hartzer, 1989; Schürmann, 1991). The structure which appears to terminate the Transvaal Sequence north of the study area (Fig. 6.5) is proposed to be either related to the Crocodile River Fragment, or alternately to be of diapiric origin.

While forward modeling of the regional gravity data was used in Du Plessis and Levitt (1987) to support an abrupt termination of the RLS within the study area, such gravity modeling does not imply that geological models proposed as a result of gravity modeling are unique (Al-Chalabi, 1971; Zidarov, 1990). Du Plessis and Kleywegt (1987) illustrated the ambiguity inherent in modeling gravity data (Fig. 2.1).

Vertical dimensions specified in geological models based on the forward modeling of gravity data should, in the absence of accurate knowledge of the subsurface geology, be regarded as order of magnitude dimensions (Kleywegt and Du Plessis, 1986). Such dimensions are dependant upon the correct selection of density contrast (Kleywegt and Du Plessis, 1986) and the choice

of the regional gravity field. Within the above constraints, it has been shown that the gravity data may also be used to support the geological model favoured in this thesis (Fig. 6.5).

7.4 IMPLICATIONS OF THE PROPOSED GEOLOGICAL MODEL

Albeit there is no evidence for the termination of the RLS within the study area, cognizance must be taken of the effect which the anticlinal floor structure has on the marginal norite and the main zone. Should similar structures occur north of the survey area, as suggested by the results of gravity modeling in this thesis (Fig. 6.5) and by Kleywegt and Du Plessis (1986), the RLS may be expected to pinch out. This hypothesis supports models in which the RLS is nonexistent in the central Bushveld Complex. Thus, while models proposing a sill-like structure for the RLS (Molyneux and Klinkert, 1978; Kleywegt and Du Plessis, 1986; Du Plessis and Kleywegt, 1987) are supported by the geological model proposed in this thesis, those based on the RLS tapering or pinching out (Molyneux and Klinkert, 1978; Kleywegt and Du Plessis, 1986) are favoured.

The postulated termination of the Transvaal Sequence, approximately 8 km north of the study area, may correspond to the zone identified by Walraven and Darracott (1976), along which the RLS pinches out. This tentative correlation is in approximate agreement with that made by Kleywegt and Du Plessis (1986). If the above correlation is valid, the implication is that the Crocodile River Fragment, at some time, extended eastwards beneath the area now covered by the Irrigasie Formation.

The evidence of anticlinal structures in the study area, provided by the interpretation of the P1-86 seismic profile in this thesis, lends support to hypotheses relating the development of the Transvaal basin and the structure of the Bushveld Complex to pre- and syn-Bushveld folding.

7.5 CONCLUSIONS AND RECOMMENDATIONS

Conventional prestack velocity analysis methods did not appear to provide the optimum stacking velocity function. Interpretive processing has enabled the effect of velocity variations to be evaluated over entire seismic events on the CMP stacked section.

Trace oriented deconvolution provided better results than gather oriented deconvolution. Despite the computational expense of trace oriented deconvolution, the use of such a method of deconvolution is merited for the P1-86 data.

In regions of complex geological structure it was concluded that a large amount of noise observed on the stacked section may be due to out-of-the-plane events. In such cases a single seismic survey line, in the absence of suitable controls such as borehole data, may be insufficient to image the subsurface in a manner allowing a unique interpretation of the data. In terms of improving the reliability of the final interpreted section, it may be desirable to implement a 3-D survey, or to implement a survey of intersecting lines, each intersecting at the point of interest and having different azimuths.

In structurally complex areas it is observed that, while improving the resolution of the data, 2-D poststack migration algorithms are not entirely suitable. As the evaluation of the effect of application of prestack migration to land seismic data is an extensive topic warranting separate research, the effect of prestack migration on the P1-86 data has not been evaluated. Such evaluation is recommended for future research.

ACKNOWLEDGEMENTS

The author wishes to thank the following:

1. Ron Hinds for his guidence throughout the project;

2. Prof. von Gruenewaldt for his advice on the geology of the Bushveld Complex and help with the interpretation;

3. the Geological Survey of South Africa and, in particular, Edgar Stettler and Andre du Plessis, for the opportunity to be involved in this project;

4. the Geological Survey of South Africa for permission to publish the data;

5. the National Geophysics Program for funding the research project;

6. Anglo American Prospecting Services, Klerksdorp, for hardcopy plotting of some of the early results;

7. Jeanette, my mother, and friends and colleagues for their interest and support; and

8. The American Dream, good red wine, and Mexican Taxi Drivers for their motivation, inspiration and solace, respectively.

The processing of the seismic data was performed using ITA INSIGHT/1 processing software.

REFERENCES

Al-Chalabi, M., 1971, Some studies relating to non-uniqueness in gravity and magnetic inverse problems: Geophysics, **36**, 835-855.

_____ , 1973, Series approximations in velocity and traveltime computations: Geophys. Prosp., **21**, 783-795.

Berkhout, A. J., 1981, Wave field extrapolation techniques in seismic migration, *in* Migration of seismic data: G. H. F. Gardner, Ed., Soc. Explor. Geophys., 414-432.

Brown, G. L. and Moxley, S. D., 1964, Hydraulic servomechanisms as seismic energy sources, *in* Geyer, R. L., Ed., Vibroseis: Soc. Explor. Geophys., 84-92.

Burger, A. J. and Coertze, F. J., 1975, Summary of age determinations carried out during the period April 1972 to March 1974: Ann. Geol. Surv. S. Afr, **10**, 135-141.

Button, A., 1978, Major diapiric structures in the Bushveld floor, north-eastern Transvaal: Trans. geol. Soc. S. Afr.

Camina, A. R. and Janacek, G. J., 1984, Mathematics for seismic data processing and interpretation: Graham and Trotman.

Chapman, W. L., Brown, G. L. and Fair, D. W., 1981, The Vibroseis system: a high frequency tool: Geophysics, **46**, 1657-1666.

Chun, J. H. and Jacewitz, C., 1981, Fundamentals of frequency-domain migration: Geophysics, **46**, 717-732.

Claerbout, J. F., 1970, Coarse grid calculations of waves in inhomogeneous media with application to delineation of complicated seismic structure: Geophysics, **35**, 407-418.

_____ , 1976, Fundamentals of geophysical data processing: McGraw-Hill.

_____ , 1985, Imaging the earth's interior: Blackwell Scientific Publications.

_____ and Doherty, S. M., 1972, Downward continuation of moveout-corrected seismograms: Geophysics, **37**, 741-768.

Cousins, C. A., 1959, The structure of the mafic portion of the Bushveld Igneous Complex: Trans. Geol. Soc. S. Afr., **62**, 179-189.

Crawford, J. M., Doty, W. E. N. and Lee, M. R., 1960, Continuous signal seismograph, *in* Geyer, R. L., Ed., Vibroseis: Soc. Explor. Geophys., 73-83.

Dahl-Jensen, T., 1989, Static corrections on crystalline rock: Geop. Prosp. **37**, 467-478.

Daly, R. A. and Molengraaff, G. A. F., 1924, Structural relations of the Bushveld Igneous Complex, Transvaal: Jour. Geol., **32**, No. 1, 1-35.

Du Plessis, A. and Kleywegt, R. J., 1987, A dipping sheet model for the mafic lobes of the Bushveld Complex: S. Afr. J. Geol., **90(1)**, 1-6.

_____ and Levitt, J. G., 1987, On the structure of the Rustenberg Layered Suite - insight from seismic reflection data: Presented at the Indaba on the tectonic setting of layered intrusives, Geol. Soc. of S. Afr., Geol. Sur. of S. Afr., Univ. of Pretoria, Inst. for Geol. Res. on the Bushveld Complex.

Engelbrecht, J. P., 1987, The tectonic setting of the Bushveld Complex in the Marico district, South Africa: Presented at the Indaba on the tectonic setting of layered intrusives, Geol. Soc. of S. Afr., Geol. Sur. of S. Afr., Univ. of Pretoria, Inst. for Geol. Res. on the Bushveld Complex.

Eriksson, P. G. and Twist, D., 1986, A note on a lahar deposit in the Hekpoort Formation, Transvaal Sequence near Pretoria: Trans. geol. Soc. S. Afr., **89**, 415-418.

Farrell, R. C. and Euwema, R. N., 1984, Refraction statics: Proc. Inst. Electr. Electron. Eng., **72**, 1316-1329.

Ferguson, J., 1973, The Pilansberg alkaline province, southern Africa: Trans. geol. Soc. S. Afr., **76**, 249-270.

Foster, M. R. and Guinzy, N. J., The coefficient of coherence; its estimation and use in geophysical data processing: Geophysics, **32**, 602-616.

Gazdag, J., 1978, Wave equation migration with the phase-shift method: Geophysics, **43**, 1342-1351.

Geyer, R. L., 1969, The Vibroseis system of seismic mapping: Jour. Canadian Soc. Explor. Geop., **6**, 7-23.

Goupillaud, P. L., 1976, Signal design in the Vibroseis technique: Geophysics, **41**, 1291-1304.

Hall, A. L., 1932, The Bushveld Igneous Complex of the central Transvaal: Mem. Geol. Surv. S. Afr., **28**, 540pp.

Hamilton, J., 1977, Sr isotope and trace element studies of the Great Dyke and Bushveld mafic phase and their relation to early Proterozoic magma genesis in southern Africa: J. Petrol., **18**, 24-52.

Hartzer, F. J., 1989, Stratigraphy, structure, and tectonic evolution of the Crocodile River Fragment: S. Afr. J. Geol, **92(2)**,110-124.

_____ , 1986, Stratigraphy and structure of the Crocodile River Fragment: Extd. Abst. Geocongress '86, Univ. of the Witwatersrand, Jhb., S. Afr.

Harvey, P. L., 1981, 'n Regionale gravitasie opname van die 1:250 000 vel 2528 (Pretoria): Unpubl. Rep. geol. Surv. S. Afr., **1981-0026**.

Hattingh, P. J., 1991, The magnetic susceptibility of the mafic rocks of the Bushveld Complex: S. Afr. J. Geol., **94**, 132-136.

_____ , 1983, A palaeomagnetic investigation of the layered mafic sequence of the Bushveld Complex: Ph.D. thesis, Univ. of Pretoria.

Hardage, B. A., 1983, Vertical seismic profiling: Handbook of Geophysical Exploration, **14A**, Helbig, K. and Treitel, S., Eds., 450pp.

Hatton, L., Worthington, M. H. and Makin, J., 1986, Seismic data processing: theory and practice: Blackwell Scientific Publications Inc.

Hinds, R. C., Kuzmiski, R. D., Botha, W. J. and Anderson, N. L., 1989, Vertical and lateral seismic profiles, *in* Geophysical atlas of western Canadian hydrocarbon pools: Anderson, N. L., Hills, L. V. and Cederwall, D. A., Eds., CSEG/CSPG, 319-344.

Hosken, J. W. J. and Deregowski, S. M., 1985, Tutorial migration strategy: Geophys. Prosp., **33**, 1-33.

Hunter, D. R., 1975, The regional geological setting of the Bushveld Complex (An adjunct to the provisional tectonic map of the Bushveld Complex): Econ. Geol. Res. Unit, Univ. of the Witwatersrand, 18pp.

Jorissen, E., 1904, On the occurrence of the Dolomite and Chert Series in the northeast part of the Rustenburg district: Trans. Geol. Soc. S. Afr., **7**, 30-38.

Kleywegt, R. J., 1988, The Moloto structure and the possible occurrence of the Rustenburg Layered Suite northeast of the Roodeplaat Complex: Extd. Abst. Geocongress '88, Univ. Natal, S. Afr., 333-336.

_____ and Du Plessis, A., 1986, On the structure of the Bushveld Complex and the central Transvaal basin: Extd. Abst. Geocongress '86, Univ. of the Witwatersrand, Jhb., S. Afr.

Kruger, F. J., Cawthorn, R. G., Meyer, P. S. and Walsh, K. L., 1986, Sr-isotopic chemical and mineralogical variations across the pyroxenite marker and in the upper zone of the western Bushveld Complex: Extend. Abstr. Geocongress 1986, Johannesburg, Geol. Soc. S. Afr., 609-612.

Lerwill, W.E., 1981, The amplitude and phase response of a seismic vibrator: Geop. Prosp. **29**, 503-528.

Levinson, N., 1947, The Wiener RMS (Root Mean Square) error criterion in filter design and prediction: J. Math. Phys., **25**, 261-278.

Lines, L. R. and Clayton, R. W., 1977, A new approach to vibroseis deconvolution: Geop. Prosp., **25**, 417-433.

Loewenthal, D., Lu, L., Roberson, R. and Sherwood, J., 1976, The wave equation applied to migration: Geop. Prosp., **24**, 380-399.

McQuillin, R., Bacon, M. and Barclay, W., 1984, An introduction to seismic interpretation: Graham and Trotman Ltd.

Mellor, E. T., 1906, The geology of the central portion of the Middelburg district: Ann. Rept. Geol. Surv. Transvaal, 55-71.

Meyer, R., 1987, The structure of the Bushveld Complex: An evaluation of geophysical evidence: Presented at the Indaba on the tectonic setting of layered intrusives, Geol. Soc. of S. Afr., Geol. Sur of S. Afr., Univ. of Pretoria, Inst. for Geol. Res. on the Bushveld Complex.

_____ and De Beer, J., 1987, Structure of the Bushveld Complex from resistivity measurements: Nature, **325**, 610-612.

Molengraaff, G. A. F., 1902, Vice President's address: Trans. Geol. Soc. S. Afr., **5**, 69-75.

_____ , 1901, Geologie de la Republique S. Africaine: Bull. Soc. Geol. France, **4**, vol 1, 13-92.

Molyneux, T. G. and Klinkert, P. S., 1978, A structural interpretation of part of the eastern mafic lobe of the Bushveld Complex and it's surrounds: Trans. geol. Soc. S. Afr., **81**, 359-368.

Ohlovich, V. A., 1964, The causes of noise in seismic reflection and refraction work: Geophysics, **29**, 1015-1030.

Reichhardt, F. J., 1989, A petrological investigation of the transition from the lower to the upper critical zone in the central sector of the eastern Bushveld Complex: PhD. thesis, Univ. of Pretoria.

Roberts, K., 1981, The Pretoria - Brits project: Inst. geol. Res. Bushveld Complex Ann. Rep., Univ. of Pretoria, 10-15.

Robinson, E. A., 1983, Migration of geophysical data: IHRDC, Boston, 214pp.

_____ and Treitel, S.,1967, Principles of digital Wiener filtering: Geophys. Prosp., **15**, 311-333.

Rogers, A. W., 1985, Determination of static corrections: Developments in geophysical exploration methods, **6**, Fitch, A. A., Ed., Elsevier Applied Science Publishers Ltd.

Ronen, J. and Claerbout, J. F., 1985, Surface-consistent residual statics estimation by stack-power maximization: Geophysics, **50**, 2759-2767.

Rothman, D. H., 1986, Automatic estimation of large residual statics corrections: Geophysics, **51**, 332-346.

Russel, B. H., 1988, Introduction to seismic inversion methods: Domenico, S. N., Ed., Course Notes Series, **2**, Soc. Explor. Geop.

Schneider, W. A., 1978, Integral formulation for migration in two dimensions and three dimensions: Geophysics, **43**, 49-76.

Schürmann, L. W., 1991, The geochemistry and petrology of the upper critical zone in the Boshoek sector of the western Bushveld Complex: MSc. thesis, Univ. of Pretoria.

Schwellnus, J. S. I., Engelbrecht, L. N. J., Coertze, F. J., Russell, H. D., Malherbe, S. J., von Rooyen, D. P. and Cooke, R., 1962, The geology of the Olifants River area, Transvaal: Information sheet 2429B (Chuniespoort) and 2430A (Wolkberg), Geol. Sur. S. Afr., 87pp.

Sharpe, M. R., Evenson, N. M. and Naldrett, A. J., 1986, Sm/Nd and Rb/Sr isotopic evidence for liquid mixing, magma generation and contamination in the eastern Bushveld Complex: Extend. Abstr. Geocongress 1986, Johannesburg, Geol. Soc. S. Afr., 621-624.

Sheriff, R. E., 1984, Encyclopedic dictionary of exploration geophysics: Soc. Explor. Geophys.

_____ and Geldart, L. P., 1983, Exploration seismology: data-processing and interpretation: Cambridge Univ. Press.

_____ and Geldart, L. P., 1985, Exploration seismology: history, theory and data acquisition: Cambridge Univ. Press.

Smit, P. J., 1961, Gravity survey of the Republic of South Africa Part III-Interpretation of gravity anomalies: Geol. Surv. S. Afr. Open File Report 300, 234pp.

_____ , Hales. A. L. and Gough, D. I., 1962, The gravity survey of the Republic of South Africa, Handbook 3: Govt. Printer Pretoria, S. Afr., 484pp.

_____ and Maree, B. D., 1966, Densities of South African rocks for the interpretation of gravity anomalies, Bulletin 48: Govt. Printer Pretoria, S. Afr., 37pp.

South African Committee for Stratigraphy (SACS), 1980, Stratigraphy of South Africa. Part 1 (Comp. L. E. Kent). Lithostratigraphy of the Republic of South Africa, South West Africa/Namibia, and the Republics of Bophuthatswana, Transkei and Venda: Handb. geol. Surv. S. Afr., **8**.

Stolt, R. H., 1978, Migration by Fourier transform: Geophysics, **43**, 23-48.

Stone, D. G., 1977, Estimation of reflection coefficients from seismic data: Presented at the 47th annual meeting of the Soc. Explor. Geop., Calgary, Alberta, Canada.

Talwani, M., Worzel, J. L. and Landsman, M., 1959, Rapid gravity computations for two-dimensional bodies with application to the Mendocino submarine fracture: J. Geophys. Res., **64**, 49-59.

Taner, M. T. and Koehler, F., 1969, Velocity spectra - digital computer derivation and applications of velocity functions: Geophysics, **34**, 859-881.

_____ , Koehler, F. and Alhilali, K. A., 1974, Estimation and correction of near-surface time anomalies: Geophysics, **39**, 441-463.

Truter, F. C., 1955, Modern concepts of the Bushveld Igneous Complex: C.C.T.A. South. reg. comm. Geol., **1**, 77-87.

Viljoen, M. J. and Scoon, R. N., 1985, The distribution and main geologic features of discordant bodies of iron-rich ultramafic pegmatite in the Bushveld Complex: Econ. Geol., **80(4)**, 1109-1128.

Von Gruenewaldt, G., 1979, A review of some recent concepts of the Bushveld Complex with particular reference to sulfide mineralization: Canadian Mineralogist, **17**, 233-256.

Walraven, F., 1974, Tectonism during the emplacement of the Bushveld Complex and the resulting fold structures: Trans. Geol. Soc. S. Afr., **77**, 323-328.

_____ and Darracott, B. W., 1976, Quantitive interpretation of a gravity profile across the western Bushveld Complex: Trans. Geol. Soc. S. Afr., **79**, 22-26.

Waters, K. H., 1978, Reflection seismology: John Wiley and Sons.

Willemse, J., 1969, The geology of the Bushveld Igneous Complex, the largest repository of magmatic ore deposits in the world: Econ. Geol. Mono., **4**.

Wood, L. C., 1982, Imaging the subsurface, *in* Concepts and techniques in oil and gas exploration: K. C. Jain and R. J. P. deFigueiredo, Eds., Soc. Explor. Geophys., 45-90.

Yilmaz, O., 1987, Seismic data processing: Investigations in Geophysics, Volume 2, Society of Exploration Geophysicists.

Zidarov, D., 1990, Inverse gravimetric problem in geoprospecting and geodesy: Dev. in Solid Earth Geop., **19**, Elsevier Science Publishers.

APPENDIX A

THE TIME-TERM METHOD FOR THE CALCULATION OF REFRACTION STATIC CORRECTIONS

The fundamental equations of the time-term method of Farrell and Euwema (1984) are reviewed below.

Consider the raypath geometry of Figure 4.2:

The traveltime between source (A) and receiver (D) can be partitioned into 3 time-term components:

$$T_{AD} = T_{AB} + T_{BC} + T_{CD}$$

$$= \frac{\overline{AB}}{V_0} + \frac{\overline{BC}}{V_1} + \frac{\overline{CD}}{V_0} \qquad (A1)$$

But,

$$\overline{AB} = \frac{Z_1}{\cos i} \qquad (A2)$$

$$\overline{BC} = x\cos i - Z_1 \tan i - Z_2 \tan i \qquad (A3)$$

$$\overline{CD} = \frac{Z_2}{\cos i} \qquad (A4)$$

Substituting expressions (A2), (A3) and (A4) into equation (A1):

$$T_{AD} = \frac{Z_1}{V_0 \cos i} + \frac{x\cos\alpha}{V_1} - \frac{Z_1 \tan i}{V_1} - \frac{Z_2 \tan i}{V_1} + \frac{Z_2}{V_0 \cos i} \qquad (A5)$$

From the special case of Snell's Law,

$$\frac{\sin i}{1} = \frac{V_0}{V_1} \qquad (A6)$$

Thus,

$$\cos i = \sqrt{1 - \left(\frac{V_0}{V_1}\right)^2} \tag{A7}$$

$$\tan i = \frac{V_0}{V_1\sqrt{1 - \left(\frac{V_0}{V_1}\right)^2}} \tag{A8}$$

Substituting equations (A7) and (A8) into equation (A5):

$$T_{AD} = \frac{Z_1}{V_0\sqrt{1 - \left(\frac{V_0}{V_1}\right)^2}} + \frac{x\cos\alpha}{V_1} - \frac{Z_1 V_0}{V_1 V_1\sqrt{1 - \left(\frac{V_0}{V_1}\right)^2}} - \frac{Z_2 V_0}{V_1 V_1\sqrt{1 - \left(\frac{V_0}{V_1}\right)^2}} + \frac{Z_2}{V_0\sqrt{1 - \left(\frac{V_0}{V_1}\right)^2}} \tag{A9}$$

Simplifying equation (A9) results in:

$$T_{AD} = \frac{Z_1\sqrt{1 - \left(\frac{V_0}{V_1}\right)^2}}{V_0} + \frac{Z_2\sqrt{1 - \left(\frac{V_0}{V_1}\right)^2}}{V_0} + \frac{x\cos\alpha}{V_1}$$

$$= P_1 + P_2 + \frac{x\cos\alpha}{V_1} \tag{A10}$$

where

$$P_1 = \frac{Z_1\sqrt{1 - \left(\frac{V_0}{V_1}\right)^2}}{V_0} \tag{A11}$$

$$P_2 = \frac{Z_2\sqrt{1 - \left(\frac{V_0}{V_1}\right)^2}}{V_0} \tag{A12}$$

For shallow dip angles, $\cos\alpha \approx 1$, and equation (A10) may be simplified:

$$T_{AD} = P_1 + P_2 + \frac{x}{V_1} \tag{A13}$$

Let station x_1 be positioned at A and station x_2 be positioned at D; then equation (A13) becomes:

$$T_{AD} = P_1 + P_2 + \frac{x_2 - x_1}{V_1} \qquad (A14)$$

A laterally varying refractor velocity may be approximated using a least squares procedure. The reciprocal of the refractor velocity is expanded to a quadratic or cubic power of the station number along the line (Farrell and Euwema, 1984).

This may be described as:

$$\frac{1}{V_1} = a + bx + cx^2 + dx^3 \qquad (A15)$$

where x is the station number.

The traveltime using the laterally varying refractor velocity is given by:

$$\begin{aligned} T_{AD} &= P_1 + P_2 + \int_{x_1}^{x_2} \frac{dx}{V_1(x)} \\ &= P_1 + P_2 + |x_2 - x_1| \cdot \\ &\quad \{a + \frac{b}{2}(x_2 + x_1) \\ &\quad + \frac{c}{3}(x_2^2 + x_2 x_1 + x_1^2) \\ &\quad + \frac{d}{4}(x_2^3 + x_2^2 x_1 + x_2 x_1^2 + x_1^3)\} \end{aligned} \qquad (A16)$$

The limit evaluation results in:

$$\frac{1}{V_1} = \{a + \frac{b}{2}(x_2 + x_1) + \frac{c}{3}(x_2^2 + x_2 x_1 + x_1^2) + \frac{d}{4}(x_2^3 + x_2^2 x_1 + x_2 x_1^2 + x_1^3)\} \qquad (A17)$$

Thus:

$$T_{AD} = P_1 + P_2 + (x_2 - x_1) \cdot \{a + \frac{b}{2}(x_2 + x_1) + \frac{c}{3}(x_2^2 + x_2 x_1 + x_1^2) + \frac{d}{4}(x_2^3 + x_2^2 x_1 + x_2 x_1^2 + x_1^3)\} \qquad (A18)$$

APPENDIX B

THE NMO EQUATION FOR A SYSTEM OF HORIZONTAL LAYERS

To generalize the NMO equation for a system of horizontal layers it is necessary to define two parameters; the average velocity and the root mean squared (rms) velocity.

Consider a system of n horizontal homogeneous layers as shown in Figure B1. Let t_j be the two-way vertical traveltime in layer j and t be the total two-way traveltime of a primary ray reflecting off base n.

Thus

$$t = \sum_{n} t_j \tag{B1}$$

The average velocity V_{ave} is given by:

$$V_{ave} = \frac{\text{total vertical distance}}{\text{total 1-way vertical traveltime}}$$

$$= \frac{h_1 + h_2 + \ldots + h_n}{1/2(t_1 + t_2 + \ldots + t_n)} \tag{B2}$$

But

$$h_j = \frac{1}{2} v_j t_j \tag{B3}$$

Thus the average velocity is given by:

$$V_{ave} = \frac{v_1 t_1 + v_2 t_2 + \ldots + v_n t_n}{t_1 + t_2 + \ldots + t_n}$$

$$= \frac{\sum_{i=1}^{n} v_i t_i}{\sum_{i=1}^{n} t_i} \tag{B4}$$

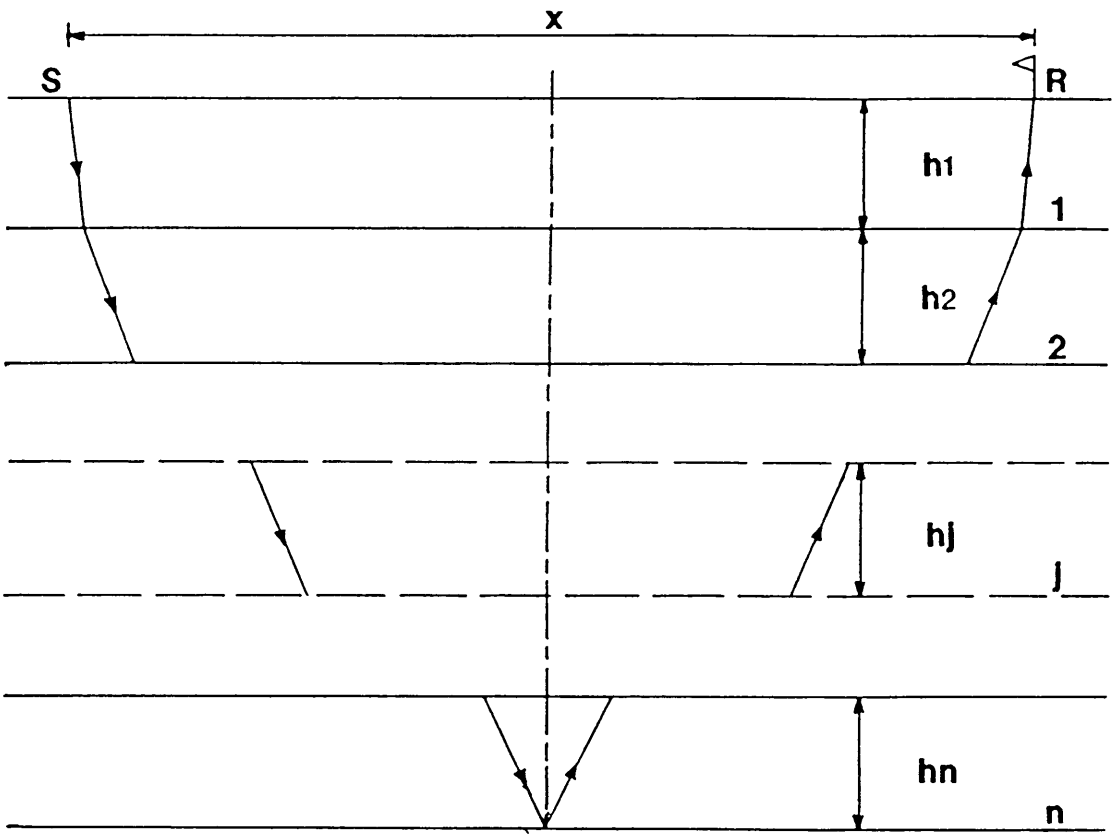

Fig. B-1 Diagrammatical representation of the geometry associated with multiple layer NMO. x is the shot-receiver offset.

The RMS velocity to the base of layer n is:

$$\overline{v}_n = \left(\sum_{i=1}^{n} v_i^2 t_i / \sum_{i=1}^{n} t_i \right)^{\frac{1}{2}} \qquad (B5)$$

For a number of flat horizontal reflectors the travel time curves are no longer hyperbolic, but take the form:

$$t^2 = t_0^2 + b_2 x^2 + b_4 x^4 + \ldots \qquad (B6)$$

where t_0 is the two-way traveltime of the normal reflected ray, and b is a function of the seismic velocity.

Inspection of a typical seismic record shows that, with the exception of very long offsets, the shapes of the traveltime curves can be closely approximated by hyperbolae. The approximation works well, even in areas of reasonably complex geologic structure (Taner *et al.*, 1970).

For a given reflection event we can write:

$$t^2 \approx t_0^2 + b_2 x^2 \qquad (B7)$$

For a single layer:

$$b_2 = \frac{1}{v^2} \qquad (B8)$$

For n layers:

$$b_2 = \frac{1}{\overline{v}_n^2} \qquad (B9)$$

(Dobrin, 1976; Yilmaz, 1987)

Subject to the small-spread (Fig. 4.7) and small dip approximations (Yilmaz, 1987), we can write:

$$t^2 \approx t_0^2 + \frac{x^2}{\overline{v}_n^2} \qquad (B10)$$

Thus, for a system of n horizontal layers, the NMO equation (equation 4.22) becomes:

$$\Delta t_{NMO} = \sqrt{t_0^2 + \left(\frac{x}{\overline{v}_n}\right)^2} - t_0 \qquad \text{(B11)}$$

APPENDIX C

THE CONVOLUTIONAL MODEL FOR THE SEISMIC TRACE

The earth's reflectivity series may be represented as the sum of n time-shifted delta functions, $\delta(t - nT)$, having amplitudes corresponding to the reflectivity coefficient time series.

Thus

$$rc_t = \sum_n rc_n \delta(t - nT) \qquad (C1)$$

where rc_t is the earth's reflectivity function and rc_n is the amplitude of the delta function at time $t = n$.

Similarly, a seismic trace, x_t, may be represented as the sum of n time-shifted seismic wavelets, each having an amplitude proportional to the earth's reflectivity coefficient at time $t = n$:

$$x_t = \sum_n rc_n w(t - nT) \qquad (C2)$$

where rc_n is the amplitude of the wavelet at time $t = n$ and $w(t-nT)$ is the time-shifted seismic wavelet.

The discrete time-shifted wavelets, $w(t-nT)$, may be treated as a continuous signal by convolution with the time-shifted delta function, $\delta(\tau - nT)$:

$$w(t-nT) = \int_{-\infty}^{\infty} \delta(\tau - nT) w(t-\tau) d\tau \qquad (C3)$$

Equation (C2) then becomes:

$$x_t = \sum_n rc_n \int_{-\infty}^{\infty} \delta(\tau - nT) w(t-\tau) d\tau$$

$$= \int_{-\infty}^{\infty} \sum_n rc_n \delta(\tau - nT) w(t-\tau) d\tau$$

$$= \int_{-\infty}^{\infty} rc_\tau w(t-\tau) d\tau \qquad \text{from (C1)}$$

$$= rc_t * w_t \qquad (C4)$$

by definition of continuous signal convolution.

Thus the ideal seismic trace can be represented by the convolution of the earth's reflectivity function with the seismic wavelet.

APPENDIX D

THE NORMAL EQUATIONS FOR THE LEAST-SQUARES FILTER

The following review of the normal equations for least squares filtering is given after Sheriff and Geldart (1983).

If the input seismic trace is given by x_v and the desired output given by y_v then the least-squares filter, r_v will be that which minimizes the expression

$$\sum_t (y_t - r_t * x_t)^2 \tag{D1}$$

The least squares method attempts to minimize the square of the error by setting the partial derivatives of the sum of the squares of the error, with respect to the variables r_i, equal to zero.

Thus

$$\frac{\partial}{\partial r_i} \sum_t (y_t - x_t * r_t)^2 = 0 \qquad i = 0, 1, \ldots, n \tag{D2}$$

Application of the chain rule for differentiation and simplifying results in the expression

$$\sum_t (y_t - x_t * r_t) \frac{\partial}{\partial r_i} (x_t * r_t) = 0 \quad i = 0, 1, \ldots, n \tag{D3}$$

For each of the n+1 elements of r_i we obtain one equation. Expressing the convolution operators in terms of a sum using the identity

$$\begin{aligned} h_t &= f_t * g_t = g_t * f_t \\ &= \sum_k f_k g_{t-k} = \sum_k g_k f_{t-k} \end{aligned} \tag{D4}$$

we have

$$\sum_t (y_t - \sum_k x_k r_{t-k}) \frac{\partial}{\partial r_i} \left(\sum_k x_k r_{t-k} \right) = 0 \tag{D5}$$

Consider the expression

$$\frac{\partial}{\partial r_i}\left(\sum_k x_k r_{t-k}\right) \tag{D6}$$

The only non-zero terms in the differential will be those involving r_i. This occurs when $k = t - i$.

Thus

$$\frac{\partial}{\partial r_i}\left(\sum_k x_k r_{t-k}\right) \equiv \frac{\partial}{\partial r_i}(x_{t-i} r_i) = x_{t-i} \tag{D7}$$

Hence, equation (D5) becomes:

$$\sum_t (y_t - \sum_k x_k r_{t-k}) x_{t-i} = 0 \tag{D8}$$

Rearranging equation (D8):

$$\sum_t y_t x_{t-i} = \sum_t \sum_k x_k x_{t-i} r_{t-k} \tag{D9}$$

Note that

$$\sum_t y_t x_{t-i} = \phi_{yx}(-i) \tag{D10}$$

where ϕ_{yx} represents the crosscorrelation of the two data sets y and x.

Using the identity

$$\phi_{yx}(-i) = \phi_{xy}(i) \tag{D11}$$

equation (D9) is rewritten:

$$\phi_{xy}(i) = \sum_t \sum_k x_k x_{t-i} r_{t-k} \tag{D12}$$

Let $j = t - k$ and sum over j:

$$\phi_{xy}(i) = \sum_t \sum_j x_{t-j} x_{t-i} r_j$$

$$= \sum_j r_j \sum_t x_{t-j} x_{t-i} \qquad \text{(D13)}$$

Consider now the expression for the autocorrelation

$$\phi_{xx}(\tau) = \sum_k x_k x_{k+\tau} \qquad \text{(D14)}$$

Changing the summation over k to a summation over j, where $j = t - k$, the expression for the autocorrelation becomes

$$\phi_{xx}(\tau) = \sum_j x_{t-j} x_{t-j+\tau}$$

$$= \sum_j x_{t-j} x_{t-i} \qquad \text{where} \quad i = \tau + j$$

$$= \phi_{xx}(i - j) \qquad \text{(D15)}$$

Thus equation (D13) becomes:

$$\phi_{xy}(i) = \sum_j r_j \phi_{xx}(i - j)$$

$$= \sum_{j=0}^{n} \phi_{xx}(i - j) r_j \qquad i = 0, 1, \ldots, n \qquad \text{(D16)}$$

This constitutes the *normal equations* for least squares filtering.

APPENDIX E

THE 2-D FOURIER TRANSFORM

Consider the 2-D scalar wave equation describing the propagation of compressional wave fields $P(x,z,t)$ in a medium of constant density and compressional wave velocity:

$$\frac{\partial^2 P}{\partial x^2} + \frac{\partial^2 P}{\partial z^2} = \frac{1}{v^2}\frac{\partial^2 P}{\partial t^2} \tag{E1}$$

or

$$\left(\frac{\partial^2}{\partial x^2} + \frac{\partial^2}{\partial z^2} - \frac{1}{v^2}\frac{\partial^2}{\partial t^2}\right)P(x,z,t) = 0 \tag{E2}$$

For constant lateral velocity it is possible to perform a double Fourier transform over x and t:

$$P(x,z,t) \Rightarrow P(k_x, z, \omega) \tag{E3}$$

Thus, by definition of the Fourier transform;

$$P(x,z,t) = \int\int P(k_x, z, \omega) e^{i(\omega t - k_x x)} \, dk_x d\omega \tag{E4}$$

Applying equation (E2) to equation (E4) gives

$$\frac{\partial^2}{\partial z^2}P(k_x, z, \omega) + (-ik_x)^2 P(k_x, z, \omega) - \frac{(i\omega)^2}{v^2}P(k_x, z, \omega) = 0 \tag{E5}$$

Simplification results in the expression

$$\frac{\partial^2}{\partial z^2}P(k_x, z, \omega) + \left(\frac{\omega^2}{v^2} - k_x^2\right)P(k_x, z, \omega) = 0 \tag{E6}$$

APPENDIX F

F-K (STOLT) MIGRATION

Equation (E6) may be rewritten:

$$\frac{\partial^2}{\partial z^2}P(k_x, z, \omega) = -\left(\frac{\omega^2}{v^2} - k_x^2\right)P(k_x, z, \omega) \tag{F1}$$

Claerbout (1985) shows the dispersion relation of the 2-D scalar wave equation to be:

$$k_x^2 + k_z^2 = \frac{\omega^2}{v^2} \tag{F2}$$

Substitute (F2) into equation (F1):

$$\frac{\partial^2}{\partial z^2}P(k_x, z, \omega) = -k_z^2 P(k_x, z, \omega) \tag{F3}$$

Equation (F1) has two sets of solutions; one for downgoing waves and the other for upgoing waves. We are interested in the upgoing (reflected) wave solution.

The solution to the Helmholz equation is

$$P(k_x, z, \omega) = P(k_x, 0, \omega)e^{i\gamma z} \tag{F4}$$

where

$$\gamma^2 = \left(\frac{\omega^2}{v^2} - k_x^2\right) = k_z^2 \tag{F5}$$

For the upgoing wave the negative root must be chosen. Thus

$$k_z = -\sqrt{\frac{\omega^2}{v^2} - k_x^2} \tag{F6}$$

Hence, the solution to the upgoing wave equation is given as

$$P(k_x, z, \omega) = P(k_x, 0, \omega)e^{-ik_z z} \tag{F7}$$

We now perform the inverse transformation

$$P(k_x, z, \omega) \Rightarrow P(x, z, t) \tag{F8}$$

Substituting the result of equation (F7) into the definition of the inverse double Fourier transform

$$P(x,z,t) = \int\int P(k_x, z, \omega) e^{i(\omega t - k_x x)} \, dk_x d\omega \tag{F9}$$

results in

$$P(x,z,t) = \int\int P(k_x, 0, \omega) e^{i(\omega t - k_x x - k_z z)} \, dk_x d\omega \tag{F10}$$

Since k_x remains constant under migration, k_z can be mapped to the frequency ω by equation (F6). Thus

$$P(x,z,t) = \int\int P(k_x, 0, \omega) e^{i\left(\omega t - k_x x + \sqrt{\frac{\omega^2}{v^2} - k_x^2}\, z\right)} \, dk_x d\omega \tag{F11}$$

Substituting t = 0 into equation (F11) results in the equation for the migrated depth section:

$$P(x,z,0) = \int\int P(k_x, 0, \omega) e^{i\left(\sqrt{\frac{\omega^2}{v^2} - k_x^2}\, z - k_x x\right)} \, dk_x d\omega \tag{F12}$$

From equation (F2):

$$\frac{d\omega}{dk_z} = \frac{v k_z}{\sqrt{k_x^2 + k_z^2}} \tag{F13}$$

Substitution of equation (F13) into equation (F12) results in the constant velocity F-K migration equation

$$P(x,z,0) = \int\int P(k_x, 0, \omega[k_x, k_z]) e^{i(k_z z - k_x x)} \frac{v k_z}{\sqrt{k_x^2 + k_z^2}} \, dk_x dk_z \tag{F14}$$

APPENDIX G

STOLT STRETCH

Consider the compressional wave field P(x,z,t); this is transformed into the "stretched" wave field P(x,d,T), where T is the stretched time axis and d is the migration coordinate corresponding to z in the stretched section. The relation between T and t is given by

$$T(t) = \frac{1}{c}\left[2 \int_0^t dt \quad v_{rms}^2(t)t \right]^{\frac{1}{2}} \tag{G1}$$

where

$$v_{rms}^2(t) = \frac{1}{t} \int_0^t v^2(t)dt \tag{G2}$$

and c is an arbitrary reference velocity used to maintain the vertical axis as time after the coordinate transformation.

This modifies the input wave field to make it appear to be the response to a constant velocity earth. Stolt (1978) shows that the "stretched" scalar wave equation takes the form

$$\left(\frac{\partial^2}{\partial x^2} + W \frac{\partial^2}{\partial d^2} + \frac{2}{c} \frac{\partial^2}{\partial d \partial T} \right) P(x,d,T) = 0 \tag{G3}$$

where W is the stretch factor, a function of velocity and coordinate variables (Yilmaz, 1987).

The dispersion relation (equation F6) is modified for use with Stolt stretch:

$$k_d = \left(1 - \frac{1}{W} \right) \frac{\omega_T}{c} - \frac{1}{W} \sqrt{\frac{\omega_T^2}{c^2} - W k_x^2} \tag{G4}$$